THE UNIVERSITY
of ADELAIDE

Nanodiamond in Optical Fibre

by

Matthew Ryan Henderson

Supervisors:
Prof. Tanya Monro
Dr. Shahraam Afshar V.
A/Prof. Heike Ebendorff-Heidepriem
A/Prof. Andrew Greentree

A thesis submitted in fulfillment of the
degree of Doctor of Philosophy

in the
Faculty of Sciences
School of Chemistry & Physics

May 2013

Declaration of Authorship

I certify that this work contains no material which has been accepted for the award of any other degree or diploma in any university or other tertiary institution and, to the best of my knowledge and belief, contains no material previously published or written by another person, except where due reference has been made in the text. In addition, I certify that no part of this work will, in the future, be used in a submission for any other degree or diploma in any university or other tertiary institution without the prior approval of the University of Adelaide and where applicable, any partner institution responsible for the joint-award of this degree.

I give consent to this copy of my thesis when deposited in the University Library, being made available for loan and photocopying, subject to the provisions of the Copyright Act 1968.

I also give permission for the digital version of my thesis to be made available on the web, via the Universitys digital research repository, the Library catalogue and also through web search engines, unless permission has been granted by the University to restrict access for a period of time.

Signed: _____

Date: _____

"Don't panic."

Douglas Adams, The Hitchhiker's Guide to the Galaxy

UNIVERSITY OF ADELAIDE

Abstract

Faculty of Sciences
School of Chemistry & Physics

Doctor of Philosophy

by Matthew Ryan Henderson

Diamond, prized as both a gemstone and a cutting and polishing material, has recently been recognised for another remarkable property, a host of optically active colour centre defects. With the rise of interest in these colour centres, due to the unique optical properties, comes a need for interfacing with other optical platforms. Recent advances have attempted to fabricate optical structures from the diamond itself, or to combine these colour centres with the well-known fabrication techniques of other materials by placing nanodiamond crystals on the surface of other structures, such as microdisks, microspheres, and optical fibres.

This thesis presents a new approach to this integration by demonstrating the fabrication of a hybrid nanodiamond-glass material. This technique embeds the nanodiamond within the optical structure, offering interaction with the bound optical fields, protection, and ease of fabrication. A range of optical structures has previously been fabricated from the chosen glass, tellurite, and fabrication of an optical fibre is demonstrated here.

Also presented is the derivation of a model describing coupling of an emitter to an optical fibre. While used here to investigate coupling of diamond colour centres to the optical fibre modes, it is more generally applicable to any emitter.

These results show the first steps of a new approach to diamond integrated photonics.

Acknowledgements

Firstly, a special thank you to my supervisors, Shahraam Afshar, Heike Ebendorff-Heidepriem, Andrew Greentree and Tanya Monro. This thesis would not have been possible without their discussions, assistance and support — and their efforts above and beyond the call of duty in the face of a looming deadline for submission.

Thank you to Brant Gibson for your guidance during my time at the University of Melbourne — from discussions of measurements, to discussions of football and the best Teriyaki beef lunch I've ever had. Also from the University of Melbourne; David Simpson, Snjezana Tomljenovic-Hanic, Igor Aharonovich, Julius Orwa, and Stephen Prawer. Without the sharing of their expertise in diamond there would only be tellurite in the diamond-tellurite fibre.

I appreciate the help of Alastair Dowler, Roger Moore, Kevin Kuan, Kenton Knight and Rachel Moore. Without their vast technical knowledge this project would not have proceeded.

Thank you to my office buddies, Erik Schartner, Stephen Warren-Smith, Michael Oermann, Sean Manning and Sebastian Ng, for the chats (both work-related and, more commonly, not so work-related), lunches, and occasional after-hours gaming sessions.

To Kris Rowland, thank you for the unannounced drop-ins whenever I had a question and for the chats that usually followed.

I enjoyed working with everyone at IPAS, thank you all for the discussions and corridor meetings.

Finally, another special thanks — this time to my family for their support over the years. To my new family, my wife Katie for always being there for me, and my daughter Ruby for being so cute and making me happy every time I look at her.

Contributions

All aspects of the project were discussed at regular meetings with my supervisors — Shahraam Afshar, Heike Ebendorff-Heidepriem, Andrew Greentree and Tanya Monro — and, later in the project, Brant Gibson (University of Melbourne).

Chapter 2

I derived the equations for the coupling coefficients, using Snyder and Love's *Optical Waveguide Theory*. I researched the appropriate power function needed to normalise the guided power capture, beginning with a dipole radiating in a bulk material. When we realised that this did not include the effects of the fibre structure (and specifically the core-cladding interface), I deduced that the correct expression was to use the radiation modes, in addition to the guided mode power, to calculate total power.

I wrote the Matlab code to calculate these coupling coefficients and the radiation modes and power, and the Meep control files of the finite-difference time domain method calculations. Step-index mode solving code was written in collaboration with Kris Rowland.

The whispering gallery mode calculations were performed in collaboration with Shahraam Afshar. The planning of the investigation into this effect, and obtaining and discussion of the results, was a joint exercise, and included some discussions with Kris Rowland and Alexandre Francois. I wrote the Matlab code to calculate the guided and radiated power, the corresponding electric and magnetic fields, and the code to find contributions from different β ranges. Shahraam Afshar derived the expression for, and wrote the code to calculate, the positions of the pure whispering gallery mode modal solutions.

Chapter 3 and 4

Glass fabrication was performed by Kevin Kuan and Kenton Knight, with some assistance from me. Planning of the glass melts was a joint discussion between me, Heike Ebendorff-Heidepriem, and either Kevin Kuan or Kenton Knight. I performed the preform extrusions. The fibre drawing was performed by Roger Moore and Alastair Dowler, with some assistance and guidance from me. Lidded wagon-wheel fabrication included discussions with Heike Ebendorff-Heidepriem and Roger Moore.

I performed the scanning electron microscope imaging, with assistance from Heike Ebendorff-Heidepriem and Rachel Moore. Raman spectroscopy of glass sample G1 was performed by Elizabeth Carter (Vibrational/Electronic Spectroscopy, School of Chemistry, The University of Sydney). Raman and photoluminescence spectroscopy, and NV^0/NV^- ratio measurements on preform sample P2 were performed by Igor

Aharonovich and Julius Orwa (University of Melbourne). I performed the optical microscope imaging.

I performed the confocal imaging and anti-bunching measurements, with training and assistance from Brant Gibson. Confocal measurements were planned in collaboration with Brant Gibson. The confocal system used was previously set up at the University of Melbourne.

Contents

List of Figures

List of Tables

List of Abbreviations

AFM atomic force microscope

APD avalanche photodiode

CVD chemical-vapour deposition

FDTD finite-difference time domain

HBT Hanbury Brown-Twiss

IPAS Institute for Photonics & Advanced Sensing

MOF microstructured optical fibre

NA numerical aperture

ND nanodiamond

NV nitrogen-vacancy

NV^0 neutral nitrogen-vacancy

NV^- negative nitrogen-vacancy

ODMR optically detected magnetic resonance

PL photoluminescence

PML perfectly-matched layer

RAM random access memory

RF radio frequency

RT room temperature

SEM scanning electron microscopy

SNOM scanning near-field optical microscope

UV-Vis ultraviolet-visible spectroscopy

WGM whispering gallery mode

ZPL zero phonon line

Physical Constants

Speed of Light	c	=	$2.997\,924\,58 \times 10^{8}\,\mathrm{m\,s^{-1}}$ (defined)
Permittivity of free space	ϵ_0	=	$8.854 \times 10^{-12}\,\mathrm{F\,m^{-1}}$
Permeability of free space	μ_0	=	$4\,\pi \times 10^{-7}\ \mathrm{V\,s\,A^{-1}\,m^{-1}}$

Symbols

a	coupling coefficient
k_0	free space wavenumber
n	refractive index
N_j	$= \frac{1}{2} \int\limits_{A_\infty} \mathbf{e}_j \times \mathbf{h}_j^* \cdot \hat{z} \ \mathrm{d}A$
P	power
r_{core}	fibre core radius
β	propagation constant
λ	wavelength
ω	angular frequency
ρ	normalised dipole radial position (r/r_{core})

To my lovely wife Katie,

and our daughter Ruby (the cutest baby in the world),
this is for you kiddo.

1

Introduction

Diamond has become an important material in our present day technology, used in a wide variety of fields including industry, jewellery, and scientific research. Many properties of diamond are exceptional — high hardness and thermal conductivity, a good electrical insulator, and a large transmission window. There is also a strong interest in another property of diamond: colour centres, which are defects in the crystal lattice. Diamond hosts a variety of lattice defects that have recently garnered interest. One such colour centre, the nitrogen-vacancy (NV) centre, has applications in a wide range of fields, including single photon generation, magnetometry, and quantum computing. An introduction to the NV colour centre follows in Section 1.1.

The research presented in this thesis aims to integrate these diamond centres with other photonic systems, to take advantage of the unique colour centre properties, by combining them with optical fibre. This would lead to a device that is easily introduced into existing photonics and could take advantage of the large field of optical fibre research knowledge. Integration of diamond colour centres with optical structures is discussed in Section 1.3. In the work presented here, diamond was added to the initial stages of fibre creation, at the glass fabrication stage. This is the first demonstration of a hybrid diamond-glass material designed to leverage the advantages of diamond colour centre emission.

The application was for efficient collection of single photon emission, for the realisation of a single photon source with a fibre-coupled output. A low melting point glass, tellurite [1], was chosen as the host glass because of possible damage to the diamond at high temperatures. Tellurite has previously been used to fabricate microstructured optical fibres (MOFs) [1], a fibre design that can achieve a high core-cladding index contrast and thus a high emission capture, which would be an advantage for the proposed single photon source. An overview of MOFs is presented below in Section 1.4. Although the initial application was for single photon collection, optical fibre coupling to the diamond

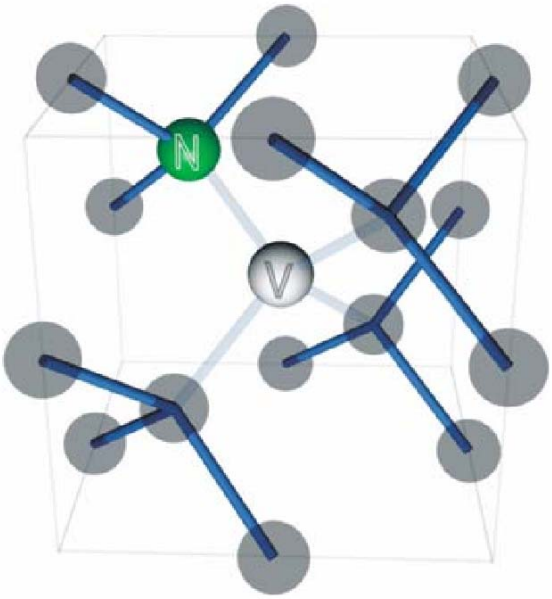

FIGURE 1.1: Diagram of an NV colour centre, consisting of a substitutional nitrogen atom adjacent to a lattice vacancy, in the diamond carbon lattice. From Ref. [2].

NV centre could also be used for magnetometry, for example allowing remote read-out and probing.

1.1 Nitrogen-vacancy colour centres

Colour centres are defects in a crystal that are optically active. This defect can be a vacancy in the lattice, a substituted atom or an interstitial atom (an atom between lattice positions). One such centre in diamond is the NV centre [2], consisting of a substitutional nitrogen atom adjacent to a vacancy in the lattice (as shown in Figure 1.1). There are over 500 identified colour centres in diamond [3], however many of these do not have proven single photon properties. In addition to NV [4, 5], proven single photon emitters include emitters based on nickel-nitrogen [2, 6, 7], silicon [8], and chromium [9], and a recent review of single photon emitters in diamond can be found in Ref. [10]. NV centres can occur naturally at low concentrations in diamond, but are more commonly produced artificially. In nitrogen-rich diamond samples, they can be formed by creating lattice vacancies by radiation damage and annealing to mobilise these vacancies next to the nitrogen impurities [11]. For specifically low-nitrogen diamond, the centres can be accurately located by implanting nitrogen in the desired region [12, 13].

The NV defect can be used to create a triggered single photon source [4, 14], a photon source that emits only a single photon on demand. Although this property is common to all single emitters (fluorophores [15], quantum dots [16, 17], etc.), the NV centre is

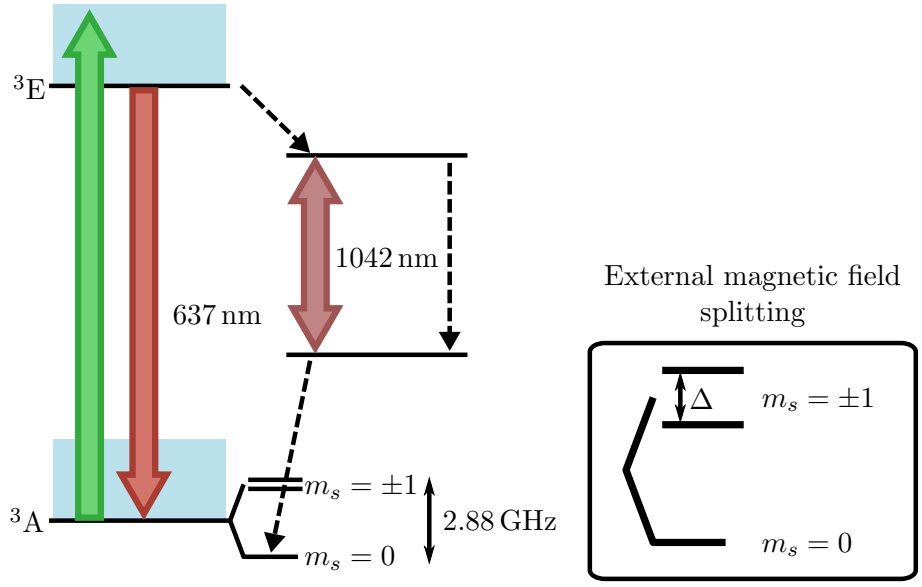

FIGURE 1.2: Energy levels of the NV^- colour centre showing pumping and photoluminescence. The 637 nm emission corresponds to the ZPL in the emission spectrum.

photostable at room temperature and does not exhibit photobleaching [18, 19]. These properties are advantageous when compared to other single dipole sources that operate at cryogenic temperatures [15, 17] or that are unstable and photobleach during use.

The NV centre has been found in either of two charge states; the neutral nitrogen-vacancy (NV^0) state, and the negative nitrogen-vacancy (NV^-) state [20]. The centres are photochromic [21], where intense irradiation can switch the state of a centre between NV^0 and NV^-. The NV^- energy levels are shown in Figure 1.2 [22], and the transition from $^3E \rightarrow {}^3A$ emits a photon at 637 nm wavelength, although this zero phonon line (ZPL) at 637 nm is broadened significantly by phonon sidebands. The neutral state has a ZPL at 575 nm [21], and also shows broad phonon sidebands. Either is suitable for use in single photon applications, as both states have large dipole moments (and hence emit photons at a high count rate) and also have negligible non-radiative decay rates (hence every cycle emits a photon).

Due to the particular energy level structure (see Fig. 1.2), NV^- shows quantum properties, such as spin polarisation and room temperature coherence [20], which is not seen in the NV^0 state and have, so far, not been seen in other colour centres. The ^3E ground state of NV^- is split into a spin zero and spin ± 1 states, with an energy gap of 2.88 GHz (see Fig. 1.2). Excitation and emission from $^3E \rightarrow {}^3A$ is generally spin-conserving (an excitation-emission cycle returns to the same spin state), although continuous illumination spin polarises the NV^- by optically pumping into the spin zero state via the

singlet transition [20, 23]. Emission is ∼30% brighter for the spin zero state, so that the intensity of the fluorescence signal can be used to distinguish the ground state spin [24].

The energy splitting between the NV^- spin zero and spin ±1 state can be measured optically, known as optically detected magnetic resonance (ODMR), by using the difference in photoluminescence (PL) intensity [25]. An applied radio frequency (RF) signal can, if at the same frequency as the ground state splitting energy, populate the spin ±1 states from the spin zero ground state. This spin ±1 population will decrease the PL and so, by scanning the applied RF frequency and monitoring the PL intensity, the splitting energy can be measured.

NV^- defects are sensitive to perturbation by external magnetic fields, allowing these centres to be used for magnetometry [22, 23, 24]. An applied external magnetic field splits the degenerate spin ±1 states, and the ground state Hamiltonian becomes [23]

$$\mathcal{H}_0 = \hbar D S_z^2 + g\mu_B B_z S_z, \tag{1.1}$$

where $\hbar D S_z^2$ is the crystal field splitting term (where $D = 2\pi \times 2.88\,\text{GHz}$), B_z is the component of the external magnetic field along the NV^- centre axis, $g \approx 2$ for NV, μ_B is the Bohr magneton, and S_z takes the values $m_s = 0, \pm 1$. The spin ±1 state is now split by an amount $\Delta = 2g\mu_B B_z$ (see Fig. 1.2), and measuring the ground state splitting using ODMR will now show two dips in PL as a function of RF frequency. The frequency difference between the two PL dips can be used to calculate this splitting and so the external magnetic field.

1.2 Other candidate single photon sources

As mentioned above (see Section 1.1), any single emitter can potentially act as a single photon source. For instance, both fluorescent molecules [15] and quantum dots [16, 17] have been used as sources of single photons.

Fluorescent molecules are unsuitable for direct inclusion within the optical glass, due to destruction by the high (∼700 °C) glass melting temperatures, and so would have to be included after fibre fabrication. Post-processing methods such as coating of the fibre core could be used to couple the fluorophore to the fibre, although only by the evanescent field. Fluorescent molecules are also affected by photobleaching, whereby the molecule is eventually destroyed (i.e. becomes non-fluorescent) by exposure to the pumping light.

The high glass melting temperatures would be of less concern for semiconductor quantum dots (such as InAs, CdS, or CdSe). Most quantum dots are, like diamond colour centres, not affected by photobleaching, although they can suffer from photoblinking (where the quantum dot will intermittently stop emitting).

Both fluorophores and quantum dot emitters also generally operate under cryogenic temperatures [15, 16, 17], compared to the room-temperature operation of diamond colour centres.

1.3 Combining diamond and photonic structures

To take advantage of the diamond colour centre properties, the centres must be integrated with other photonic structures. Methods of integration can be split into two main categories; using diamond as the photonic material, or combining diamond nanocrystals with other optical materials. See also Ref. [26] for a review of diamond photonic structures.

Optical device fabrication techniques for diamond are immature compared to other, more studied, materials such as silicon, but there has been some successes in fabricating optical structures from diamond crystals. Nanopillars have been fabricated in NV-containing diamond crystal by masking and etching [27, 28]. Focused ion-beam milling has been used to fabricate solid immersion lenses in diamond [29, 30]. Diamond waveguides [31, 32] and microrings [33] have also been milled in a two-step process, in which a layer of diamond was first converted to graphite (sp^3 carbon to sp^2) by irradiation in the desired pattern, and then selective etching of the graphite revealed the final diamond structure.

In general, though, diamond fabrication is difficult and so combining nano-scale diamond crystals, containing colour centres, with existing optical structures is an attractive solution. Use of these nanodiamonds (NDs) can also be split into two main approaches; either locating the ND outside the photonic structure and coupling using evanescent fields, or embedding the ND inside the structure.

External coupling of NV centres in ND has been achieved using a variety of photonic structures. Diamond nanocrystals have been nanopositioned, using scanning near-field optical microscope (SNOM)/atomic force microscope (AFM) equipment, onto optical fibre endfaces [34, 35], microspheres [36], microdisk resonators [37], and photonic crystals [38]. Solution coating has also been used to attach ND onto microspheres [39]. Nanopositioning of a gallium phosphide photonic crystal cavity on the surface of a

poly(methyl methacrylate) film showed coupling to embedded nanodiamond NV centres [40].They have been grown, using chemical-vapour deposition (CVD), onto the endfaces of optical fibre [41], and coated onto optical fibre tapers [42].

Creating a hybrid diamond-glass material leads to new possibilities for fabrication. The diamond is embedded within the optical material and this removes the restriction of coupling only to the evanescent fields. The colour centre and photonic structure may also be protected from the environment, as access from outside is not required for ND placement. It combines the fabrication properties of a soft glass with the optical properties of diamond, and more specifically the diamond colour centre.

A limitation common to the previously mentioned techniques of colour centre integration is the low device yield obtained in fabrication. Either labour-intensive nano-positioning is required, decreasing output due to time constraints, or (such as in the case of CVD deposited diamond) the useable device yield is low due to random placement of the colour centres. The hybrid diamond-tellurite material shown here would allow the use of macroscopic fabrication techniques to produce the diamond-fibre hybrid device for large quantity production, without the need for high precision placement equipment such as nanometre-resolution SNOMs, AFMs or confocal microscopes. This strategy would also improve overall device yield by allowing a large number of devices to be fabricated at the same time from a fibre pull of up to a few hundred metres. Well-known glass processing techniques, for example extrusion [43] (see Section 3.2.4), are available for fabrication of a wide variety of fibre designs that will then incorporate the attractive colour centre properties of room temperature single photon emission and spin coherence, and photostability.

1.4 Microstructured optical fibres

Optical fibres can be thought of as guiding light by internal reflections, where the light is constrained to the core area by reflecting from the cladding. The reflection mechanism is typically total internal reflection, relying on a core refractive index that is higher than the cladding index so that light is reflected at low angles of incidence. However, other reflection methods are also effective — for example, photonic crystal bandgap fibres use a bandgap effect, where the light is not able to propagate in the cladding material due to a periodic interference condition. These guidance mechanisms rely on a refractive index pattern across the fibre cross-section, and there are a range of methods to achieve this patterning. For instance, standard telecommunications fibre uses doping to raise the refractive index of the core region. A class of fibres, known as microstructured optical fibres (MOFs), use micron-scale refractive index patterning for guidance [44, 45, 46].

The patterning can either lower the average cladding refractive index, for guidance by total internal reflection, or create a periodic array for a bandgap effect.

A refractive index variation can be achieved in several different ways, however; such as index-changing doping of specific components (e.g. combining doped silica rods in undoped silica capillary stacking) or using different materials. For many MOF designs, the refractive index changes are introduced by incorporating air holes in the structure. By using a combination of the fibre material and air, complex fibre structures can be fabricated using well-controlled techniques. There are a range of techniques available for fabrication of MOFs, with a common workflow of creating a macroscopic shaped glass piece which is then drawn down to microscopic dimensions using a fibre draw tower. Methods such as capillary stacking, where air holes are introduced by the capillary holes, and extrusion [43], creating patterns by forcing the material through a die, can be used to create complex cross-sectional structure that, when drawn down, can result in the micron-scale features needed for light guidance. Other methods such as casting or drilling are also available, although any process that allows a pattern or structure to be formed in the glass can be used.

MOFs allow great flexibility in the design of the structure. Generally, as air is used for the refractive index variation, a large core-cladding refractive index contrast is available, which leads to a high numerical aperture (NA). Also, the air holes can be filled with liquids or gasses for sensing applications [47], giving a long interaction length and a close proximity to the guided core light.

In this project, the optical fibre development was focused on a suspended core fibre design. A suspended core fibre would allow a maximal core-cladding index contrast by using air as the cladding material, which is advantageous for emission collection. The tellurite glass used for ND inclusion had also been successfully used to fabricate this type of fibre structure previously [1]. In this design, the glass core is suspended in an air cladding with a supporting structure used to locate the core within an external glass jacket (required for structural strength and to isolate the air cladding). The particular variation used here, called a 'wagon-wheel' fibre, supports the micron-scale core with three equally-spaced radial struts connected to a large ($\sim$200 µm) glass jacket (see Fig. 1.3). Between these struts are air holes used to form a cladding. As the strut thickness decreases, the fibre approaches a pure air-clad suspended core design. This is an established MOF design and has been previously fabricated in a variety of materials [1, 48, 49, 50, 51].

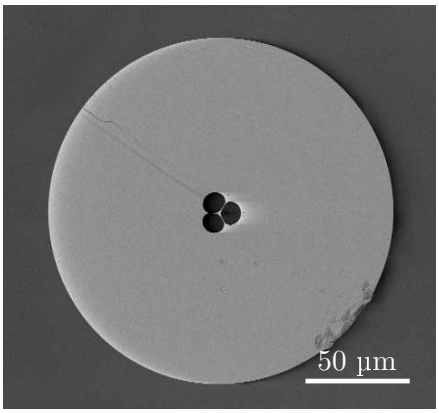

FIGURE 1.3: SEM image of a wagon-wheel suspended core fibre.

1.5 Outline

This thesis will present the first demonstration of a hybrid diamond-glass, experimental characterisation of this glass and the resulting optical fibres, and theoretical modelling of the expected emission characteristics of a fibre-embedded colour centre.

Chapter 2 shows the development of a general analytical model for emission coupling to an optical fibre, based on a dipole emitter in a step-index fibre geometry. The analytical model was used to explore the effect of fibre design on the expected NV emission capture into the optical fibre modes, and to study the change in the radiation pattern and emitted power of a dipole in the vicinity of the optical fibre. The model was then verified using finite-difference time domain (FDTD) modelling, an independent method. An interesting result of this modelling was the appearance of strong resonances in the emission, and these are explored in Section 2.2.3.

To integrate the diamond nanocrystals with an optical fibre, a hybrid diamond-tellurite glass was fabricated. Characterisation showed that the diamond, and the unique optical properties of the NV centres, survived this process. These results are shown in Chapter 3.

A successful diamond-tellurite glass led to the fabrication of the first suspended core optical fibre structure with embedded ND, and a variation of the design allowed confocal imaging of the fibre core region for direct optical pumping of the embedded NV colour centres. Concluding remarks are then presented in Chapter 5.

2

Modelling

This chapter focuses on development of a theory describing emission of an emitter in the vicinity of an optical fibre. This is then used for numerical analysis of the proposed diamond-fibre device, to better understand the effects of the fibre parameters on the device performance — in this case, the collection of NV colour centre emission from diamond nanocrystals embedded within the glass from which the fibre is made into the fibre guided modes. There are many degrees of freedom in the fabrication of an appropriate fibre and so an accurate computer model of the system is essential. To ensure high efficiency photon collection, the combined fibre & ND system must be understood and optimised. In particular, the effect of core diameter, emitter position and refractive index on device properties must all be understood. Computer modelling plays an important role in exploring this design space as fibre fabrication is relatively costly in time and materials, and some degree of randomness in emitter position is unavoidable.

A suitable model for the emitter-fibre system had to represent the fibres that could be fabricated, as the model would be used to guide this fibre design. In this project a step-index fibre geometry was used to approximate the microstructured geometry. This allowed a reasonably accurate description of the air-clad suspended core fibre that would be fabricated, but at the same time reduced the complexity of the problem such that a (relatively) simple analytical solution was available. this analysis was primarily to see the effects on the collection of emission, and so the simpler step-index model was chosen for a faster, more transparent solution.

The step-index modes of the fibre were used to describe the fields of the combined emitter-fibre system. These fibre modes form a complete basis set, and so can be used to describe the electromagnetic fields of any system. The fields were written in terms of a complete orthogonal basis of modes of the fibre and this modal description could then be used to calculate the expected coupling of emitters to the fibre. The basis set was separated into guided modes of the fibre and radiation modes (all other modes, that

aren't guided, needed to form a complete basis set). The equations for the modes of the step-index fibre are derived in Section A.1.

Once the fibre modes had been found, introducing an emitter allowed investigation into coupling of this emitter to these derived modes. To approximate an NV colour centre, the emitter was modelled as an electric dipole. The derivation of a model that describes the coupling of the emitted light from this dipole into the fibre modes is shown in Section 2.1 (with a complete derivation in Appendix A.3). This model was then used to perform calculations of the expected coupling over the fabrication parameter space.

Single NV centres emit as single photon sources — the emitter is pumped into the excited state, and there is then a delay due to the ∼10 ns lifetime before emitting a photon. The NV emitter cannot emit a second photon during this cycle and so non-classical single photon emission is observed. The emitter in this derivation is described by a classical dipole. However, it has been demonstrated that the classical electrodynamic result can be used to derive certain physical quantities of the quantum system — specifically, for this derivation, spontaneous emission rate (using dipole radiated power) [52, 53, 54, 55] and radiation pattern [56]. The results of this classical description can therefore be applied to the quantum behaviour of NV single photon capture into the fibre modes.

The total emitted power is needed to find the fraction of emission that is coupled to the fibre modes, giving, in the case of the single photon source, the probability that a photon is captured into a guided mode. The emitted power (or, equivalently, emission rate) can change dramatically for an emitter near an interface [57, 58, 59]. In Section 2.2.1, the effect of the fibre geometry on the dipole emission is discussed, and the change to total power is calculated using the radiation modes. Although generally not treated, the radiation modes are required in this case to calculate the total power emitted by the emitter. All of this information can then be used to estimate the efficiency of the fibre device as a collector of single photon emission, although, of course, this modelling is more generally applicable to any dipole emitter.

The results of the model calculations are presented (see Section 2.2) and an interesting consequence of the radiation mode modelling, that of apparent whispering gallery modes (WGMs) excited in the fibre by the emitter, is presented in Section 2.2.3.

Finally, the FDTD method was used to verify the results obtained by the single dipole model (see Section 2.1). FDTD solves for Maxwell's equation directly, and is independent of the method described above. The FDTD method and the results of this investigation are discussed in Section 2.3.

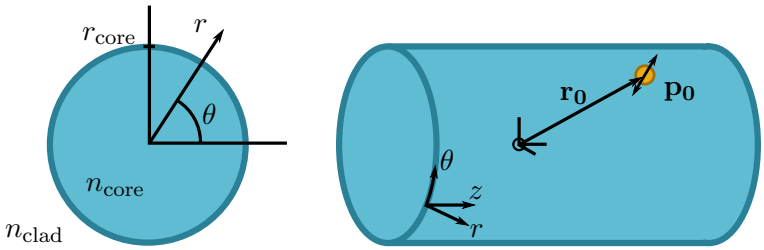

FIGURE 2.1: Diagram of the step-index model with a single dipole.

2.1 Modelling of dipole-fibre coupling

The step-index fibre geometry consists of a cylindrical core of radius r and infinite length with a surrounding cladding that extends towards infinity in all directions (a diagram is shown in Fig. 2.1).

The step-index model is applicable to many different geometries that are able to be fabricated. More specifically, a step-index fibre with an air cladding material is a reasonable approximation to the proposed suspended core structure that is regularly fabricated at our fibre draw facility (excepting possibly for the WGM modelling, discussed in Section 2.2.3, due to the strong dependence on the deformations from a circular core). The step-index model can also be used to approximate a standard step-index fibre (e.g. doped silica) or a multi-ring holed microstructured fibre (e.g. by a stack-and-draw technique). More complex modelling, such as finite-element modelling or a W-profile analytical solution, would allow a more accurate description, showing effects such as confinement loss of the fibre. However, due to the added complexity of these methods, the step-index fibre was chosen for the initial modelling, which captured all of the essential details of the coupling. These more complex methods could then be used if a more accurate representation was required after obtaining the step-index results.

There has been previous study in the area of emitters in the vicinity of optical fibres. Fluorescence capture into fibre guided modes has been modelled [60], although this assumed an isotropic and homogeneous distribution of emitters and did not consider emission changes due to the core-cladding interface. Emission near a dielectric cylinder [58, 59] has been investigated, including spontaneous emission rate and radiation pattern changes. Other interface effects, such as those of planar interfaces [55, 61] or gold nanoparticles [62], have also been modelled and experimentally measured. The treatment shown here is based on derivations of optical fibre mode excitation by current sources in Ref. [63].

The fields of the dipole-fibre system are expanded using the step-index mode basis set — guided modes of the fibre and radiation modes, which are defined as any modes that

are not guided (i.e. all other modes needed in order to form a complete orthogonal basis set). This can be written in the form:

$$\mathbf{E} = \sum_k \Big[\overbrace{a_k(z)\,\mathbf{e}_k e^{-i\beta_k z}}^{+z \text{ propagating guided}} + \overbrace{a_{-k}(z)\,\mathbf{e}_{-k} e^{i\beta_k z}}^{-z \text{ propagating guided}} \Big] + \sum_\nu \int \overbrace{a_\nu(\beta)\,\mathbf{e}_\nu(\beta) e^{-i\beta z}\ \mathrm{d}\beta}^{\text{radiation}}, \tag{2.1}$$

$$\mathbf{H} = \sum_k \Big[a_k(z)\,\mathbf{h}_k e^{-i\beta_k z} + a_{-k}(z)\,\mathbf{h}_{-k} e^{i\beta_k z} \Big] + \sum_\nu \int a_\nu(\beta)\,\mathbf{e}_\nu(\beta) e^{-i\beta z}\ \mathrm{d}\beta, \tag{2.2}$$

where $\mathbf{e}$ and $\mathbf{h}$ represent the modal fields and a is a coefficient that describes the coupling of the emission to the corresponding mode, and will be called a 'coupling coefficient'. The propagation constant, $\beta = k_z$, is discrete for the guided modes ($k_0 n_{\text{clad}} < \beta_j \leq k_0 n_{\text{core}}$) and continuous for the radiation modes ($0 \leq \beta < k_0 n_{\text{clad}}$). Finding every coupling coefficient, a, for a particular system provides the information required to calculate the resulting field for that system, where a is the coupling coefficient to any individual mode. The modal fields, $\mathbf{e}$ and $\mathbf{h}$, of the geometry are vectors representing the components ($\hat{r}$, $\hat{\theta}$, and $\hat{z}$ for example) of the field as a function of spatial position, and are derived for a step-index fibre in Section A.1.

The coupling coefficients must be derived for the case of a single dipole in the vicinity of a step-index fibre. The coupling coefficients will then describe the coupling into the modes of the fibre due to the dipole, positioned either inside or outside the fibre core, and are needed to find the power distribution into the fibre modes (radiation pattern) of the emitting dipole. Figure 2.1 shows a diagram of the model.

The single emitter was modelled as a dipole at position $\mathbf{r} = \mathbf{r_0}$, with a transition frequency ω_f and dipole moment $\mathbf{p} = \mathbf{p}_0 e^{-i\omega_f t}$. The polarisation density, $\mathbf{P}$, associated with this dipole is

$$\mathbf{P} = \sum_{i=1}^{N} \mathbf{p}_i \delta(\mathbf{r} - \mathbf{r}_i) = \mathbf{p}_0 e^{-i\omega_f t} \delta(\mathbf{r} - \mathbf{r_0}). \tag{2.3}$$

And the current density, $\mathbf{J}$, is

$$\mathbf{J} = \frac{\partial \mathbf{P}}{\partial t} = -i\omega_f\, \mathbf{p}_0 e^{-i\omega_f t} \delta(\mathbf{r} - \mathbf{r_0}). \tag{2.4}$$

The derivation then follows that shown in Ref. [63], using the Reciprocity Theorem and the expression for the current density shown above in Equation (2.4). The Reciprocity Theorem is

$$\frac{\partial}{\partial z}\int_{A_\infty} \mathbf{F}_c \cdot \hat{z}\ \mathrm{d}A = \int_{A_\infty} \nabla \cdot \mathbf{F}_c\ \mathrm{d}A, \tag{2.5}$$

with

$$\mathbf{F}_c = \mathbf{E} \times \bar{\mathbf{H}}^* + \bar{\mathbf{E}}^* \times \mathbf{H}. \tag{2.6}$$

The barred and unbarred fields that appear in $\mathbf{F}$ correspond to any two systems. In this case it is useful to define these two systems as: (1) the dipole-fibre system, as in Eqs. 2.1 and 2.2, with a current density as in Eq. 2.4 and (2) a single mode, j, of the step-index fibre. The full derivation is presented in Section A.3. Using Eq. (2.5) together with Maxwell's equations leads to the expression for the coupling coefficients, a_j, for each of the fibre modes j. The coupling coefficients, shown in Equation (2.7), describe the strength of the dipole coupling to the corresponding mode (they are the coefficients of each of the mode fields in the modal total field expansion, see Equation 2.2) and can be used to find the power coupled into each mode.

$$a_j = \frac{i\omega_f}{4N_j} e^{-i\omega_f t} e^{i\beta_j z_0} \left[\mathbf{e}_j^*(\mathbf{r}_0) \cdot \mathbf{p}_0(\mathbf{r}_0)\right], \tag{2.7}$$

where

$$N_j = \frac{1}{2}\int_{A_\infty} \mathbf{e}_j \times \mathbf{h}_j^* \cdot \hat{z}\ \mathrm{d}A. \tag{2.8}$$

The power coupled into each mode is (see Section A.5)

$$P_j = |a_j|^2 N_j. \tag{2.9}$$

Equation 2.7 shows that the coupled power into a mode depends on the dot product of the dipole moment and the mode electric field evaluated at the dipole position.

Similarly, for the radiation modes the coupling coefficients are

$$a_\nu(Q) = \frac{i\omega_f}{4N_\nu(Q)} e^{-i\omega_f t} e^{i\beta z_0} \left[\mathbf{e}^*_\nu(\mathbf{r}_0, Q) \cdot \mathbf{p}_0(\mathbf{r}_0) \right], \tag{2.10}$$

where $Q = r_{\text{core}}(k_0^2 n_{\text{clad}}^2 - \beta^2)^{1/2}$. The total radiation power, due to the integration over Q, is

$$P_{\text{rad}} = \int_Q |a_\nu(Q)|^2 N_\nu(Q) \ \mathrm{d}Q. \tag{2.11}$$

Note that when the total radiation power is defined, all components of the radiation are represented. Looking back, the fields have been expanded in terms of z-propagating modes and so the radiation modes have been defined as a function of Q, which is related to the propagation constant, β. The propagation constant represents propagation down the fibre length (in the z-direction), and integration over Q is required to calculate all the radiation modes — from those travelling close to the guided mode cutoff ($\beta = k_0 n_{\text{clad}}$, where values larger than this are guided) to those propagating completely transverse to the fibre ($\beta = 0$, i.e. no propagation in the z-direction). By defining the power to be the flux in the z-direction, it may not be immediately obvious why this should capture the power in radiation modes with β values close to zero (as they are not propagating along the z-direction). Indeed, this power is captured, and the reason this is the case is because of the integration over the *infinite* cross-section, A_∞. Thus, all power is captured in this expression, because of the integration over an infinite plane.

The capture fraction (CF), which is the fraction of emitted power that is coupled into the guided modes of the fibre, is defined as

$$CF = \frac{P_{\text{guided}}}{P_{\text{total}}}. \tag{2.12}$$

This gives a measure of the performance of the device, given that the useable emission is in the guided power.

2.1.1 Extension to multiple emitters

The previous derivation (see Section 2.1) described coupling of a single emitter to the fibre modes, but there are several interesting cases where extending this treatment to multiple emitters would be useful. It could be used to investigate the effects of multiple single emitters on the single photon source (such as degree of single photon degradation), or the modelling of an NV emitter, where the emission is described by a 2D dipole.

In sensing, a measurable emission pattern change due to the addition of other dipoles would be pertinent (such as for single molecule detection) or for a sensing method where multiple emitters are used (e.g. magnetometry with an ensemble of NV centres).

For multiple emitters, there is now a slightly more complicated expression for the current. For a system of N dipoles: the ith dipole having dipole moment $\mathbf{p_i}e^{i\omega_i t}$ and position $\mathbf{r}_i$. The polarisation density is

$$\mathbf{P} = \sum_{i=1}^{N} \mathbf{p_i} e^{i\omega_i t} \delta(\mathbf{r} - \mathbf{r}_i), \tag{2.13}$$

which gives a current density of

$$\mathbf{J} = \frac{\partial \mathbf{P}}{\partial t} = -\sum_{i=1}^{N} i\omega_i \, \mathbf{p_i} e^{-i\omega_i t} \delta(\mathbf{r} - \mathbf{r}_i). \tag{2.14}$$

The coupling coefficients are obtained by following the same derivation as that for the single emitter above (derived in Section A.3), until the substitution for $\mathbf{J}$. Substituting the new expression for the current density leads to the following equation for the mode coefficients:

$$a_j = \sum_{i=1}^{N} \frac{i\omega_i}{4N_j} e^{-i\omega_i t} e^{\beta_j z_i} \left[\mathbf{e}_j^*(\mathbf{r}_i) \cdot \mathbf{p_i} \right], \tag{2.15}$$

where z_i is the z-position of the ith dipole. The full derivation of Equation 2.15 is in Section A.4. Equation 2.15 shows that the coupling coefficient to the mode for multiple emitters is just the summation of the coupling coefficients for each emitter (compare to Eq. 2.7).

This derivation has not been used for any numeric calculations during this work, although future work could include applying this expression for the applications listed above. The multiple emitter modelling could be expanded by deriving an expression for the case of dipoles with different transition frequencies, and investigating the effect of induced dipoles (e.g. a dipole and an emitter, such that the emitted field excites the dipole) on the derivation shown here.

2.2 Analytical model results

The analytical model described in Section 2.1 was used to explore the behaviour of an emitter in a step-index fibre geometry. Due to fabrication considerations (see Chapter 3), and successful fabrication of an embedded ND-tellurite material, the main focus of the modelling is using tellurite glass [1] as the core material (with a refractive index of ~ 2.025 at 700 nm).

Firstly, the total power emitted by the dipole is calculated in Section 2.2.1. The total power is needed to calculate the fraction of power captured into the guided modes. The guided mode capture is explored in Section 2.2.2, showing the effect of fibre and dipole emitter parameters (fibre core diameter, dipole position, dipole orientation and fibre refractive index contrast). Finally, an intriguing observation found when modelling the radiation modes, that of sharp peaks in the radiation mode power for a z-oriented dipole at the fibre core-cladding interface, is investigated in Section 2.2.3.

The normalised dipole position, ρ, is

$$\rho = \frac{r}{r_{\text{core}}} \tag{2.16}$$

2.2.1 Total power change

The total rate of emitted photons is an important parameter for the modelling of the dipole emission. Here, with the use of a classical dipole, the count rate is instead described by an emitted power, P_{total}. Although the total emitted power is a classical property, it is relevant to the single photon emission as it allows the calculation of the capture fraction, that is the proportion of the NV emission power coupled into the guided modes of the fibre. This will give us a measure of the efficiency of our device as it gives the probability of a generated photon being captured by the fibre (i.e. emitted as a useful output photon), which, as has been mentioned, is an important metric for the proposed single photon source.

In an infinite, homogeneous material the power can be calculated using a simple expression [64],

$$P_{\text{bulk}} = \left(\frac{\mu_0}{\epsilon_0}\right)^{\frac{1}{2}} \frac{\omega^4 n}{12\pi c^2}. \tag{2.17}$$

However, in the case of an emitter within, or in the vicinity of, a step-index fibre there is a non-homogeneous material with large discontinuities in the refractive index. The

emission rate and pattern are not an inherent property of an emitter, they depend on the local density of states of the electromagnetic field. It has been known since experiments by Purcell in the 1940s on radio frequency emission [57], and verified in many other systems [55, 61, 62], that the local environment can alter emission behaviour. The refractive index boundaries modify the local density of states from the free-space behaviour, which in turn can greatly affect the emission rate and pattern of the emitter [57, 58, 59, 65]. In the case of the step-index geometry described above, the total emission will depend on the position and orientation of the emitter, the core diameter and the refractive index of the core and cladding.

This change in power can be calculated using Green's function, as in Ref. [59, 66], or using a modal expansion, as in Ref. [58]. A modal expansion method has been used here, by deriving all modes (guided and radiation) to give a complete basis set — calculating the total power requires the calculation of the power coupled into all modes of the system, i.e.

$$P_{\text{total}} = \sum_{j} P_j + \sum_{\nu} P_{\text{rad}}, \tag{2.18}$$

where P_j and P_{rad} are defined in Eqs. (2.9) and (2.11). In this expression the effects of the local boundaries are inherent in the derivations of P_j and P_{rad}.

Figure 2.2 shows the large changes in total emitted power ($P_{\text{total}}/P_{\text{bulk}}$) that can arise from these interface effects. This figure shows the normalised total power as a function of core diameter. The normalised power is defined as the calculated total dipole power in the fibre divided by the power emitted by the same dipole in a bulk material of the same refractive index (i.e. the ratio of total power with and without any interface effects). A normalised power greater than one therefore represents power enhancement due to the geometry, and less than one represents power reduction. Plots of three different core refractive indices (1.6, 2, and 2.5) show the effect of the interface refractive index contrast on the total emitted power. The total power from the dipole fluctuates as the distance between the emitter and the core-cladding interface changes due to the change in core diameter. This interface reflects emitted power and, by altering the dipole-interface distance, the resulting interference from the back-travelling emission alternates between constructive and destructive. Observe that the power calculated can deviate substantially from the bulk value: for a refractive index of 2 (close to the value for tellurite glass) the total power can vary between 1.55 and 0.55 of the bulk power.

Also, from Fig. 2.2, as the core diameter increases the oscillations reduce and the change in total emitted power approaches 1. A larger core diameter fibre better approximates

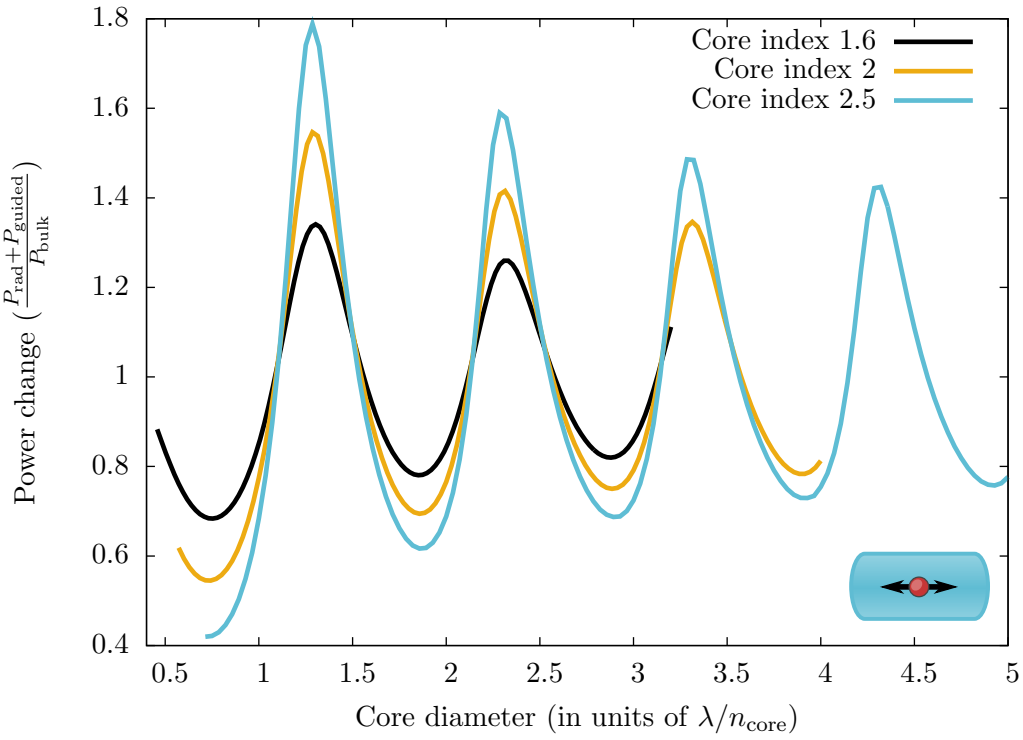

FIGURE 2.2: Plot showing the total emitted power of the dipole versus fibre core diameter for three different core refractive indices; 1.6, 2, and 2.5. Dipole power is relative to the total power emitted by the same dipole in a bulk (infinite and homogeneous) material of the same refractive index. The fibre core diameter has been normalised to the wavelength of emission in the core material (λ/n_{core}). The fibre is a step-index geometry with an air cladding and the dipole is z-oriented, emitting at 700 nm, and is located in the centre of the fibre core. The total power can be seen to fluctuate as the core diameter change causes constructive and destructive interference conditions on the reflected emission.

an infinite and homogeneous material and so the emitted power approaches the bulk material value, as expected.

The normalised power is also shown as a function of dipole position in Fig 2.3 for a selection of core diameters (displayed in the inset), where the dipole position is varied from the centre of the core ($\rho = 0$) out to twice the core radius (the core-cladding interface is at $\rho = 1$). The total power versus core diameter is displayed as an inset to show the location of each dataset in relation to the total power peaks in core diameter. The vertical lines in the inset plot denote the core diameter of the corresponding linestyle in the main plot. Again, the total power is altered dramatically from the bulk value depending on the position of the dipole relative to the core-cladding interface. Note that here the bulk power, P_{bulk}, is the emitted power in tellurite. When the dipole is in the air cladding ($\rho > 1$) the total power is normalised to the higher bulk power value of tellurite (as the refractive index of tellurite is higher, see Eq. 2.17) and so the power change value for emission in bulk air corresponds to $n_{\text{air}}/n_{\text{tellurite}} = 0.49$ (this value

is noted in Fig. 2.3). When this factor is taken into account it can be seen that, as expected, the dipole emitted power approaches that for radiation in air as the distance from the fibre increases (i.e. as ρ increases). Also note that the peak near the core-cladding interface, for the 0.8 µm line, reaches a higher total power than that of the core centre maxima. This peak is due to resonant coupling into the radiation modes and will be discussed further in Section 2.2.3. This resonant coupling at larger core diameters can affect the total power emission to a much higher degree than that shown here, with enhancements of up to 400 times the bulk emission (see Section 2.2.3).

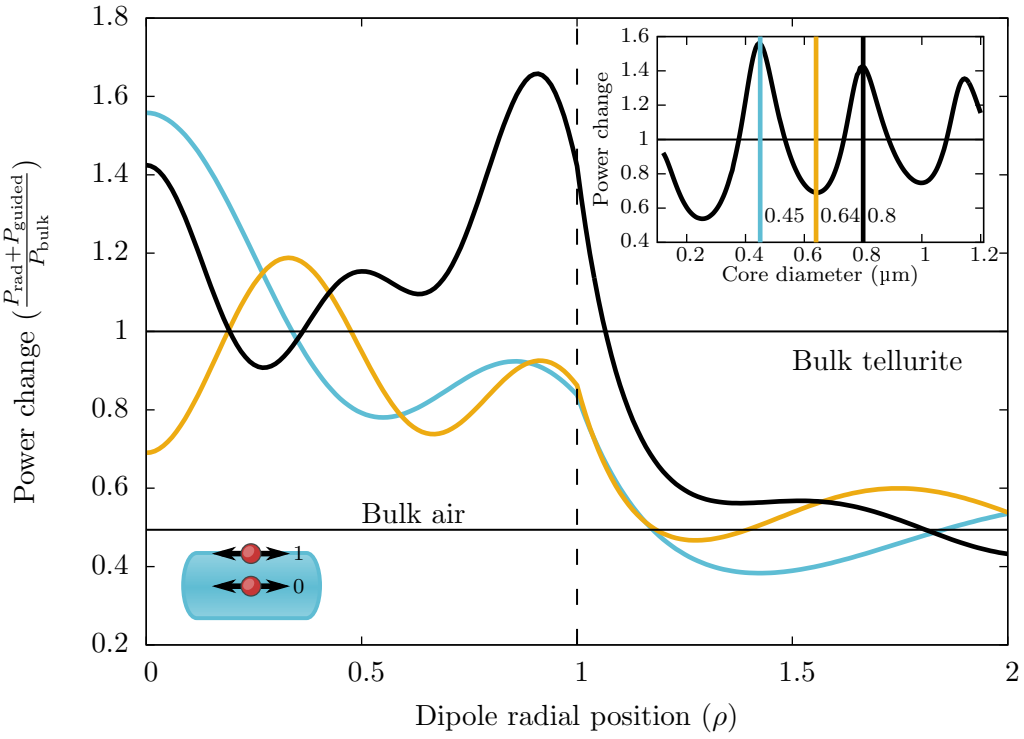

FIGURE 2.3: Total dipole emitted power as a function of dipole radial position for a selection of core diameters. The fibre is a step-index geometry with a tellurite core in an air cladding. The core diameter for each line is shown in the inset plot. The dipole is z-oriented and is radiating at a wavelength of 700 nm. Here $\rho = 0$ corresponds to a dipole in the centre of the fibre, and $\rho = 1$ to a dipole at the core-cladding interface. INSET: total power versus core diameter. The vertical lines match to the line styles in the main plot, showing the corresponding core diameters.

2.2.2 Capture fraction

Calculations of the capture fraction (see Equation 2.12) were performed to investigate the effect of the fibre parameters on the efficiency of the device, as it determines the number of single photons emitted into the guided fibre modes. As described above, a classical description is used to calculate the capture fraction and this is then used to find the probability of single photon emission into a particular mode (in this case the guided

modes). A high capture fraction means that the device will couple a large fraction of the emission, giving a brighter and a more reliably-triggered source. A capture fraction of 1 indicates all emission is into guided fibre modes, and a capture fraction of 0 indicates no emission is into guided modes (i.e. all power is emitted into radiation modes).

The capture fraction depends on the total dipole emission and so will be affected by changes in this emission due to the core-cladding interface, as discussed in Section 2.2.1. The change to the capture fraction, due to this Purcell effect, is shown in Fig. 2.4. Here the capture fraction obtained using the unmodified bulk power ($P_{\text{total}} = P_{\text{bulk}}$) is compared to that using the total power calculated from the radiation and guided mode power ($P_{\text{total}} = P_{\text{guided}} + P_{\text{rad}}$). It can be seen that the interface effects can substantially change the expected coupling of the dipole emission into the guided fibre modes. The difference in the two traces of Fig. 2.4 shows that it is important to use the modal description to calculate the total emitted power and hence the capture fraction, as it differs substantially from the assumption of a homogeneous, isotropic medium.

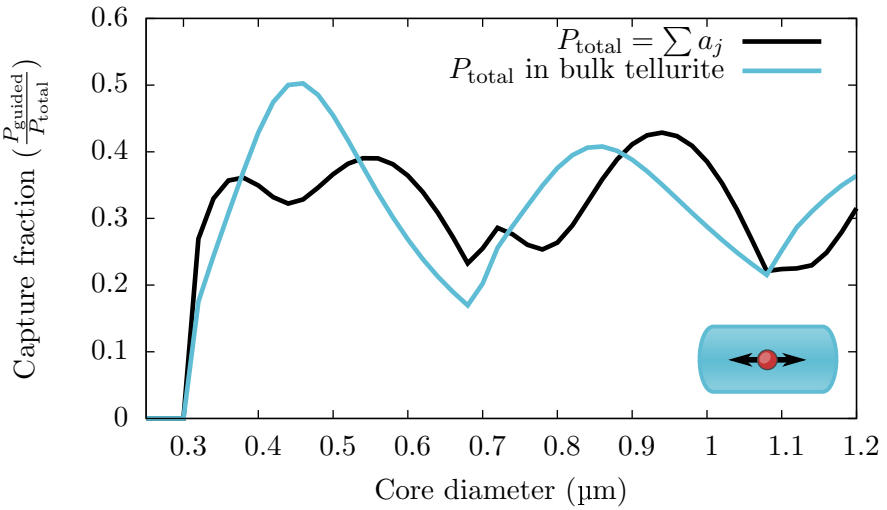

FIGURE 2.4: Comparison between the results for the capture fraction using the modal expansion method and the bulk material expression to calculate the total power. The black line represents capture fraction calculations using radiation and guided modes for total power. The blue line represents calculations for capture fraction assuming the total power emitted is using the bulk material expression (see Eq. 2.17). The dipole is z-oriented and located in the centre of a tellurite core/air clad fibre, emitting at a wavelength of 700 nm.

Figure 2.5 shows the capture fraction for varying core diameters and emitter positions. The fibre is a tellurite step-index fibre with an air cladding. The plots are for radial, azimuthal and longitudinal dipole orientations. The maximum capture fractions obtained from this calculation are shown in Table 2.1.

Sharp features in the capture fraction plots (Fig. 2.5) are due to higher-order guided modes appearing as the core diameter increases (see Fig. 2.6). The capture is enabled

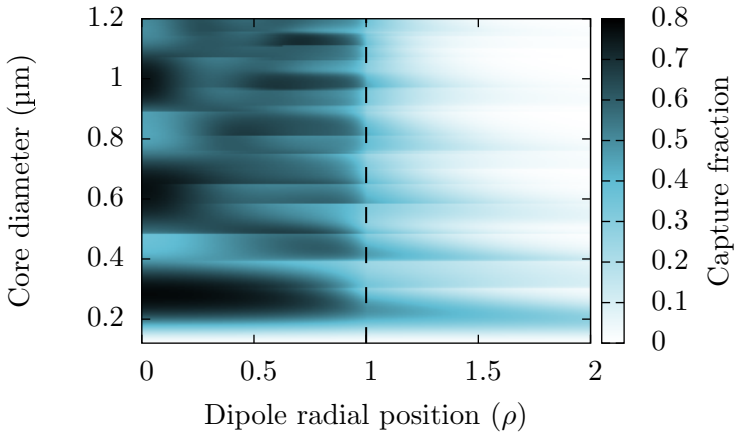

(A) $\mathbf{p} = p_0\hat{r}$

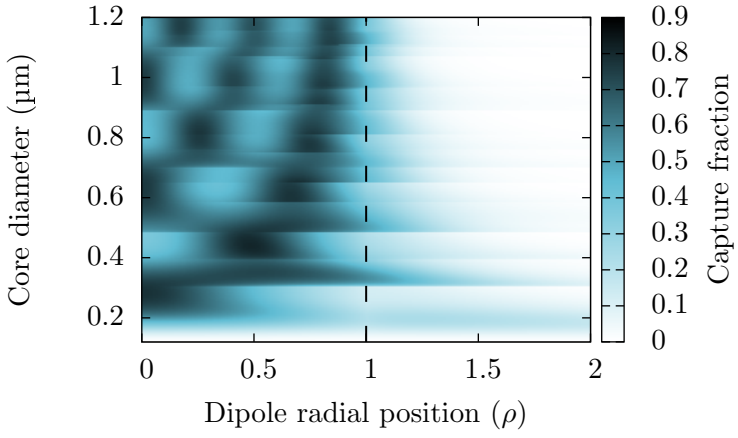

(B) $\mathbf{p} = p_0\hat{\theta}$

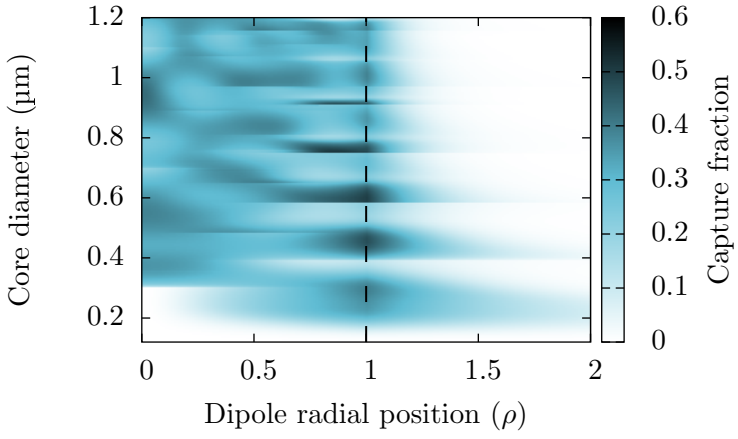

(C) $\mathbf{p} = p_0\hat{z}$

FIGURE 2.5: Capture fraction for varying core diameter and dipole position, for a tellurite step-index fibre in air. Dipole orientation is (a) radial, $\mathbf{p} = p_0\hat{r}$, (b) azimuthal, $\mathbf{p} = p_0\hat{\theta}$, and (c) longitudinal, $\mathbf{p} = p_0\hat{z}$.

Dipole orientation		ρ	Core diameter (µm)	Capture fraction	Guided power ($P_{\text{guided}}/P_{\text{bulk}}$)
Radial	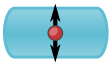	0	0.28	0.78	0.71
Azimuthal		0.5	0.44	0.81	0.71
Longitudinal		1	0.6	0.51	0.41

TABLE 2.1: Maximum capture fractions obtained by varying core diameter and dipole position, for r-, θ-, and z-oriented dipoles. The dipole position and core diameter corresponding to each maximum in capture fraction is shown. The total amount of power that is coupled into the guided modes is also shown (normalised to the power emitted in bulk tellurite).

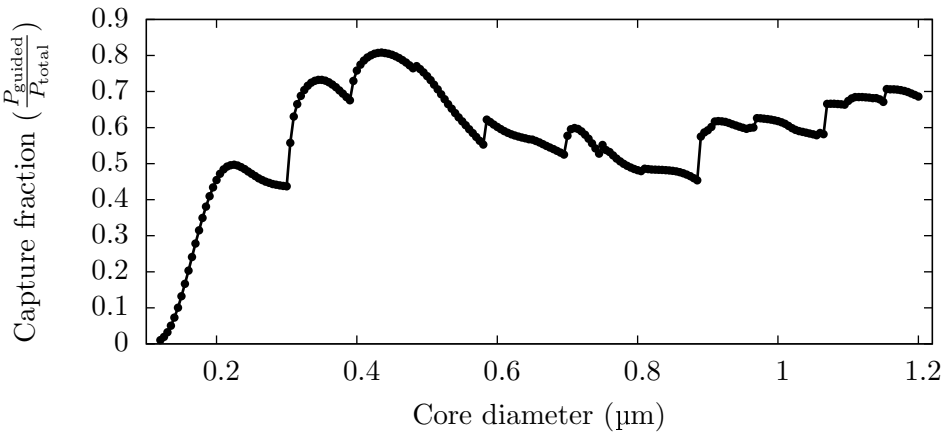

FIGURE 2.6: A slice through $\rho = 0.5$ of the azimuthal dipole capture fraction data shown in Fig. 2.5b, showing sharp features due to higher-order guided modes.

by the modal field overlap with the dipole moment of the emitter (described by the electric field-dipole dot product term in the coefficient expression, see Equation 2.7) and so the coupling is proportional to the electric field magnitude. For example, at small core diameters (less than 0.2 µm in Fig. 2.5) the capture fraction rapidly drops to zero. At these core diameters the fibre mode is only weakly affected by the sub-wavelength core and the mode spreads considerably into the cladding region, which decreases the local electric field (of all field components) at the dipole position and hence decreases emission capture.

Another example of this effect can be seen in the longitudinally- (z-) oriented dipole plot (Fig. 2.5c). Note the cases of no capture for small core diameters and positions near the fibre centre. This is due to the peculiarities of the longitudinal electric field (E_z). At the fibre centre ($\rho = 0$) only the TM modes exhibit a non-zero E_z field component — in all other modes this component is zero at the centre. Like other higher-order modes, these TM modes also have a cut-off value and so do not exist below a defined core diameter. This means that, below this core diameter, no TM modes exist and so there can be

no coupling from the z-oriented dipole into the guided modes. Figure 2.5c shows the TM_{01} mode appearing (when the core diameter is large enough to support this mode) as a sharp increase in capture fraction at approximately 0.3 µm for a dipole position of $\rho = 0$. As the E_z component of the fundamental, HE_{11}, mode is non-zero away from the core centre, guided mode capture for these dipole positions can be seen below the TM_{01} cut-off core diameter. This effect is also discussed in Section 2.3.1.

Note that the capture fraction gives only the probability of capture into the guided modes, and does not give any information about total fibre coupled power. As discussed in Section 2.2.1, the emitted power of the dipole can be greatly affected by the fibre structure and this can lead to a high power output into the guided modes.

Refractive index contrast

The refractive index contrast between the core and cladding of the fibre affects the fibre NA, and so will also affect the amount of single photons captured by the fibre. Indeed, the capture fraction of the fibre depends strongly on the core-cladding refractice index contrast, as can be seen in Fig. 2.7. This figure plots the maximum capture fraction obtainable for a radially-oriented dipole as the cladding index is changed from air ($n = 1$) to very close to the core index ($n_{\text{core}} = 2.025$). Unsurprisingly, a large index contrast is best for a high capture efficiency — indicating that a suspended core design, with a maximal index contrast (glass to air), is advantageous for capture. However, capture for a typical low index contrast doped-core fibre (for comparison, a value of $\Delta n \sim 5 \times 10^{-3}$ [67] for Corning SMF-28 silica telecommunications fibre) reduces to a few percent.

2.2.3 Whispering Gallery Modes

In the step-index fibre, WGMs exist due to the circular cross-section. The longitudinal invariance of the fibre means that these modes do not have a predetermined position. However, this invariance is broken by the introduction of the dipole, and the dipole position then defines the WGM — realising a self-aligned cavity. This effect will be discussed below (see Section 2.2.3.2), after first confirming that the resonances seen in the fibre geometry are indeed due to WGMs.

Sharp peaks were seen in the total emitted power of the dipole when plotted as a function of core diameter, using the analytical expressions derived here. These peaks were seen when a longitudinal (z-oriented) dipole was located at the core-cladding interface of the step-index fibre. Figure 2.8 shows these peaks in total power, with the contributions to

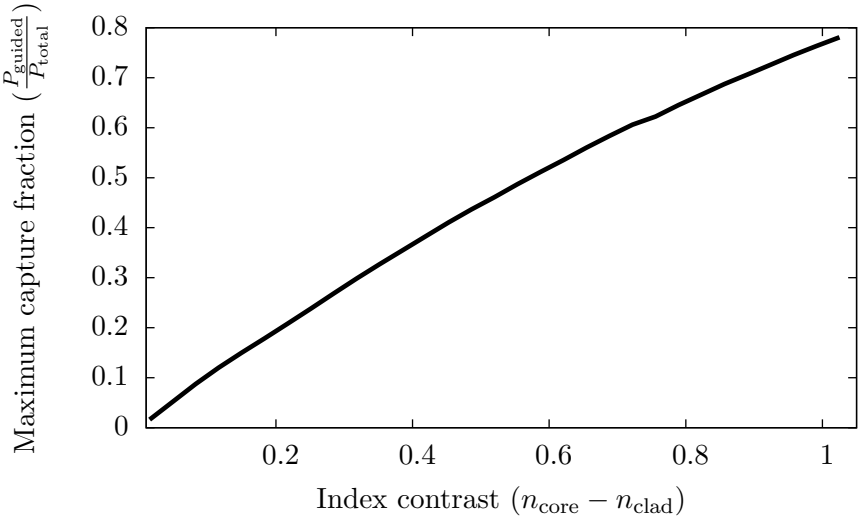

FIGURE 2.7: Maximum capture fraction that can be obtained as a function of cladding index. The fibre is a tellurite ($n = 2.025$) core step-index geometry and the emitter is radially-oriented and positioned in the centre of the core. This is the maximum capture that can be obtained by searching over core diameter.

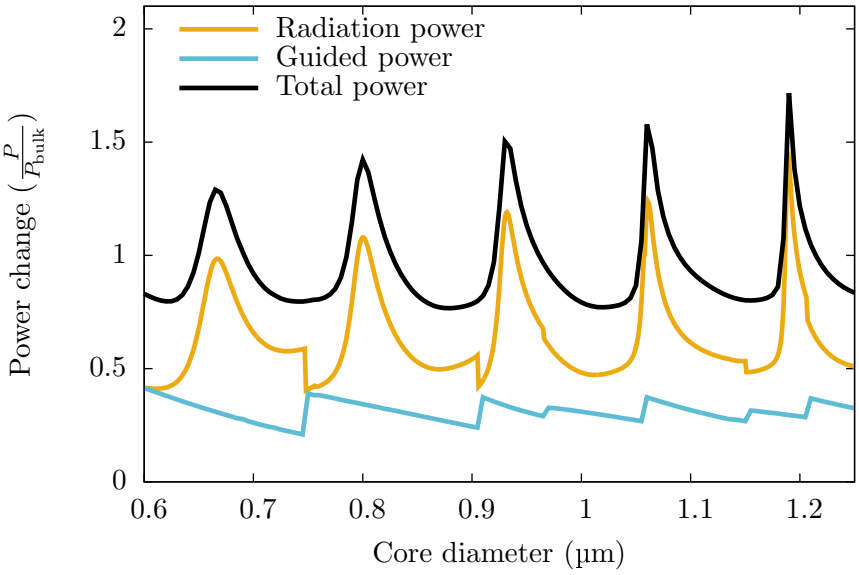

FIGURE 2.8: Total power emitted by a dipole (black) as a function of core diameter, with the contributions from radiation modes (orange) and guided modes (blue). Dipole is z-oriented, positioned at the core-cladding interface of a step-index fibre and emitting at 700 nm. The fibre has a tellurite core with an air cladding. The power has been normalised to that emitted in bulk tellurite (see Eq. 2.17).

this total power from guided modes and radiation modes of the fibre. It can be seen from Fig. 2.8 that the peaks originate from the fibre radiation modes and appear to be independent of guided mode power. The peaks were verified using the FDTD method, and this is presented in Section 2.3.4.

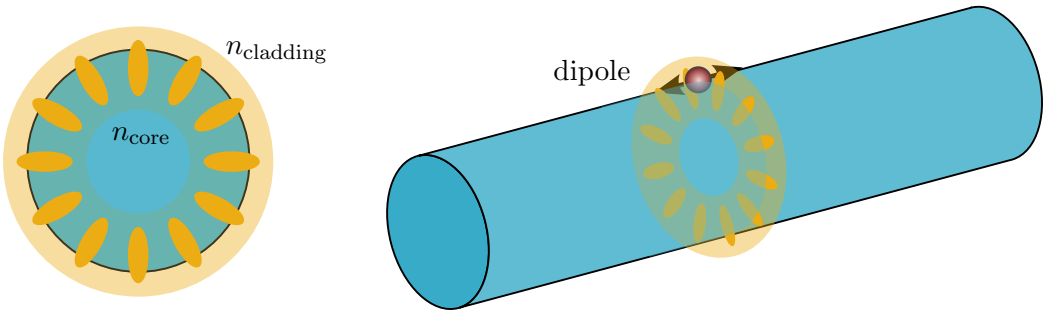

FIGURE 2.9: Schematic showing a WGM resonance in a step-index fibre geometry, and the emitting dipole at the core-cladding interface.

The peaks were attributed to WGM resonances travelling around the fibre circumference (transverse to the fibre propagation direction). The fibre geometry allows these resonances because of the circular cross-section and core-cladding index contrast (see Fig. 2.9), and the reasons for this identification are discussed in detail below (see Section 2.2.3.1). In brief, the longitudinal electric field (E_z) in the cross-section of the fibre matches well with that expected of a WGM and the position of the resonance peaks matches with WGM modelling results. Calculations of individual peaks, in Section 2.2.3.2, also show that a large component of the peak consists of radiation power that is travelling transverse to the fibre axis (which is the expected direction for WGMs, see Fig. 2.9).

WGMs have been solved by a variety of different methods and for a large range of structures, such as a bent waveguide approach for ring resonators [68, 69], finding solutions for complex frequencies [70] in disk or ring resonators, the finite-element method in disk resonators [71], and the FDTD method [72]. Here, the WGMs appear naturally in the radiation modes rather than being explicitly calculated, and a step-index fibre mode basis set is used to describe the coupling of the emitter into the WGM, as in Refs. [58] and [66]. Also, the modelled system is a dipole coupled to an optical fibre. The WGM cavity effects cannot be separated, and any calculated resonance parameters (such as Q-factor) are properties of this coupled system.

The following discussions involve concepts that are very similar in nomenclature, but very different in definition — such as 'mode', which can apply to fibre guided modes, fibre radiation modes, and whispering gallery modes, and trans-electric (TE) and trans-magnetic (TM) labelling, which can apply to any of these modes and are distinct due to perpendicular propagation directions for fibre modes and WGMs. Setting a consistent nomenclature is thus important. Here, modal solutions of the step-index fibre will be called fibre modes, and these are separated into guided modes and radiation modes, as in the previous sections. Solutions of the pure WGM solution will be called WGMs or WGM modes. WGMs will be numbered with brackets, such as TE(l, m), to be distinct

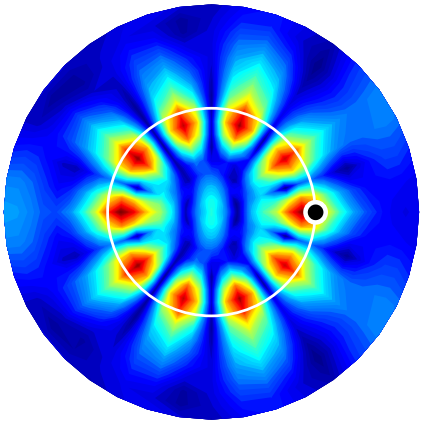

FIGURE 2.10: S_z pattern of the coupled radiation modes showing a WGM resonance for a z-oriented dipole at the core-cladding interface, calculated by the analytical step-index method. The core is overlaid as a white circle and the dipole location is shown as a small black circle. The dipole is emitting at 700 nm. The step-index fibre has a tellurite core with an air cladding and a core diameter of 0.8 µm. Note that the pattern is a superposition of all the radiated power and so some features (such as the central peak) may be due to Fabry-Perot type resonances or other background radiation.

from the fibre mode labelling TE_{lm}, and will be described explicitly, e.g. 'WGM TE mode'. This distinction is made because of the difference in propagation direction, for example the WGM TE mode is propagating in the plane of the fibre cross-section and this means that $E_\theta = 0$, in contrast to a *fibre* TE mode where $E_z = 0$.

2.2.3.1 Identification through field patterns and peak positions

As found in the previous sections (see sections A.3 and 2.3.1), the degree of coupling between a mode and a dipole depends on the dot-product of the electric field and the dipole moment. In the case of WGMs there is a large z-component to the electric field at the anti-nodes for the WGM TE modes. A z-oriented dipole at one of these anti-nodes will couple strongly to the corresponding WGM, and so it would be expected that some amount of coupling to this type of mode would be seen in the system described here based on the fibre geometry.

The radiation mode electric and magnetic fields for a core diameter corresponding to a resonance (at 0.8 µm, see Fig. 2.8) was calculated and plotted in the r-θ plane and the resulting field pattern for S_z (see Fig. 2.10) resembled that of a WGM pattern. The WGM can be clearly seen among the background emission pattern (due to other emission that wasn't coupled into the WGM), indicating strong coupling into this mode. This pattern was verified using the FDTD method (see Section 2.3.4).

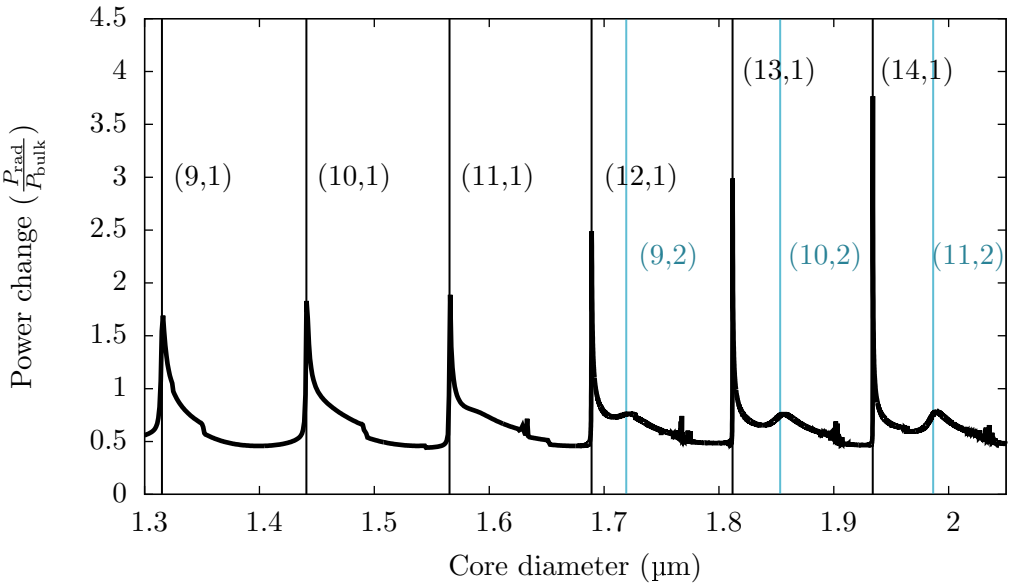

FIGURE 2.11: Radiation power versus core diameter, with WGM TE modal solutions for comparison. The WGM TE modes are labelled with the azimuthal and radial orders as (l, m). The emitting dipole is z-oriented and positioned at the core-cladding interface of a step-index fibre consisting of a tellurite core with an air cladding. Dipole emission is at 700 nm. The power has been normalised to that emitted in bulk tellurite (see Eq. 2.17).

The radiation mode peak positions were also compared to the calculated position of WGM modal solutions. The radiation power is plotted as a function of core diameter in Fig. 2.11, with vertical lines denoting the calculated core diameters of the supported 2D microdisk WGM modal solutions. The expected WGM peak positions match very well to the radiation mode peaks. This result, together with the field pattern in Fig. 2.10, suggests that these radiation peaks are due to WGM resonances. The WGM modal solutions were calculated using the dispersion relation (which can be derived from Refs. [68, 70]) for the WGM TE modes,

$$J'_m(k_0 n_{\text{core}} r_{\text{core}}) H_m^{(1)}(k_0 n_{\text{clad}} r_{\text{core}}) - H_m^{\prime(1)}(k_0 n_{\text{clad}} r_{\text{core}}) J_m(k_0 n_{\text{core}} r_{\text{core}}) = 0 \qquad (2.19)$$

where m is the azimuthal WGM mode number, and J and H are the Bessel and Hankel functions, respectively.

Note that the peaks show a pronounced asymmetric 'tail' on the large core diameter side. This asymmetry is due to leaky skew ray modes propagating along the fibre length [73], and will be discussed further in Section 2.2.3.2.

2.2.3.2 Coupling changes: radiation pattern narrowing

The narrowing in linewidth associated with higher-order WGM (larger core diameters) is fundamentally due to the increase in Q-factor of these WGM. Interestingly, the Q-factor of the higher-order WGM approaches that of a pure WGM modal solution, as discussed in Section 2.2.3.3, despite a lack of longitudinal confinement in the fibre design. Peak broadening, due to this longitudinal invariance, has been seen previously for capillary WGM [73] and shows the same extended tail at the shorter wavelength (longer core diameter) side of the resonance. The cause of this broadening is due to skew ray modes [73] (WGM-like spiral modes that propagate longitudinally), and these modes can be seen in the results of the model presented here. The model results indicate that skew rays may not be a significant cause of peak broadening for all of the WGM resonances in the fibre.

Figure 2.12 shows two WGM resonance peaks, at core diameters of 1.689 µm and 3.7 µm, for 700 nm wavelength excitation. Plotted on the same graphs are the contributions from different ranges, or bins, of z-propagation constant, β. This shows that for small core diameters, or equivalently low azimuthal order WGM, the resonance peak consists of dipole emission coupling to many different β ranges. Recall, from Section 2.1, that $\beta = 0$ corresponds to radiation travelling perpendicular to the fibre propagation direction and increasing β values give radiation power contributions closer to the fibre direction (see Fig. 2.13). This means that the lower order WGM peaks are a mix of pure WGM (for which $\beta = 0$) and 'leaky', or z-propagating, skew ray modes (for which $\beta > 0$). Compare this to the case of a higher order WGM, as shown in Fig. 2.12b, where the resonance peak consists mainly of β-values very close to 0. The WGM resonance is strong enough that almost all of the radiated power is coupled only into this pure WGM.

Comparing the Q-factor of the WGM here to those obtained from the pure WGM solutions (see Table 2.2) showed that for the (azimuthal) higher-order modes, the coupled dipole-cavity approaches that of the pure modes. This is unexpected because of the lack of confinement in the longitudinal direction, where it would be expected that emission leaking down the fibre length (i.e. skew rays) would reduce the coupled Q-factor. The Q-factor is calculated [70] by

$$Q = \frac{\mathrm{Re}(n_{\mathrm{eff}})}{2\,\mathrm{Im}(n_{\mathrm{eff}})} \tag{2.20}$$

for the pure WGM, where n_{eff} is the calculated (complex) effective refractive index of the WGM, and by

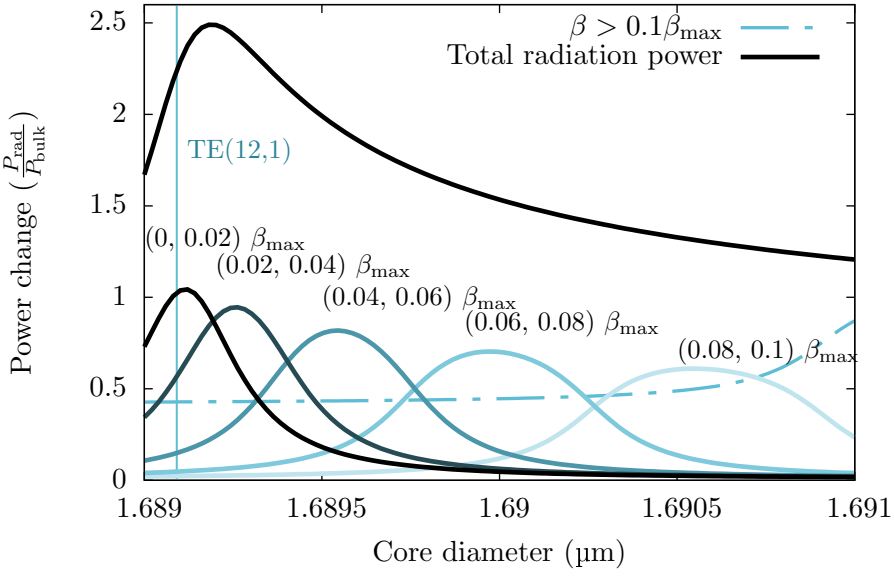

(A)

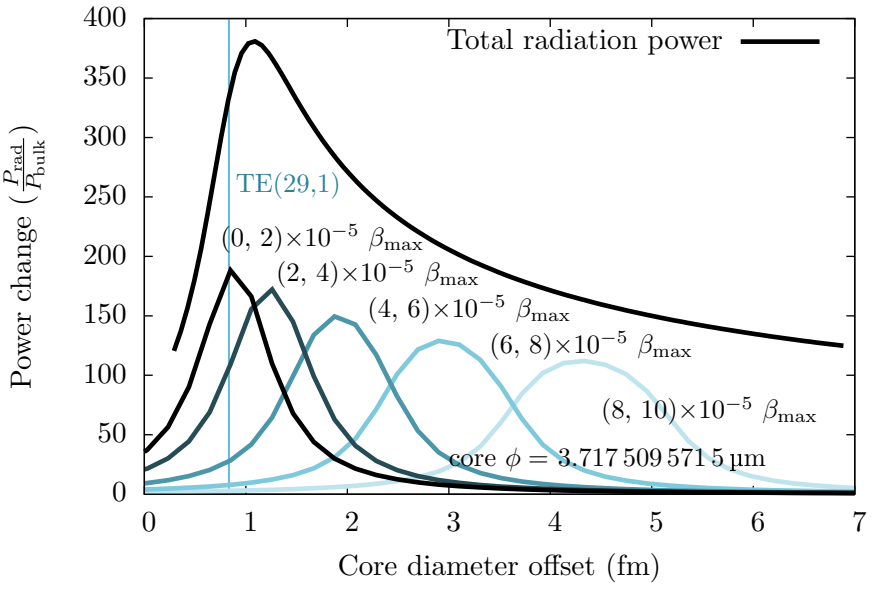

(B)

FIGURE 2.12: Resonance peaks at core diameters of (a) 1.689 µm and (b) 3.7 µm, showing the contributions from the different β components of the radiation modes. Also shown are the core diameter values for the WGM modal solutions TE(12,1) and TE(29,1) on figures (a) and (b), respectively. The power has been normalised to that emitted in bulk tellurite (see Eq. 2.17). The resonance at 3.7 µm has a larger component of the peak at small values of β (note the factor of 10^{-5}), which corresponds to radiation angles close to perpendicular. Note that (b) is plotted versus the offset from a core diameter of 3.717 509 571 5 µm (and is in units of fm) as this resonance peak is very narrow. The corresponding values for wavelength and refractive index were to the same precision, with $\lambda = 700.000\,000\,000$ nm and $n_{\text{core}} = 2.024\,982\,213\,988\,1$.

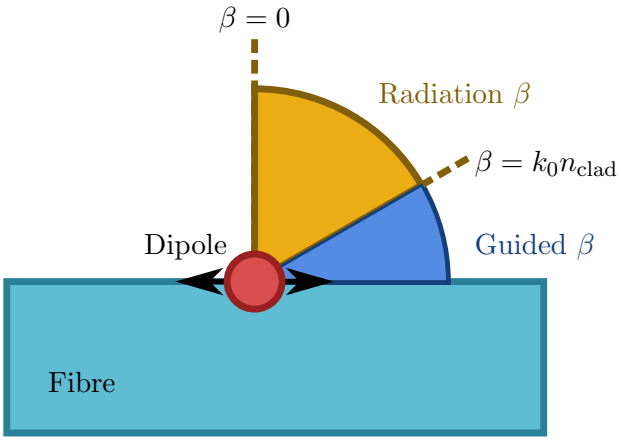

FIGURE 2.13: Schematic showing a representation of β for radiation modes.

Core diameter (µm)	WGM TE mode	Resonance peak Q	Pure WGM Q
1.689	12,1	2000	4971.5
3.7	29,1	1.3×10^9	4.4×10^9

TABLE 2.2: Comparison between the resonance Q-factor obtained from the resonance peaks modelled here and those obtained by WGM solutions. The WGM TE modes shown here are displayed in Section 2.2.3.3.

$$Q = \frac{\omega_{\text{res}}}{\Delta\omega} \tag{2.21}$$

for the coupled dipole-resonator modelling shown here, where ω_{res} is the resonance frequency and $\Delta\omega$ is the full-width half maximum linewidth.

From this modelling, it can be seen that the lower-order WGM resonances have a wider linewidth because of the increased coupling to leaky radiation modes. The narrow linewidth of the higher-order WGM is also explained, as the emission is not coupled to the leaky z-propagating modes and so the linewidth approaches that of a pure WGM. This shows that, theoretically, the quality of the fibre as a cavity may not be limited by the lack of longitudinal confinement. This means that, for the specific fibre designs where this effect occurs, no alignment to a cavity needs to be made — as long as the emitter is z-aligned it will couple to a pure WGM at any point along the fibre.

2.2.3.3 Sensitivity to refractive index change

As WGMs are resonances, the peak positions are very sensitive to changes in the resonator geometry. Conventional WGM resonators have been successfully used in different

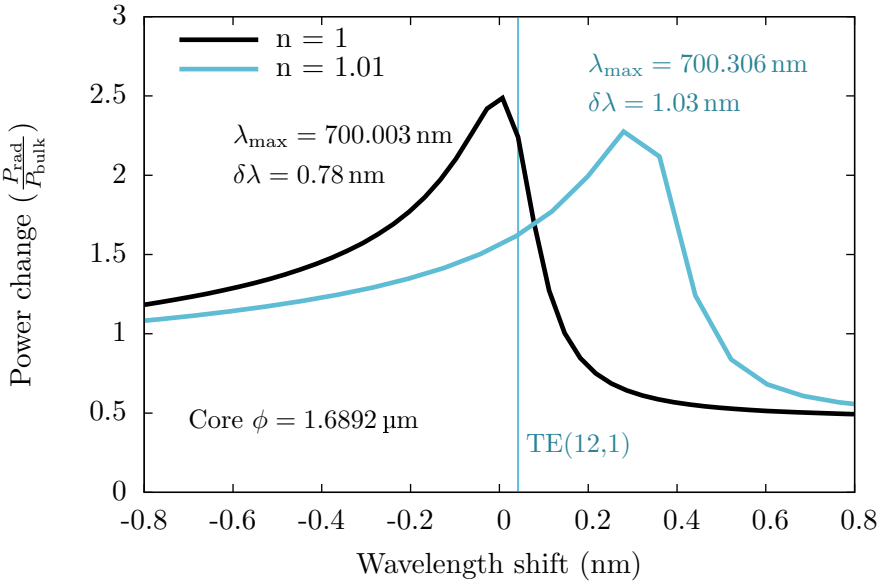

(A)

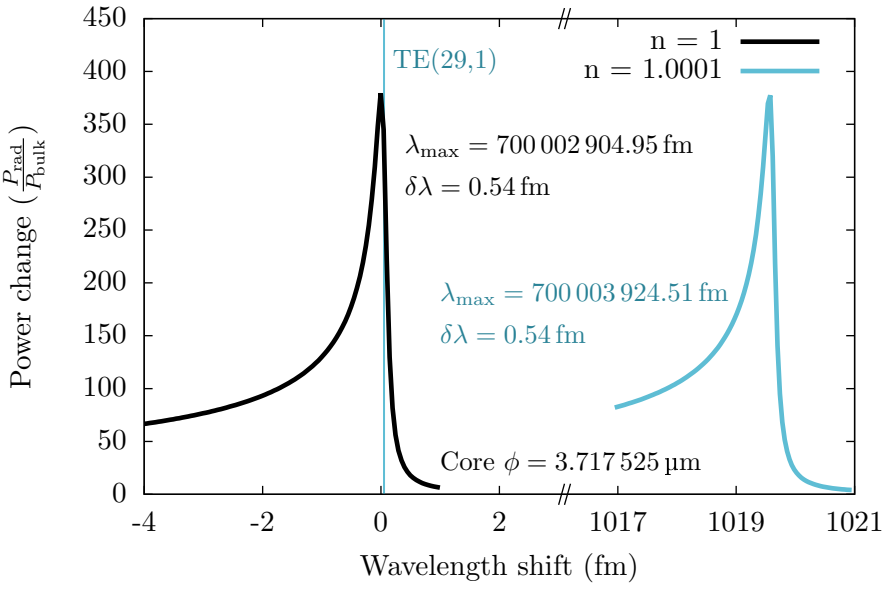

(B)

FIGURE 2.14: Shift in the resonance peak due to a change in the cladding refractive index from (a) 1 to 1.01 for a 1.689 µm core diameter and (b) 1 to 1.0001 for a 3.7 µm core diameter. Also shown are the wavelength values for the WGM modal solutions TE(12,1) and TE(29,1) on figures (a) and (b), respectively. The fibre is a step-index geometry and has a core refractive index of 2.025. The dipole is z-oriented and located at the core-cladding interface of the fibre.

sensing archetectures, such as refractive index sensors (see e.g. [74]). The WGMs seen here, in the fibre geometry, showed a shift in resonance wavelength, as expected, when the cladding refractive index was changed. This can be seen in Fig. 2.14, where the radiation power is plotted vs. wavelength for two different cladding refractive indices.

The sensitivity of the peaks to the refractive index change increases as the core diameter increases, which follows from the higher Q-factor of these WGMs. The linewidths of the WGM peaks decrease at the same time, both positively and negatively affecting the sensing potential of the device. The narrowing linewidth increases the resolution of the refractive index measurement, due to an increased ability to distinguish a change in the peak position. Conversely, the linewidth becomes so narrow for the higher order modes that numerical modelling of the resonance becomes difficult and suggesting challenging experimental detection (with linewidths of e.g. <1 fm).

2.2.3.4 Fabry-Perot type mode peaks in total power

The total dipole emission power is shown in Fig. 2.15a for a range of core diameters and dipole positions. As shown previously (see Eq. 2.16), the normalised dipole position, $\rho = r/r_{\text{core}}$, corresponds to a dipole in the centre of the fibre at $\rho = 0$ and to a dipole at the core-cladding interface at $\rho = 1$. Figure 2.15a shows peaks in the total power in addition to the WGMs. The WGMs correspond to the areas of high power emission nearest to the core-cladding interface (which is $\rho = 1$ on the y-axis), but other peaks in the core region can be seen. For example, at positions (0.45 µm, 0), (0.8 µm, 0) or (0.6 µm, 0.4) on Fig. 2.15a.

From a simple argument of reflections from the core-cladding interface, it could be expected that Fabry-Perot type resonances are present. Following this thought, the resonance condition would be given by

$$2\pi m = \begin{cases} 2\pi \frac{2Ln_{\text{core}}}{\lambda_0} + \pi & \text{for} \quad 0 < r < r_{\text{core}} \\ 2\pi \frac{2Ln_{\text{clad}}}{\lambda_0} & \text{for} \quad r_{\text{core}} < r < \infty, \end{cases} \tag{2.22}$$

where L is the distance to the interface, n is the refractive index of the material, m is an integer, and λ_0 is the free-space wavelength of the emission. The addition of π accounts for the phase-shift of a reflection from a higher to a lower refractive index boundary, and so these equations assume $n_{\text{core}} > n_{\text{clad}}$.

The distance to the interface, L, relates to the normalised dipole radial position, ρ, and the core diameter, r_{core}, by

$$L = \begin{cases} r_{\text{core}} - \rho\, r_{\text{core}} & \text{for} \quad 0 < \rho < 1 \quad \text{short side} \\ r_{\text{core}} + \rho\, r_{\text{core}} & \text{for} \quad 0 < \rho < 1 \quad \text{long side} \end{cases} \tag{2.23}$$

Rewriting these resonance conditions in terms of core diameter and fractional dipole position gives

$$\rho = \begin{cases} 1 - \frac{\lambda_0(m-\frac{1}{2})}{2n_{\text{core}}r_{\text{core}}} & \text{for} \quad 0 < \rho < 1 \quad \text{short side} \\ \frac{\lambda_0(m-\frac{1}{2})}{2n_{\text{core}}r_{\text{core}}} - 1 & \text{for} \quad 0 < \rho < 1 \quad \text{long side} \end{cases} \tag{2.24}$$

Lines corresponding to the Fabry-Perot type resonance conditions are plotted in Fig. 2.15b using Eq. (2.24), which relates dipole position to core diameter, and $m = 1$ to 7. These conditions show a qualitative agreement to the positions of the peaks, indicating that they may be related to Fabry-Perot type resonances.

2.3 Finite-difference time domain method: validating the analytical model

The FDTD method [75] was explored for use as an independent validation of the above analytical expressions. FDTD solves Maxwell's equation directly — the method is independent of the analytical expressions that were derived above, and so serves to verify the results from the model. Several results obtained from the analytical model were checked in this way and these are outlined below.

One point of note is that FDTD calculates the total field instead of a modal decomposition as for the analytical method. This means that the field calculated includes all of the radiation and guided mode fields together, with no simple way to deconvolve them. The guided power needed to be calculated independently from the total power, and so a long length of fibre and a long simulation run time were used to spatially separate the guided emission from the radiated emission. Radiated emission has a minimum propagation angle, due to the guided mode capture, and, due to this angle, long propagation lengths increase the distance of the radiation power from the fibre. Guided modes are transversally invariant along the fibre length and so this propagation spatially separates the two classes of modes. Also, there is no information on the amount of power coupled into each separate guided mode unless the field is deconvolved.

As the computational domain must be finite (due to limited computer memory), perfectly-matched layers (PMLs) [76] were used on all sides of the domain to reduce reflections at the boundary and so approximate an unbounded simulation space.

The software package Meep [77, 78] was used to perform these calculations on a quad-core 3.4 GHz AMD Phenom II 965 processor with 4 GB of random access memory (RAM)

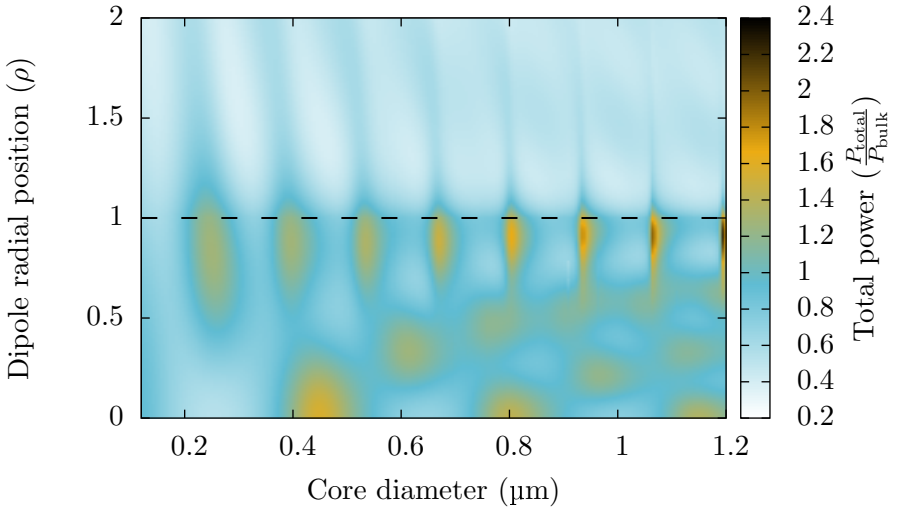

(A) Total power

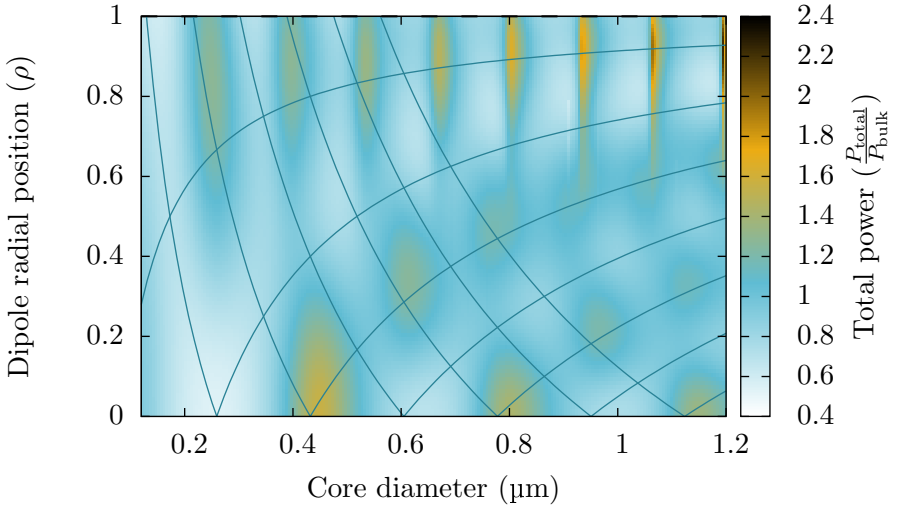

(B) Fabry-Perot type resonances

FIGURE 2.15: (a) Total emitted power versus core diameter and dipole location. The dashed line shows the core-cladding interface. (b) Same contour plot as for (a), but with lines to indicate the curves matching the Fabry-Perot interference conditions for $m = 1$ to 7. For both plots, the fibre is a step-index geometry and has a tellurite core with an air cladding. The dipole is longitudinally (z-) oriented and emitting at 700 nm. The features match well with the Fabry-Perot resonance conditions.

(8 GB for the capture fraction FDTD modelling in Section 2.3.3) running a Kubuntu Linux operating system.

2.3.1 Selective mode coupling

Equation (2.7), which expresses the mode-coupling of the single dipole emission, shows that the coupling coefficient is proportional to the dot product of the electric field and the dipole polarisation:

$$a_j \propto \mathbf{e}_j^*(\mathbf{r}_0) \cdot \mathbf{p}_0(\mathbf{r}_0). \tag{2.25}$$

Looking at the special case of a z-oriented dipole in the centre of the fibre core, $e_z(0,0,0) = 0$ for all modes except TM (see Equation A.16). This means that, according to the analytical model introduced in Section 2.1, emission should couple only into the TM_{0n} modes for a dipole in this position and orientation. This effect is also discussed in Section 2.2.2.

This prediction was verified by modelling a long section of fibre with an emitter placed in the location described. A long section of fibre was needed because the FDTD modelling does not give us a modal field expansion, instead only calculating the total field. To see the excited fibre modes, they first need to be separated from the rest of the dipole radiation. One way to do this is to propagate the fields for a long distance — the fibre modes will be guided and so retain their transverse shape, while the radiation modes will propagate in all directions and are not confined to the fibre. This can be seen in Fig. 2.16, where the flux in the z direction is calculated in a region that is the same size as the fibre core, at different points along the fibre length. The flux is defined as

$$S_z = \int_{\text{surface}} (\mathbf{E} \times \mathbf{H}) \cdot \hat{z} \ \mathrm{d}S \tag{2.26}$$

where $\hat{z}$ is a unit vector in the z direction, the integral is over the surface and S_z is then the z component of the Poynting vector. The flux reaches a constant value after ~80 µm of propagation, for a core diameter of 1 µm and refractive index of 1.4 with an air cladding. The emission wavelength is 700 nm and the dipole is z-oriented and located in the centre of the fibre core.

Figure 2.17 shows the E_y field at an x-z slice through the origin. The dipole is located to the left side of the image. The emission can be seen radiating in all directions, but notice the emission separating into guided and radiation power as it travels down the

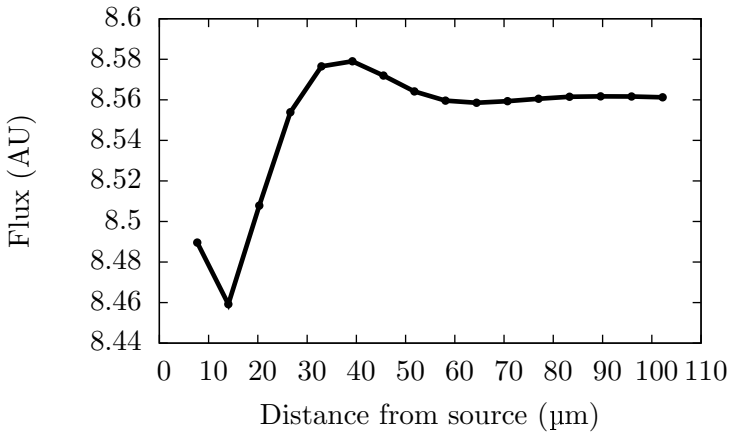

FIGURE 2.16: FDTD calculated flux through the fibre core as a function of position along the fibre length (z). The fibre is a step-index air-clad geometry with a core diameter of 1 µm and refractive index of 1.4. The emitter is z-oriented, located in the centre of the core at the beginning of the fibre, and emitting at a wavelength of 700 nm. Notice that the flux is constant after a distance of approximately 80 µm for this fibre.

fibre. This is due to the acceptance angle of the fibre, a portion of the radiation off-axis to the fibre is still captured and guided. The guided mode profile is also invariant along the z-axis apart from an oscillation as expected.

The E_y field, shown in Fig. 2.17, appears to have the expected ring-like shape of the TM_{01} mode. To verify that this propagating mode was indeed the TM_{01} mode, the transverse profile (x-y slices) of the fields were also compared to the expected fields in a step-index fibre. Shown in Fig. 2.18 are the electric fields and Poynting vector obtained from the end of the fibre in the FDTD calculation, and the same fields for the TM_{01} mode calculated from the analytical step-index solution. This figure compares the two sets of fields, giving good agreement in the core and thus verifying that coupling is only into the TM_{01} mode as expected. The results differ outside the core area, but this is expected due to the radiated field computed in the FDTD that does not exist in the pure analytical expression for the mode.

In summary, the FDTD results indicate that only the TM_{01} guided mode is excited (the only TM mode solution for this fibre) and this agrees with the predictions of the step-index model. Validation of the total power and capture fraction calculations, also using FDTD, will now be shown in sections 2.3.2 and 2.3.3, respectively.

2.3.2 Total emitted power

The total power emitted by the dipole was calculated in the analytical model by summing the power in all the guided and radiation modes, due to changes in the emitted power from a Purcell effect (see Section 2.2.1). This power change, caused in this case by close

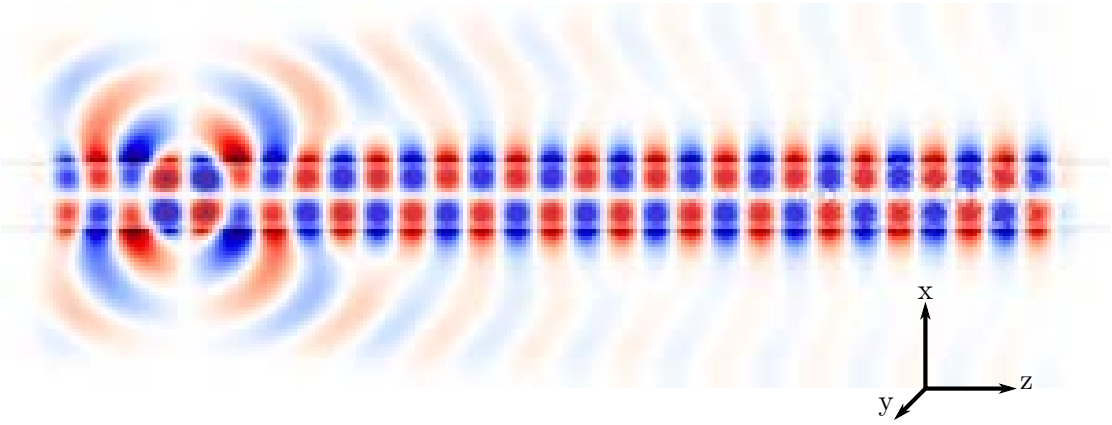

FIGURE 2.17: E_y field for a z-oriented dipole at the centre of the fibre. The core is overlaid in grey and the two colours (red and blue) distinguish positive and negative field directions. The structure consists of a core of diameter 1 µm and refractive index of 1.4 in air. Only the TM_{01} mode of the fibre is coupled into (see Fig. 2.18 for TM_{01} field distributions).

proximity to the core-cladding interface, can be significant when compared to the power emitted by the same dipole in an infinite homogeneous (bulk) material. Here the total power changes predicted by the analytical model (see Section 2.1 for the theoretical discussion and Section 2.2 for the calculation results) are verified by FDTD. To do this, the power emitted by a dipole was calculated with and without the fibre geometry and the ratio of these results gave the power change (for comparison with the analytical method).

The electric dipole source was located at the centre of the FDTD domain and the flux was calculated over a centred sphere at each time-step and summed to calculate the total power emitted by the source. The flux was calculated using the expression for the Poynting vector normal to the sphere surface,

$$\mathbf{S} = \int_{\text{Sphere}} (\mathbf{E} \times \mathbf{H}) \cdot \hat{\mathbf{n}} \quad dS, \tag{2.27}$$

where $\hat{\mathbf{n}}$ is the unit normal to the sphere and the integral is over the sphere surface. The FDTD domain was set up with a cylindrical material of refractive index 2.025 (equal to the index of tellurite at the emission wavelength of 700 nm), for the fibre, in air (refractive index of 1). See Fig. 2.19 for a schematic of the system modelled by the FDTD. When calculating the total power at different dipole locations, the location of the cylinder was changed so that the dipole remained centred in the computational domain. This allowed the dipole to remain at the centre of the integration sphere without needing to expand the domain size unnecessarily. For example, when the power of the

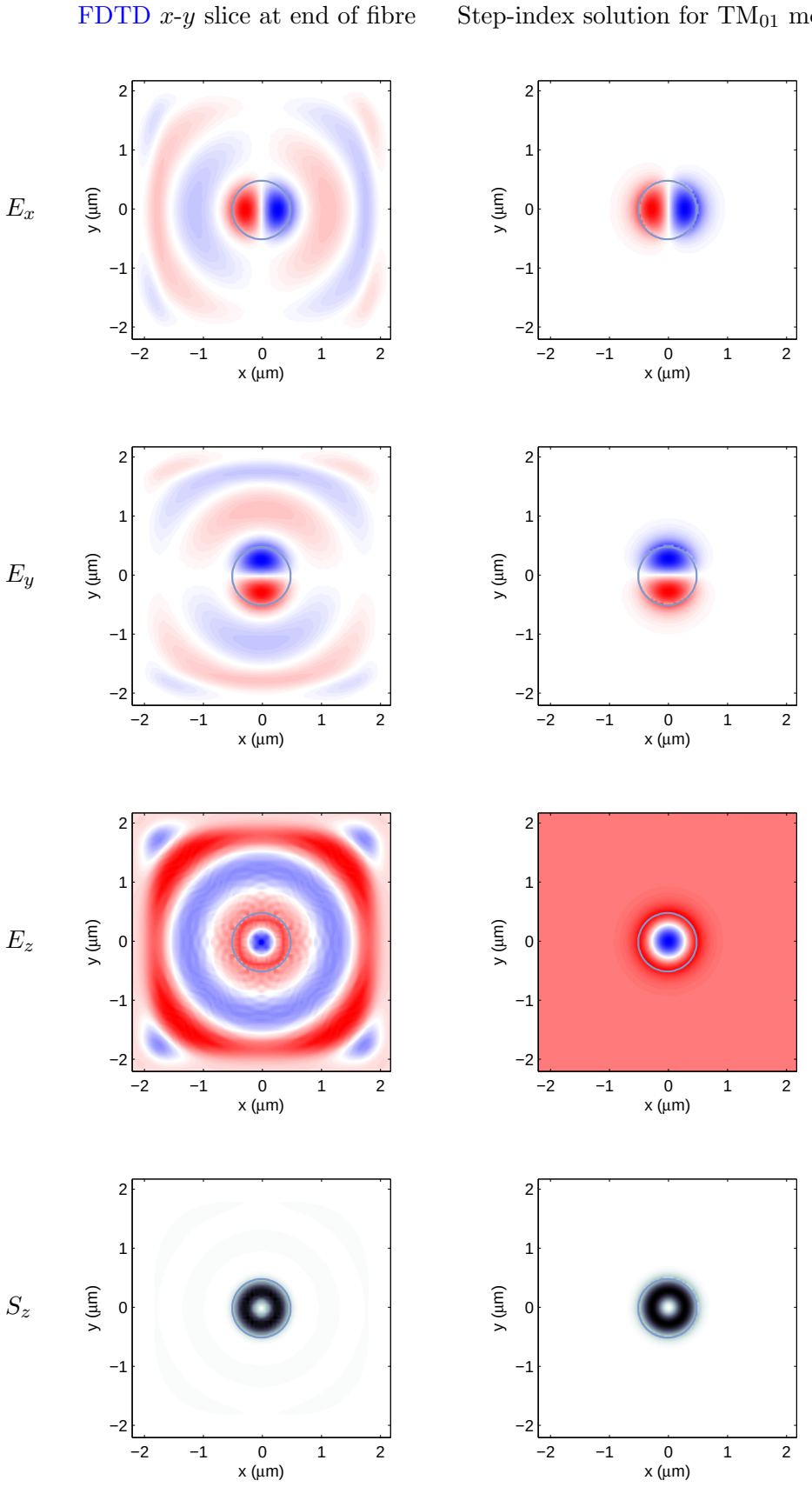

FIGURE 2.18: Comparison of fields and intensity obtained using the FDTD method described in the text and step-index fibre analytical field expressions. Blue and red colours in the vector plots denote positive and negative direction.

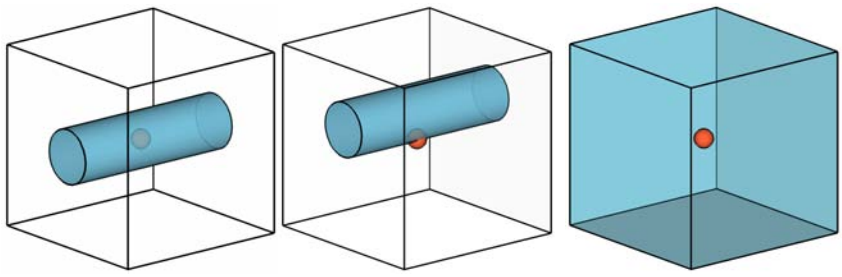

(A) (B) (C)

FIGURE 2.19: Schematics of the FDTD domain for calculating power, showing how the fibre is positioned in order to keep the dipole at the centre of the domain for each calculation. Tellurite glass is shown in blue, air in white, and the dipole as a red sphere. The computational domain is shown as a black cube. Note that the PMLs and integration sphere are not shown for clarity. (a) Dipole at fibre centre. (b) Dipole at fibre interface. (c) Dipole in bulk glass for normalisation of the results.

dipole at the interface was calculated, the fibre was moved in y a distance equal to the core radius (see Fig. 2.19b).

The total domain size was scaled to the size of the integration sphere radius and PML thickness, with the sphere radius depending on the fibre core diameter (it was varied to ensure that the sphere integration was larger than the core).

The flux calculation was started after the system had reached a steady-state. The same simulation was also performed without the fibre cylinder so that a bulk material power value could be determined in order to find the power change. In these bulk simulations the whole domain was filled with a material of refractive index 2.025, such that the power change is relative to the tellurite bulk and so is comparable to that found by the analytical method.

Figure 2.20 shows the results of these simulations. The analytical calculations are shown with the line and the FDTD data are shown as dots, and the results show good agreement. The relative difference in the results, $(P_{\mathrm{FDTD}} - P_{\mathrm{model}})/P_{\mathrm{FDTD}}$, is less than 1%.

For the FDTD results, computational parameters were systematically changed and checked to be sure that the result had converged (e.g. PML thickness, grid resolution, the spacing around the fibre, etc.) and the convergence tests for FDTD grid spacing and PML thickness are shown in Fig. 2.21.

2.3.3 Capture fraction

The capture fraction was calculated using FDTD for comparison with the step-index model (see Section 2.1) predictions. The FDTD domain, shown in Fig. 2.22, consisted

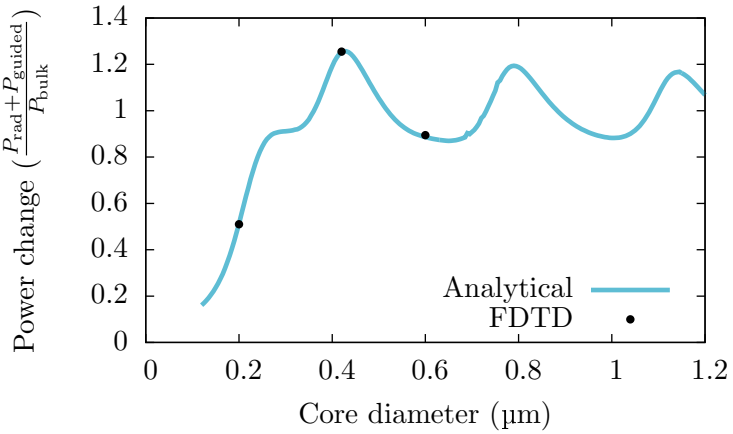

FIGURE 2.20: Comparison of total power emitted by the dipole obtained by FDTD and step-index model. The dipole is located at the centre of the fibre, oriented radially, and is emitting at 700 nm. The line corresponds to the step-index model and dots correspond to FDTD data. FDTD shows good agreement with the analytical results, with a relative difference of $< 1\%$.

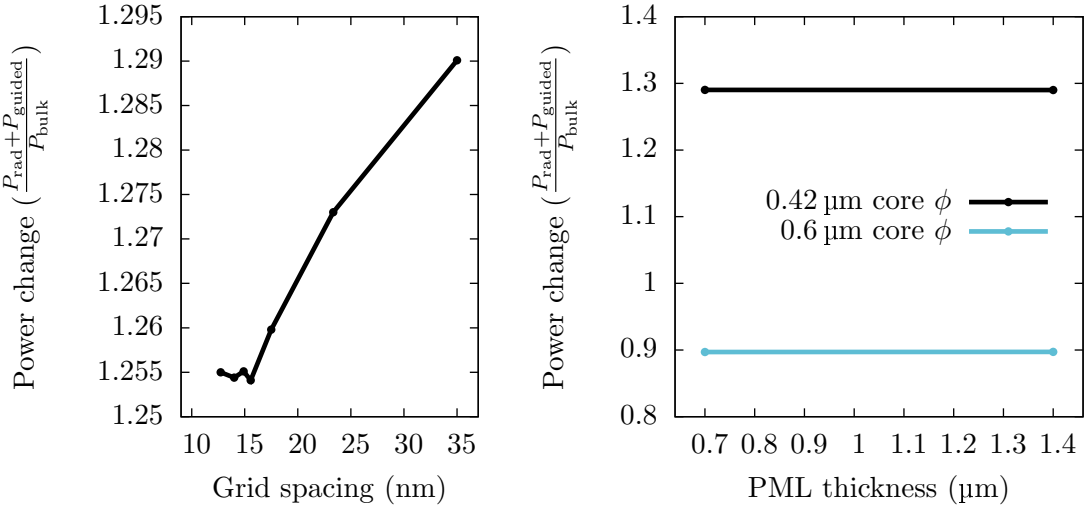

FIGURE 2.21: Convergence tests for FDTD total power calculations, as shown in Fig. 2.20. The dipole is located at the centre of the fibre, oriented radially, and is emitting at 700 nm. The fibre is step-index with a tellurite core and air cladding, and a core diameter of 0.42 µm. Varying (a) grid spacing (PML = 0.7 µm) and (b) PML thickness (grid spacing = 35 nm).

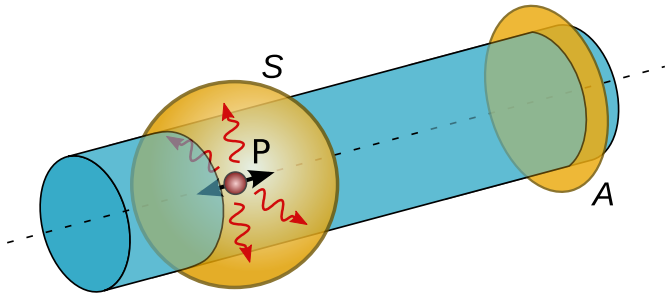

FIGURE 2.22: Flux integration surfaces used in the FDTD calculation of total power and capture fraction.

of a step-index fibre (the cylinder) in air with two flux calculation surfaces (labelled S and A in the figure).

One flux surface, S, is a sphere centred on the dipole source, as for the total power calculations (see Section 2.3.2), and the second, A, is a circular surface that is slightly larger than the fibre diameter. This second surface calculates the flux down the fibre, i.e. the guided power. This surface (A) must be larger than the fibre to capture as much of the evanescent power in the guided mode as possible, but must also be small enough that a minimal amount of the radiation power is included. For the FDTD calculations shown here, the radius of the surface A was 1.5 times larger than the radius of the fibre.

The flux through these two surfaces then provides the quantities needed to calculate the capture fraction, P_{total} and P_{guided}. In this calculation P_{total} is calculated from the flux through the sphere S, which will be denoted P_S, and P_{guided} by the flux through the circular surface A, which will be denoted P_A. Following Equation (2.12), the capture fraction, CF, is then given by

$$CF = \frac{P_A}{P_S} \tag{2.28}$$

As for the selective mode coupling calculations (see Section 2.3.1, and in particular Figs. 2.16 and 2.17), a length of fibre was modelled to separate the radiated power from that guided by the fibre. This greatly increases the amount of memory required for a given fibre core diameter, compared to the total power calculations a much longer computational domain is needed. A fibre length of 49 µm was simulated for the calculations shown here, which was based on the simulation results in Fig. 2.16.

The results of these FDTD calculations are shown in Fig 2.23, comparing the capture fraction obtained by the FDTD method (circles) to the analytical solution using the two expressions for total emitted power - bulk material power (blue) and summing the power in all modes (orange). The FDTD results show a reasonable match to the capture

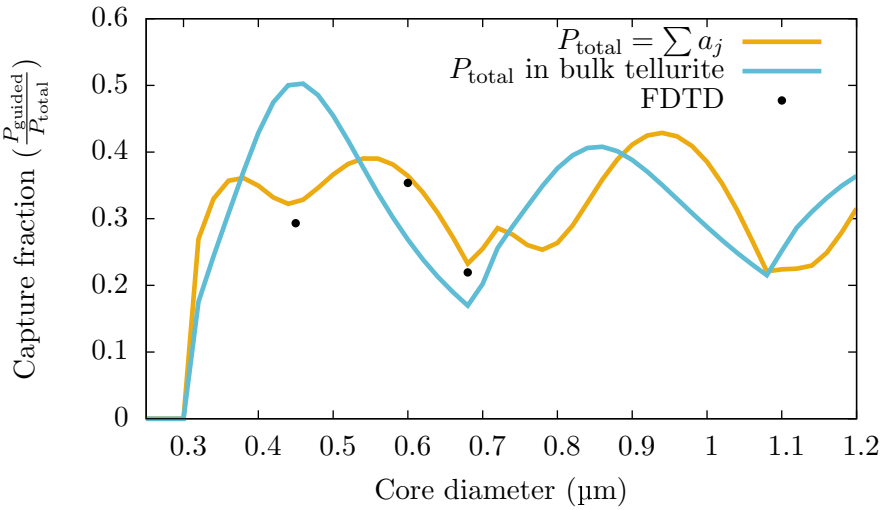

FIGURE 2.23: Comparison between the results of FDTD (circles) and the analytical model (orange line) for capture fraction calculations, with the capture fraction calculated using bulk emitted power shown for comparison (blue line). The step-index fibre simulated had a tellurite core with an air cladding, and the dipole was z-oriented, emitting at 700 nm and located at the centre of the fibre core. For the FDTD simulation, the grid spacing was 25 nm and the fibre length was 49 µm. FDTD shows good agreement with the analytical results, with a relative difference of 3% at 0.6 µm and a maximum difference of 10%.

fraction calculated when using the analytical solution and a total power calculated by summing all modes. The relative difference, $(CF_{\text{FDTD}} - CF_{\text{model}})/CF_{\text{FDTD}}$, is 3% at 0.6 µm, 7% at 0.68 µm and 10% at 0.45 µm. This total power expression also matches to a significantly higher degree than when using bulk power emission, indicating that bulk power does not describe the dipole emission in the vicinity of the optical fibre accurately. The small inconsistency between the FDTD and analytical method, becoming greater at smaller core diameters, can be attributed to the finite radius of the fibre flux surface (A). This surface must be of a limited radius so that the radiation power does not contribute to the calculated fibre flux. At smaller core diameters the fibre mode extends further from the core and so this surface captures less of the fibre power, which lowers the calculated capture fraction compared to that expected if all the guided power is collected. A value of 1.5 times the core radius was used for this surface. This calculation could be extended by varying this surface radius to find the optimal value (i.e. that captures the maximum amount of fibre power, while excluding radiation power).

Convergence of the FDTD results were tested by varying PML thickness and grid resolution, and the convergence data are shown in Fig. 2.24.

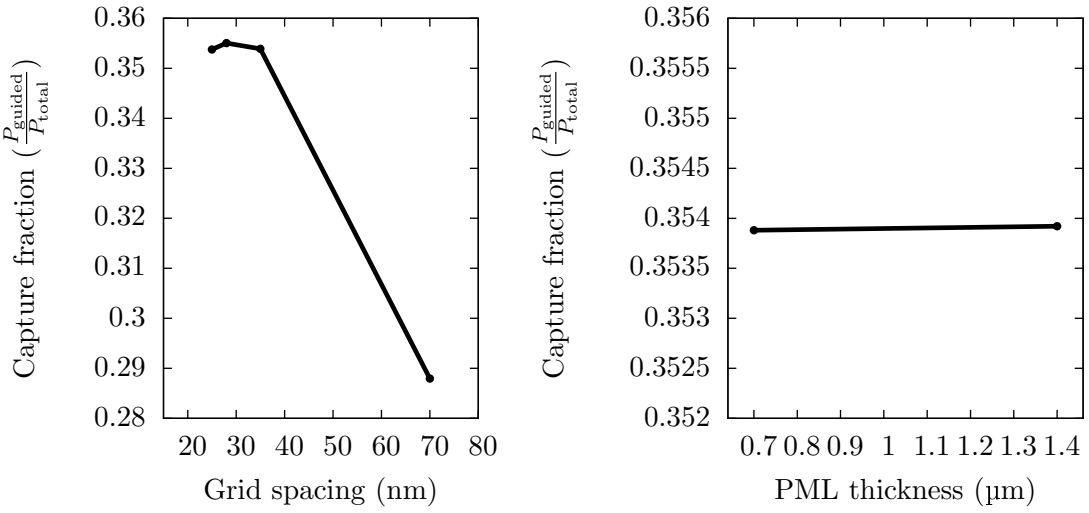

FIGURE 2.24: Convergence tests for FDTD capture fraction calculations, as shown in Fig. 2.23. The dipole is located at the centre of the fibre, oriented longitudinally (z-oriented), and is emitting at 700 nm. The fibre is step-index with a tellurite core and air cladding, and a core diameter of 0.6 µm. Varying (a) grid spacing (PML = 0.7 µm) and (b) PML thickness (grid spacing = 35 nm).

2.3.4 Whispering gallery modes

The total emitted power and field patterns for the WGM calculations (see Section 2.2.3.1) were verified using FDTD. The total power was calculated as in Section 2.3.2, and the field pattern was found by outputting the field at a slice through the fibre cross-section at the position of the dipole (i.e. an r-θ slice at $z = 0$).

Figure 2.25 shows a comparison of the results obtained via FDTD and the analytical method for the total power, at core diameters corresponding to both on- and off-resonance. These results were obtained with a z-oriented dipole at the core-cladding interface of the fibre. The results agree well, and are assumed to be indicative of the behaviour everywhere.

The output fields from the FDTD method also compare well with that calculated using the analytical method. This is shown in Fig. 2.26, where E_z is plotted for an r-θ cross-section of a fibre at the dipole position. This is compared to the analytical solution for S_z, for the same 0.8 µm core diameter. Note that both field patterns show a 10-node WGM pattern.

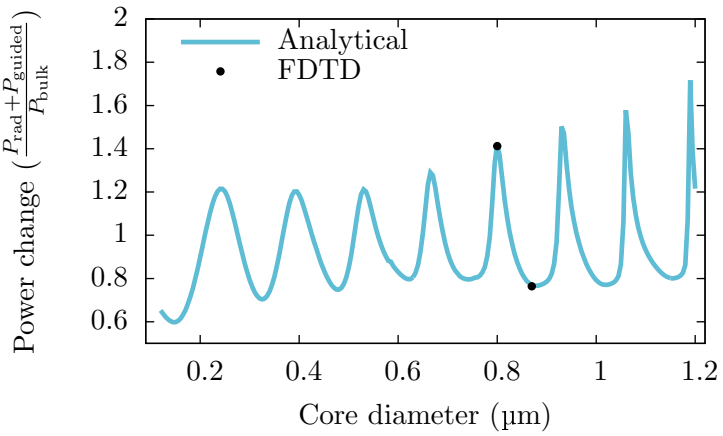

FIGURE 2.25: Comparison of total power calculated via FDTD and the analytical method, for a z-oriented dipole positioned at the core-cladding interface of a step-index fibre consisting of a tellurite core with an air cladding. Dipole emission is at 700 nm.

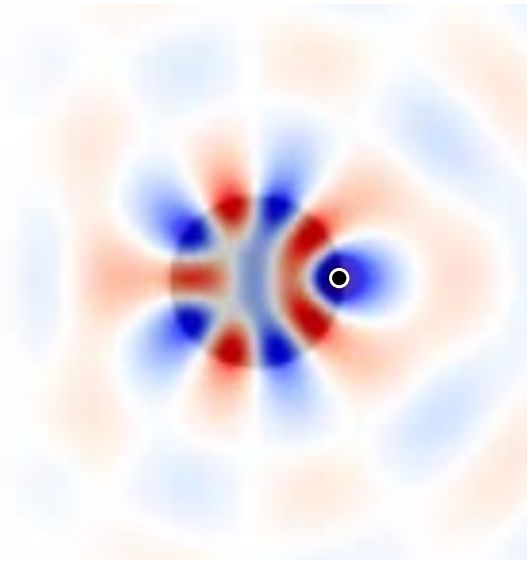

(A) E_z field via FDTD. Blue and red corresponds to positive and negative values for the electric field, with white indicating no field. The core region is overlaid as a darker circle.

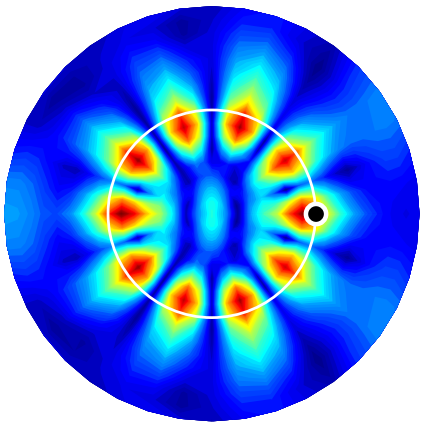

(B) S_z field via analytical method. The core is overlaid as a white circle.

FIGURE 2.26: Comparison of fields calculated by (a) FDTD and (b) the analytical step-index method, for a z-oriented dipole at the core-cladding interface. The dipole is emitting at 700 nm and the location is shown as a small black circle. The step-index fibre has a tellurite core with an air cladding, and a core diameter of 0.8 µm.

2.4 Conclusion

Modelling of emitters in the vicinity of a waveguiding structure is relevant for many applications of nanoparticle-embedded material. Specifically, for the case of ND, it is important to understand the coupling of emission from the nanocrystal to the optical fibre modes. This chapter has shown the derivation of a model to describe this emitter-fibre interaction, by using a step-index fibre and a dipole approximation to find the coupling of emitted power into the fibre modes. The Purcell effect, caused by a change in the local density of states due to the fibre core-cladding interface, was accounted for by finding the radiation modes of the fibre and including these when calculating emitted power.

A high refractive index contrast was shown to be essential for good coupling between the fibre modes and the emitter. A coupling efficiency of up to 81% was shown for a tellurite core step-index fibre surrounded by an air cladding. The capture fraction was calculated for a large range of core diameters and dipole positions, and the model could be used to calculate the expected coupling for any dipole orientation and position. These results can be used to understand NV coupling to the optical fibre modes for single photon emission or single NV magnetometry.

An initial derivation, expanding the theory to multiple emitters, was also demonstrated. This could be expanded for applications involving multiple-NV magnetometry, 2D dipoles, or single particle detection.

The results of this new model were validated by comparing against FDTD calculations, an independent method, and these comparisons showed good agreement, with total power calculations matching to within 1%.

The model shown here was used to predict coupling of emission into fibre modes and these results drove the design of the fabricated fibres (see Chapters 3 and 4).

3

Glass Fabrication and Optical Characterisation

Here a new hybrid material is developed, embedding diamond nanocrystals containing NV centres into a glass. A soft glass, tellurite, was used, for reasons which will be discussed below. This material shows the advantages of the NV colour centre, such as single photon emission and magnetometry, while allowing the use of the mature fabrication techniques available to soft glasses. In particular, we have fabricated a microstructured optical fibre from this material, and have verified that the diamond colour centres retain single emission properties. This allows the production of hundreds of metres of fibre from a single glass billet, potentially fabricating many hundreds of devices.

This hybrid material process creates several new challenges, however. Diamond begins to graphitise (sp^3 carbon converts to sp^2) at temperatures above ~500–600 °C in the presence of oxygen [79, 80, 81, 82, 83] and this needs to be taken into account during glass melting and fibre drawing conditions (i.e. either a low temperature or an oxygen-free environment is required). Conventional silica and silicate optical glasses are typically melted at temperatures much higher than this; tellurite soft glass was chosen because of both a low melting temperature and a proven optical fibre fabrication process [1]. Secondly, the nanocrystal placement is inherently random, in contrast to methods such as nanopositioning (although selectively doping specific fibre components can help to limit this).

This chapter focuses on the general glass-making procedures, and descriptions and characterisation of the individual samples that were fabricated during this project. An introduction to the basics of fibre fabrication, in the way of fabrication of unstructured fibres, will also be given. Unstructured fibres are often fabricated to characterise the glass; in this case to check that the process doesn't damage the ND or introduce other unwanted

effects, but also to test more general glass properties, such as loss characteristics, where it is important to know the effect of the fabrication, and in some cases (such as loss) the fibre length is advantageous for the measurement. Fabrication of more complex fibres will be discussed in Chapter 4.

The aim here is to provide a context for, and explain, the decisions made during the fabrication process based on the characterisation data and show the evolution of the samples — from the first trial glasses shown here to the fabricated structured fibres of Chapter 4. Characterisation methods will be presented, and include such methods as confocal microscopy (see Section 3.3.1), Hanbury Brown and Twiss auto-correlation (see Section 3.3.2) and Raman spectroscopy (see Section 3.3.3 for Raman features of relevant materials). The results of these measurements will then be discussed in the individual sample descriptions.

3.1 Summary of samples

Summaries of the glass samples are shown in tables 3.1, and unstructed and structured fibres are shown in tables 3.2 and 3.3, respectively. These tables include details of the fabrication and the sample identification names used throughout the remainder of the text. The sample numbers are consistent throughout, such that glass sample G1 was used to fabricate preform P1 and then fibre F1. Where the same glass sample and preform was used to make multiple fibres, the fibres have been denoted F1a, F1b, etc. (where the glass and preform are G1 and P1, respectively). The corresponding in-house sample codes are shown in Section C.1.

Sample	Diamond type added	ND mass added (mg)	ND Conc^{n} (ppm wt.)	Batch mass (g)	Melt conditions	Notes
G1	Abrasive powder	16	320	50	Open air	
G2	Non-irradiated	28	280	100	Glovebox	
G3	Non-irradiated	0.94	9.4	100	Glovebox	
G4	Non-irradiated	0.0048	0.048	100	Open air	Used 0.511 09 g of G3.
G5	Irradiated	0.8	8	100	Glovebox	
G6	Non-irradiated	1	3.3	300	Glovebox, Open Air	Remelted doped tellurite in open air furnace. Glovebox furnace too small for 300 g melt.

TABLE 3.1: Summary of details for glasses fabricated within this project. Section 3.2.1 describes the different diamond types.

Sample	ND Conc^n (ppm wt.)	Structure	Notes
F2	280	Unstructured	
F3	9.4	Unstructured	Failed fibre draw
F4	0.048	Unstructured	No single-photon emission seen
F5	8	Unstructured	

TABLE 3.2: Summary of fabricated fibres in Chapter 3.

Sample	ND Conc^n (ppm wt.)	Structure	Notes
F6a	3.3	Wagon-wheel	
F6b	3.3	Lidded wagon-wheel	Extruded tube
F6c	3.3	Lidded wagon-wheel	Cut tube

TABLE 3.3: Summary of fabricated fibres in Chapter 4.

3.2 General fabrication information

3.2.1 Diamond nanocrystals

The different nanodiamonds used for this project will be referred to as:

'Abrasive powder': Element6 Micron+ MDA 100,000 SLS diamond polishing powder, 100,000 grit from Shell-lap Supplies, Adelaide, Australia.

'Non-irradiated': NaBond nanodiamond manufactured by a non-detonation process, with a purity $> 99.95\%$ (Grade A) and an average particle size of 40-50 nm.

'Irradiated': Diamond nanopowder from Van Moppes, Switzerland. Irradiated with 2 MeV electrons at a dose of 10^{18} cm^{-2}. Annealed under vacuum at 800 °C for 2 h to mobilise the vacancies to the intrinsic nitrogen, and then in air at 475 °C for 2 h to remove the outer graphitic layer caused by the manufacturing process and the irradiation.

3.2.2 Tellurite glass

Tellurite is a member of a group of glasses known as 'soft glasses' and has a relatively low melting temperature, compared to silica (the most widely used material for optical fibres). The glass network former is tellurium dioxide. In this project a lanthanum-doped tellurite glass was used [1], with a composition of $2.2La_2O_3$–$4.9Na_2O$–$19.6ZnO$–$73.3TeO_2$

(mol%). This composition was used because it is an established glass for MOF fabrication at the Institute for Photonics & Advanced Sensing (IPAS). The refractive index of this glass is 2.025 at 700 nm, which is high compared to silica (refractive index of 1.46 [84] at 700 nm). Tellurite also shows high nonlinearity, with $n_2 \sim 5 \times 10^{-19}\,\mathrm{m^2\,W^{-1}}$ [85]. The glass transition temperature, T_g, is at 315 °C, and the difference between glass transition and crystallisation temperature, an indication the crystallisation stability, is $\Delta T = T_\mathrm{x} - T_{rmg} = 165\,^\circ\mathrm{C}$ [1]. The low softening temperature is convenient for fabrication of microstructured fibres using an extrusion technique.

Tellurite glass was chosen as the most suitable host glass for incorporation of nanodiamond due to:

- a low melting temperature, such that the glass is fluid enough to allow ND dispersion (by swirling and convection) and casting (to form a billet for preform fabrication) at 700 °C. Diamond begins to graphitise in an oxygen-containing atmosphere, with oxygen acting as a catalyst, above 450–600 °C (depending on composition — e.g. nanodiamond [79, 80, 81], bulk slab [79, 80, 82], CVD [82, 83]). The glass melting temperature must be kept as low as possible for the ND added to survive the glass melting procedure. Any processing near or above the graphitisation temperature will begin to destroy the diamond, and so for the fabrication presented here the time where the diamond was exposed to the relatively high tellurite melt temperature was minimised.
- a high refractive index. From the modelling (see Section 2.2.2), it was seen that the refractive index contrast was important for high capture efficiency. Tellurite has a relatively high refractive index of 2.025 at 700 nm [1].
- suitable optical transmission at the emission wavelength range of the NV centre. Tellurite has a wide transparency window, from 500 nm to 4 µm, and a low transmission loss of $<1\,\mathrm{dB\,m^{-1}}$ from 550–900 nm [1].
- previous experience for fibre fabrication. Tellurite fibre fabrication has already been shown [1, 86] and the equipment and expertise was available for the fabrication of the billet, preform extrusion (see Section 3.2.4) and fibre drawing.

Another glass family, fluoride glass (whereas tellurite is an oxide glass), was also tried, as it shows the same properties as listed for tellurite above (apart from a lower refractive index of ∼1.5). The fluoride glass was found to be unsuitable, however, as the nanodiamond did not disperse in the glass melt, instead floating on the surface.

3.2.3 Glass fabrication

Glass fabrication is the first step in creating an optical fibre and I will now present the general method used to create the glass samples for this project. Any variations from this method are noted in the individual sample descriptions (see later in this chapter and Chapter 4).

The tellurite raw materials were batched as for a standard, undoped tellurite glass melt. The raw materials were placed into a gold crucible and melted for 1 hour in a controlled atmosphere furnace (N_2 + O_2) at 850 °C or an open air furnace at 900 °C. The crucible containing the glass melt was generally removed from the open air furnace and swirled once or twice during this time.

The furnace temperature was then reduced to 700 °C. As soon as the furnace reached 700 °C the crucible was removed and the dry ND powder was added. The crucible was swirled to distribute the particles throughout the melt and then returned to the furnace at 700 °C for 15 min. This additional time in the furnace was to assist in homogeneously distributing the ND.

The crucible was then removed, swirled again and cast into a brass mold. This cast billet was then annealed at 315 °C for 1 h.

Three different types of glass sample were fabricated; 50 g rectangular blocks with dimensions 15x10x30 mm used to measure bulk glass properties, 100 g cylindrical billets with a diameter of 30 mm and height of ∼20 mm for fabrication of unstructured fibres (see Section 3.2.4), and 300 g cylindrical billets with a diameter of 50 mm and height of ∼30 mm for fabrication of structured fibres (see Section 4.1).

Glass fabrication

1. Batch raw materials and put into gold crucible
2. Put crucible into furnace at 700 °C
3. Increase furnace temperature to 900 °C
4. (Open air) Leave at 900 °C for 1 h, removing to swirl every ~20 min
   (Glovebox) Remove from furnace and swirl, decrease furnace temperature to 850 °C and leave for 1 h
5. Decrease furnace temperature to 700 °C
6. When furnace has reached this temperature, remove the crucible, add ND, swirl, and return to furnace at 700 °C
7. Leave in furnace for 15 min
8. Remove crucible from furnace, swirl, and cast into brass mold heated to ~305 °C (open air) or ~295 °C (glovebox)
9. Anneal glass in mold at 315 °C for 1 h

3.2.4 Unstructured fibre fabrication

Before fabricating more complex structures, the initial glass trials were formed into unstructured fibres for characterisation and validation of the basic preform and fibre fabrication processes. These unstructured fibres are effectively thin glass rods, generally with an outer diameter of 160 µm to be consistent with the diameter commonly used for the more complex fibres (see Chapter 4).

The glass billet (see Section 3.2.3) is processed in two main steps to fabricate the final fibre: an initial shaping in an extrusion process [43] to create what is called the preform (see below), and the drawing down of this preform to the dimensions of a fibre using a fibre draw tower.

Preforms are the intermediate step between the glass billet and the final drawn fibre. This is the stage at which the structure needed for the fibre is created, and the end result of the draw is a scaled version of this preform cross-section.

FIGURE 3.1: (Left) Die design used to fabricate a rod preform. (Right) Die shown with the sleeve that holds the cylindrical glass billet and the plate to which the ram applies force.

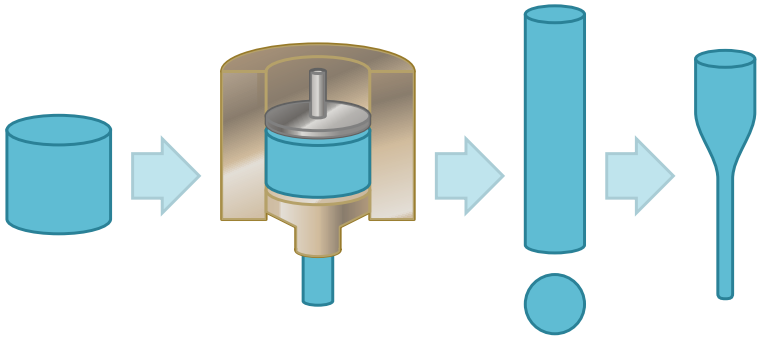

FIGURE 3.2: Bare fibre fabrication schematic.

To create the complex structuring of the later MOFs an extrusion process was used to fabricate the preform. This same process is used to create the unstructured fibre so that the results can be applied to the MOF fabrication. The billet was heated inside a 10 tonne electric ram to a temperature at which the glass was soft enough to be pushed through a die. This die was designed to create the required preform shape — for example, the die used to fabricate the rod preform is shown in Fig. 3.1. The ram head moved at a constant speed so that it fed the die with a constant glass flow.

For a 30 mm diameter billet, as used for a 10 mm rod preform (a cylindrical rod of glass produced by a circular die design, used to create the unstructured fibres), the ram feed rate was $0.2\,\mathrm{mm\,min^{-1}}$. After this extrusion process the preform is annealed to remove any introduced internal stresses. Preforms were then mounted into a fibre draw tower and drawn down into optical fibres.

The complete process for unstructured fibre fabrication is shown below for reference, and a schematic diagram of the process can be seen in Fig. 3.2. All annealing steps were performed using the same general annealing protocol (see Section C.2).:

Unstructured fibre fabrication

1. Fabricate glass billet (see Section 3.2.3).
    - Anneal billet.
2. Extrude billet to create preform.
    - Anneal preform.
3. Draw fibre in fibre draw tower.

3.3 Characterisation methods

3.3.1 Confocal microscopy

A confocal microscope was used to image NV centres in the samples. Figure 3.3 shows a schematic of the setup. A 532 nm pump laser, focused through a 100X objective to a spot size of ~300 nm, was scanned across the sample using a piezo stage. The resulting PL from this pump was collected back through the same 100X lens and into a multi-mode collection fibre which also acted as the confocal pinhole. The emission signal was detected by single-photon sensitive avalanche photodiodes (APDs). A dichroic mirror was used to separate the pump beam from the return signal, and the collected emission is filtered with a 550 nm high-pass to filter the pump and, depending on what is to be imaged, a 650–750 nm bandpass filter to select the NV^- emission range. The confocal scans were performed at room temperature.

The fibre scans in this chapter were all performed by scanning across the fibre endface (Fig. 3.3b shows a diagram of the scan axes and laser incidence). In Chapter 4, some scans are taken with different laser and scanning orientations, and these will be described in the text and using similar diagrams to those shown in Fig. 3.3b.

Bulk glass samples were polished and then mounted and scanned along the surface, while unstructured fibres were generally cleaved and scanned across the fibre endface. The confocal microscope focal point was below the surface of the sample in all scans to ensure that only embedded NV centres were characterised.

The signal could be routed to an optical fibre splitter for measuring photon statistics (see Section 3.3.2 below) or a high sensitivity spectrometer for PL measurements.

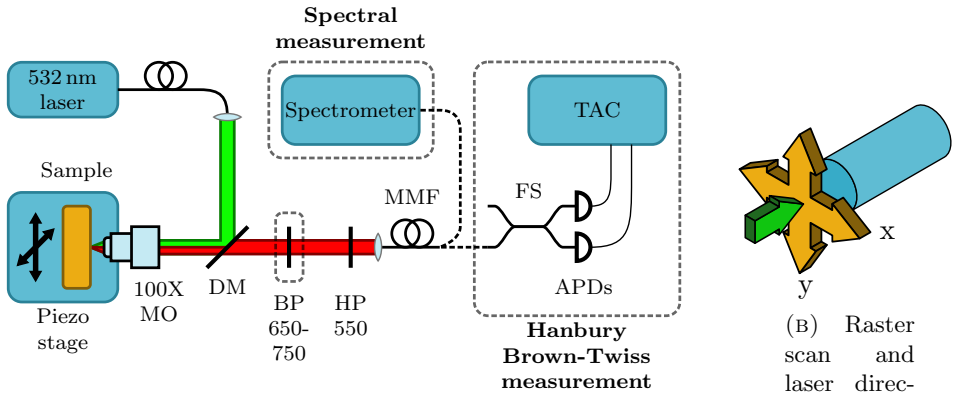

(A) Confocal schematic

(B) Raster scan and laser direction

FIGURE 3.3: (a) Schematic of the confocal microscope. MO — microscope objective, DM — dichroic mirror, BP — bandpass filter, HP — high-pass filter, MMF — multimode fibre, FS — 50/50 fibre splitter, APDs — avalanche photodiodes, TAC — time-to-amplitude converter. (b) Schematic showing the raster scan direction (orange) and pump laser incidence (green) relative to the fibre geometry (blue).

3.3.2 Photon statistics measurement

A Hanbury Brown-Twiss (HBT) [87] interferometer was used to measure the photon statistics of the emitted light. This measures the second-order intensity correlation function,

$$g^{(2)}(\tau) = \frac{\langle I(t)I(t-\tau)\rangle}{\langle I(t)^2\rangle}. \tag{3.1}$$

A schematic of this measurement is shown in Fig. 3.3. The sample beam is incident on a beamsplitter, in this case a fibre splitter (FS), and directed to two photodetectors (APDs). A time-to-amplitude converter (TAC) measures the time delay between a photon count on each of the detectors and this data is binned and plotted. This data is normalised to calculate $g^{(2)}$. For a Poissonian source, such as a laser, this function is 1 for all times. However, a single photon source cannot output two photons at the same time (by definition) and so the probability of the two detectors firing at the same time should be reduced, reaching zero for perfect detectors and no background signal. This is seen in the correlation function as a dip in the data at zero time delay when the incident light shows sub-Poissonian properties.

If photons from more than one emitter are incident, the dip at zero time degrades. The single-photon dip at zero time for an ideal N photon emitter is [18] $1 - 1/N$. It follows from this equation that (taking $N = 2$) a $g^{(2)}(0)$ value below 0.5 indicates a single photon emitter.

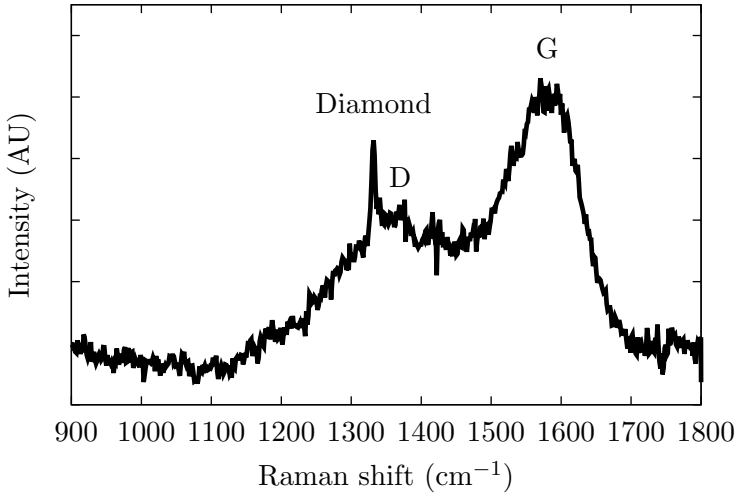

FIGURE 3.4: Raman spectrum of non-irradiated ND, taken at liquid nitrogen temperature (80 K) with an excitation wavelength of 514.5 nm. The diamond and graphite (D and G) peaks have been labelled.

3.3.3 Raman properties of nanodiamond

Raman spectroscopy was performed on the samples to detect diamond, and any graphite or other amorphous carbon either present on the diamond or formed during the fabrication. This section will summarise the Raman properties of the relevant materials, but will not present a complete description of the Raman spectroscopy technique itself (please see e.g. Ref. [88] for a more complete overview).

Diamond can be distinguished from other forms of carbon by the Raman spectrum. Single crystal diamond has a narrow peak at 1332 cm^{-1} with a width of 2 cm^{-1} [89], which can be shifted and broadened slightly in different forms (for example, films can shift to 1332–1336 cm^{-1} and 5–17 cm^{-1} linewidth [89]). Graphite, on the other hand, exhibits broad peaks at 1350 cm^{-1} and 1560 cm^{-1} [80] labelled D and G peaks, respectively. The Raman cross-section of graphite is also ∼55 times higher than that of diamond [90] and so small quantities of graphite (compared to the quantity of diamond) will dominate the spectrum. Figure 3.4 shows the Raman spectrum of non-irradiated ND powder, taken at 80 K with an excitation wavelength of 514.5 nm.

Tellurite glass shows Raman features below 1000 cm^{-1} and involves several broad peaks, the strength of which depends on glass composition [85]. The main interest for this project is that the glass spectrum does not overlap with that of the diamond and graphite peaks.

FIGURE 3.5: Sample slice of glass G1. The glass is dark due to a high concentration of added diamond (compare to e.g. G3 in Section 3.4.3). The dark swirls suggest an inhomogeneous mixing. (Right) Same image labelled with an area characteristic of a 'dark' patch and away from these patches.

3.3.4 Scanning electron microscopy

Fibre structural characterisation was performed using scanning electron microscopy (SEM). Fibres were cleaved and mounted into a fibre SEM mount vertically. These samples were platinum coated (2 nm thickness).

3.4 Initial glass trials

3.4.1 G1 diamond polishing powder-doped block

This glass was the first trial of incorporating ND into glass. Diamond polishing powder was used as an inexpensive test material to verify the glass fabrication method before using the nanoparticle diamond powder supplied by the University of Melbourne. NV centres, and nitrogen impurities in general, are naturally occuring in diamond and so the diamond polishing powder was expected to contain these colour centres.

16 mg of diamond polishing powder was added to the tellurite melt. The furnace used for this glass sample was an open-air furnace, and the glass melting followed the fabrication steps as outlined in section 3.2.3.

A slice of the glass block is shown in Fig. 3.5. The block was quite dark and, as expected from the appearance, had a high loss (see Section 3.4.1.1 below), which was most likely due to the large diamond mass added (compare this sample to the lower concentration glass G3 in Section 3.4.3). While this high loss was not desirable, the diamond survivability and anti-bunching behaviour after the high melting temperatures

were the important parameters in this first trial. The sample also appeared to be inhomogeneously mixed, as seen by the pronounced dark swirled areas.

3.4.1.1 G1: Loss measurement

Measurements using ultraviolet-visible spectroscopy (UV-Vis) were performed on a slice of sample G1. The loss data versus wavelength is shown in Fig. 3.6a. The loss is calculated from the transmission (see Section C.4) and includes subtraction of Fresnel reflections (see Section C.3) before normalising to the sample thickness of 1.08 ± 0.01 mm. There appear to be two components to the loss spectrum; a high background loss of $\sim$2000 dB m^{-1}, and a wavelength-dependent loss that increases with decreasing wavelength.

To explore this wavelength dependence, the loss versus inverse wavelength to the 4$^{\text{th}}$ power (λ^{-4}) was also calculated and is shown in Fig. 3.6b. A fit to λ^{-4} for loss suggests Rayleigh scattering [91], an indication that the scattering particles are much smaller than the scattered wavelength. The least-squares linear fit line is shown for the loss in Fig 3.6b.

3.4.1.2 G1: Raman spectroscopy

Raman spectroscopy on a piece of the glass block confirmed the presence of diamond. The spectrum (Figs. 3.7a and 3.7b) shows a peak at 1332 cm^{-1}, which is consistent with diamond. Graphite peaks are not seen in the spectra, suggesting that no graphite was present in the sample volumes measured as the Raman cross-section is much larger than that of diamond (see Section 3.3.3 and Fig. 3.4 for more information on diamond and graphite Raman spectra). Raman characterisation of a later sample, preform P2, confirmed that graphite present in the initial diamond powder was not seen on the resulting glass Raman spectrum and this was attributed to preferential oxidation of the graphite (see Section 3.4.2.3 for a more detailed discussion). The spectrum also shows the same spectral features both at and away from the dark patches (see Fig. 3.5), which indicates that these patches are not due to graphite (either from the initial diamond powder or from graphitisation at the elevated temperatures of the melt).

3.4.1.3 G1: Confocal microscopy

Confocal microscopy imaging (see section 3.3.1) confirmed the presence of diamond colour centres after the glass fabrication process. Figure 3.8 shows the confocal scan

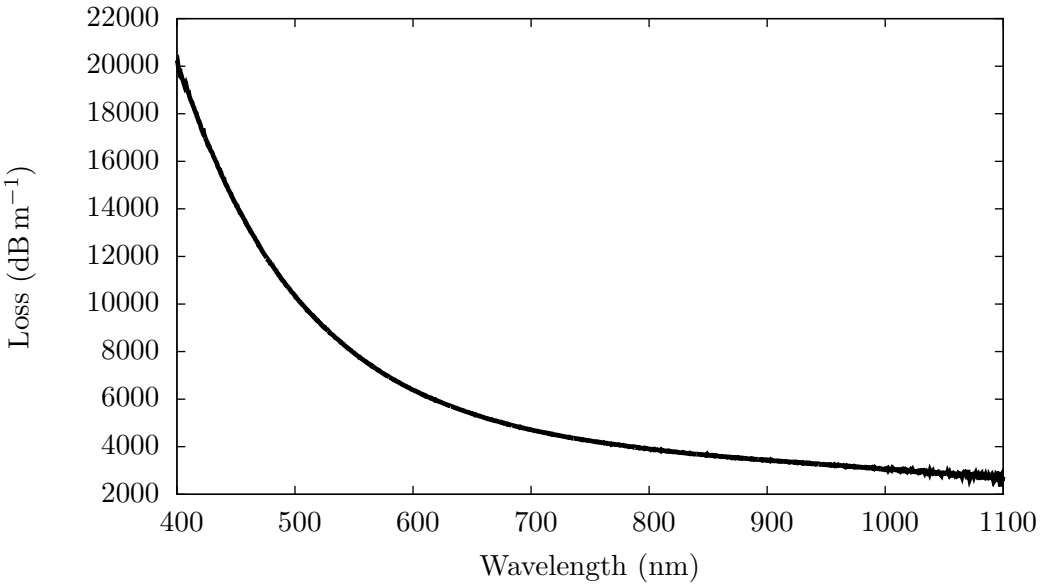

(A)

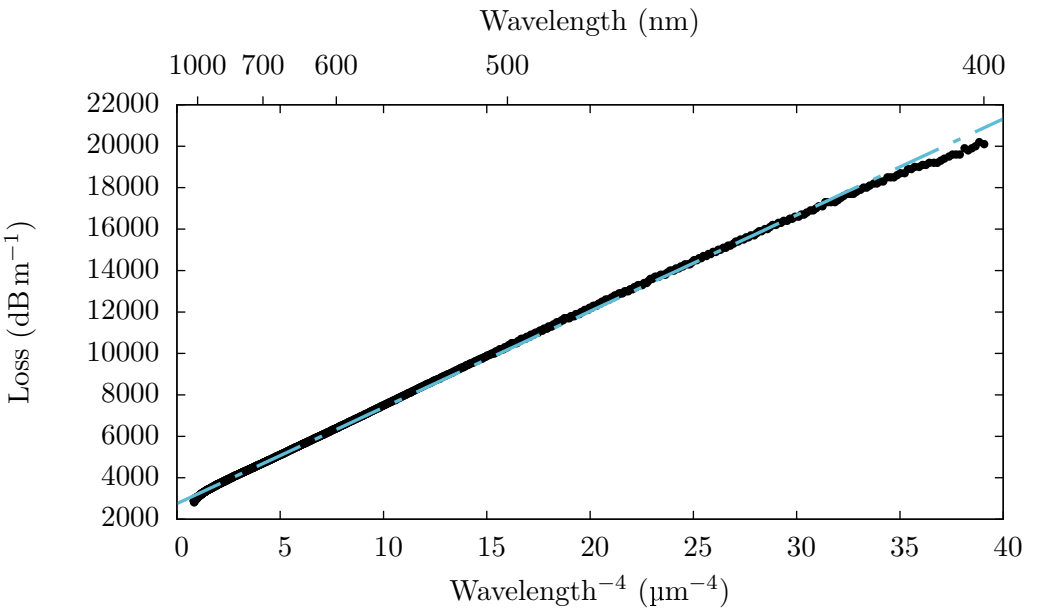

(B)

FIGURE 3.6: (a) Plot of Loss vs. wavelength for sample G1 measured using UV-Vis. (b) Plot of Loss vs. wavelength^{-4} for sample G1 and the corresponding linear fit. A linear relation indicates scattering in the Rayleigh regime [91], i.e. particles with radii much less than the wavelength. Loss due to Fresnel reflection has been subtracted from both spectra (see Section C.3).

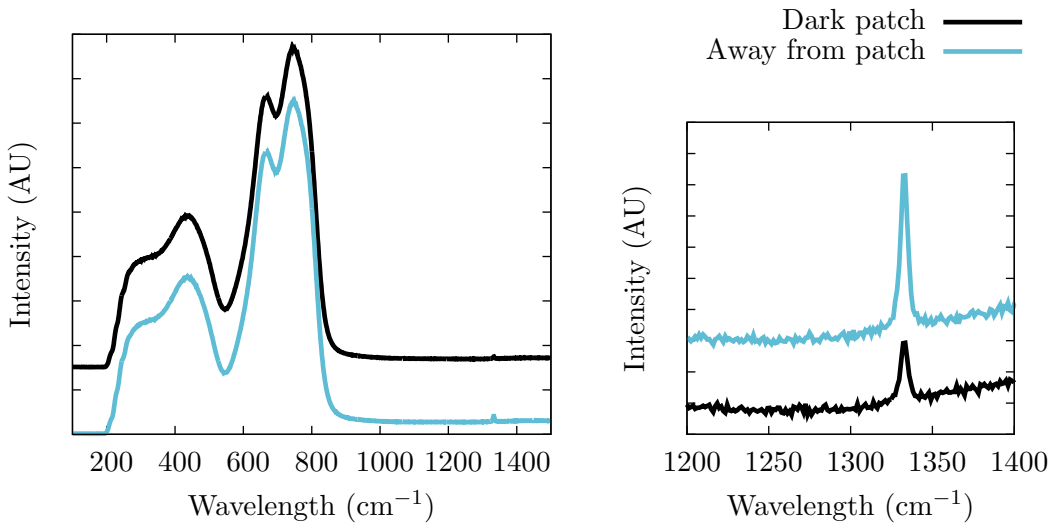

(A) Full (B) Zoom

FIGURE 3.7: Raman spectrum of sample G1 in dark patches and away from dark patches (see Fig. 3.5) for 488 nm excitation wavelength. The peak at 1332 cm^{-1} is indicative of diamond, and the peaks below 1000 cm^{-1} are consistent with tellurite [85].

image obtained. The signal in this scan has been filtered to the emission of the NV centre with a 650–750 nm bandpass filter, and so the PL visible should be due to diamond NV centres. Many large particles (>1 µm) appear in the scan as the sample was fabricated using diamond abrasive powder, rather than ND.

Anti-bunching was seen in the NV emission (see Section 3.3.2). Figure 3.9 shows the $g^{(2)}$ data obtained for the NV centre pictured, and a comparison of the spectrum obtained from this centre compared to the background glass PL is shown in Fig. 3.10. These spectra were taken from the confocal output without the 650–750 nm bandpass filter, so that any glass background signal features outside of this window could be collected. Notice that the background glass signal only begins to show features beyond 700 nm, and is distinguishable from that of the NV PL at 650–750 nm. Note also that the glass does show PL in the 650–750 nm collection window, and this will contribute some background signal to the confocal scans and anti-bunching measurements. This background spectrum agrees well with that measured for undoped tellurite using 532 nm excitation [92]. Although the anti-bunching dip at $t = 0$ does not extend below 0.5, to confirm *single*-photon emission, it does show non-classical (anti-bunching) behaviour. This smaller dip may be due to the presence of a few emitters or a high background signal. See section 3.3.2 for more details.

The importance here is that NV centres were present in the diamond after the glass processing (i.e. the colour centres survived the high temperatures and the glass environment) and non-classical statistics were seen, which verifies that the glass fabrication

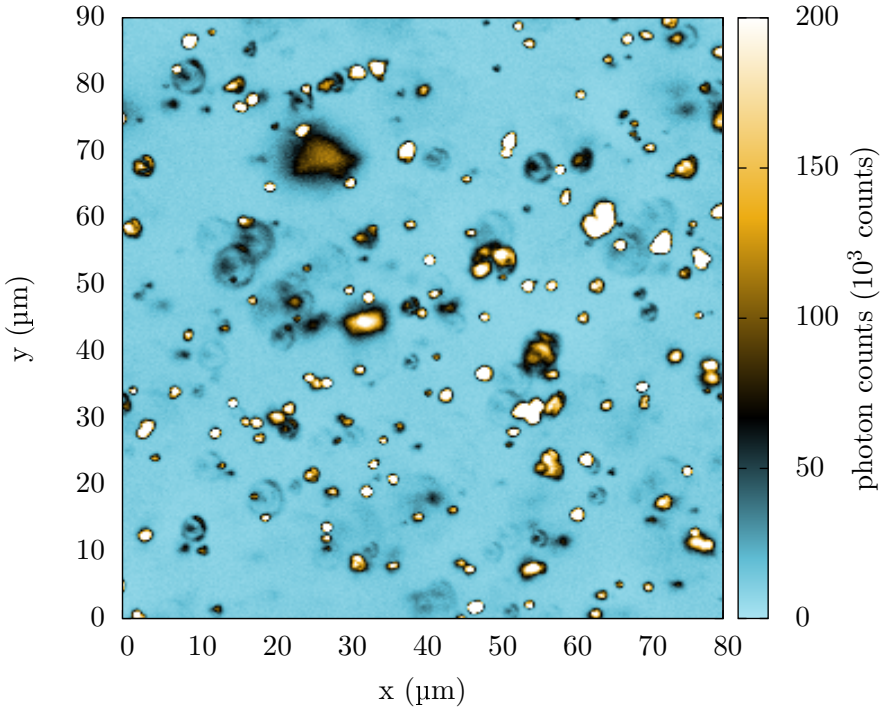

FIGURE 3.8: Confocal image of sample G1 at a pump wavelength of 532 nm showing fluorescence from diamond colour centres. Included diamond is abrasive powder and so the average particle size is quite large compared to the nanoparticle diamond.

process was useable for the creation of the hybrid diamond-glass material. Successive trials would be using ND with a controlled size, optimised for the probability of single emitters, and so the characterisation of strictly single emitters in this trial was not essential.

3.4.2 G2 non-irradiated nanodiamond-doped

The measurements of the initial trial, using diamond abrasive powder (see Section 3.4.1), confirmed that the NV centres in the diamond survived the glass processing. Sample G2 was then fabricated using nanodiamond powder (non-irradiated ND). A 100 g, 30 mm diameter cylindrical billet was made so that a fibre could be fabricated from the sample. This sample would be used to investigate whether the non-irradiated ND powder would survive the glass processing and the subsequent fibre processing steps of extrusion and drawing (see Section 4.1). See below for details on the resulting preform (P2) and fibre (F2).

The glass sample was fabricated using 28 mg of non-irradiated ND powder added to a 100 g tellurite melt, as described in the general glass fabrication (see Section 3.2.3). This

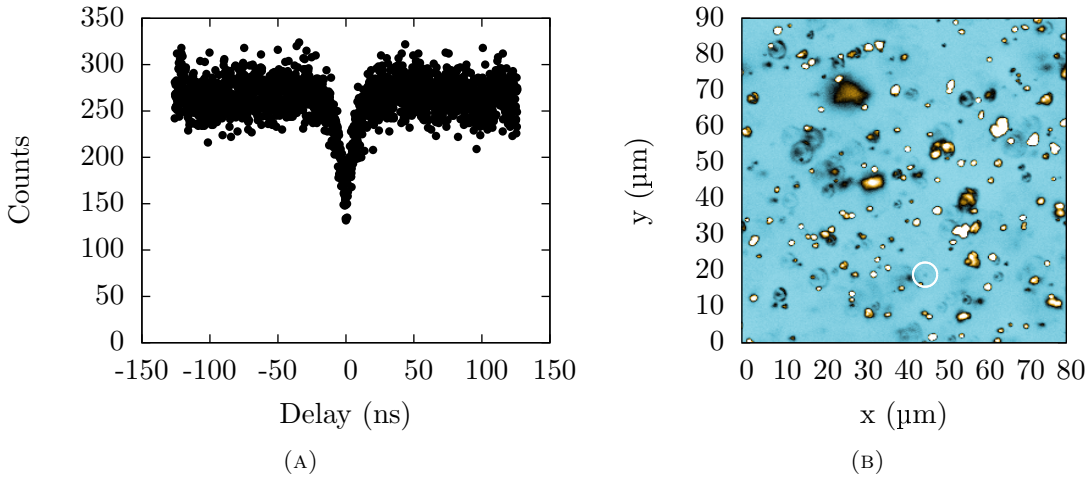

(A) (B)

FIGURE 3.9: (a) Anti-bunching data obtained for a slice of the glass sample G1, with (b) the corresponding location on the confocal scan shown with a white circle (see Fig. 3.8 for complete confocal scan image). The dip at $t = 0$ corresponds to sub-poissonian emission statistics and is indicative of single-photon emission (see Section 3.3.2). The shallowness of the dip shown here may be due to excitation of a few emitters (generally two or three, as the dip is still present) or a single emitter with a high background signal, both of which would degrade the single emitter dip. This data shows that non-classical (anti-bunching) emitters are present in the sample after glass processing.

amount of non-irradiated ND was chosen to achieve a similar concentration to the 50 g sample G1 (see Section 3.4.1).

The glass sample G2 was extruded (see Section 3.2.4) into a rod preform (P2) using a 10 mm rod die, to be drawn into a 160 µm outer diameter unstructured fibre. A section of preform P2 was characterised using Raman spectroscopy and PL spectrum measurements. The fibre F2 was the first trial fibre to include the non-irradiated ND. The fibre was pulled from preform P2 into an unstructured fibre with a nominal outer diameter of 160 µm.

3.4.2.1 P2: Photoluminescence

A PL spectrum taken from the bulk preform sample (Fig. 3.12) showed features consistent with NV centres. Figure 3.12 shows the PL spectrum of the preform, compared to spectra of ND powder and an undoped tellurite sample. The PL features of the preform sample match well with those of the ND powder, and the undoped tellurite background is featureless for the majority of the NV emission band. The spectra were all taken with a Raman spectrometer, using the 514.5 nm line of an argon ion laser, at a temperature of 80 K (rather than from the confocal microscope output as in Section 3.4.1.3).

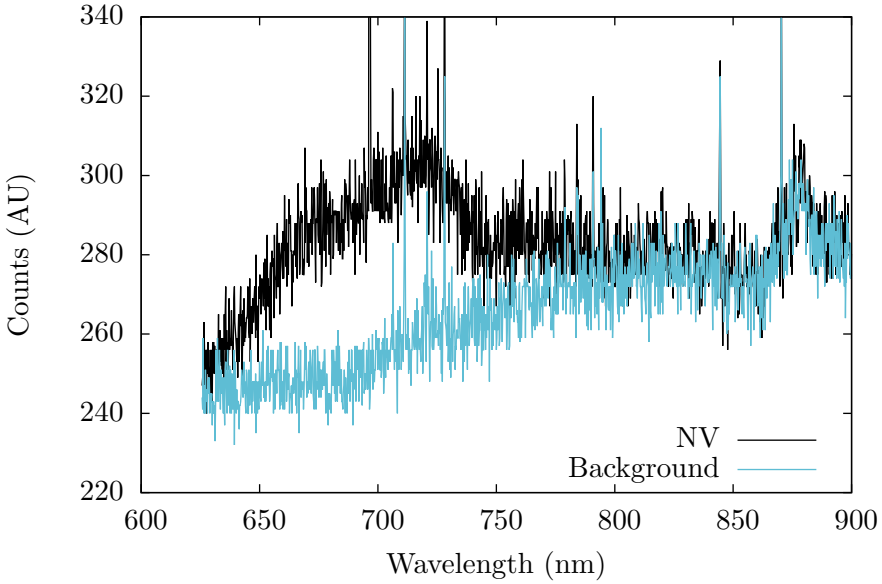

(A) NV centre and background

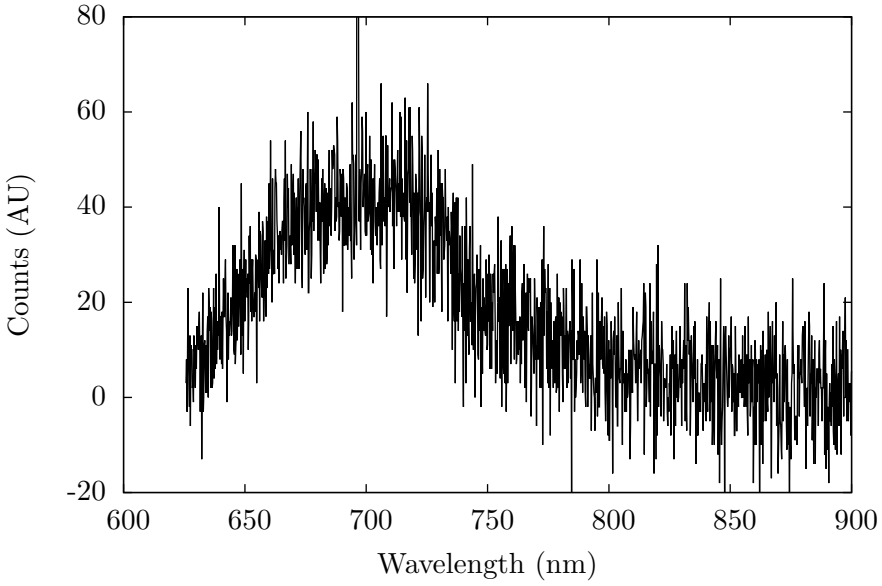

(B) Background subtracted

FIGURE 3.10: PL spectrum of the emitter shown in Fig. 3.9, with (a) the background glass spectrum for comparison, taken from the same sample scan in an area with no emitters, and (b) with this background spectrum subtracted from the NV emission. Taken with the 650–750 nm bandpass filter removed. The spectrum shows a PL signal consistent with an NV centre.

FIGURE 3.11: Sample G2, doped with non-irradiated ND. The dark appearance is attributed to the high diamond concentration, as for sample G1 above (see Section 3.4.1).

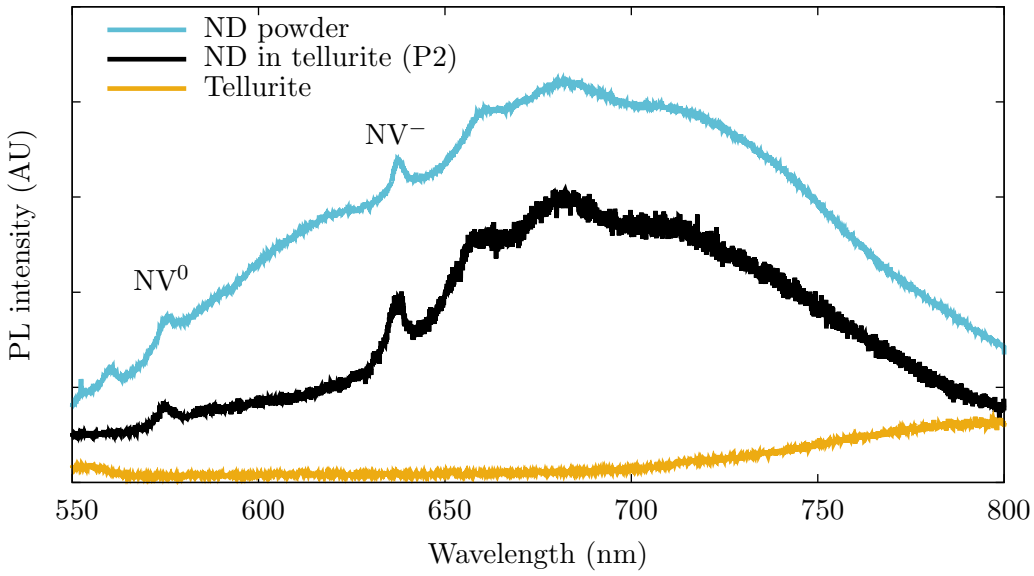

FIGURE 3.12: PL spectrum for preform P2, compared to undoped tellurite and ND powder. The ZPL peaks for NV^0 and NV^- emission are labelled. Taken at liquid nitrogen temperature (80 K) with an excitation wavelength of 514.5 nm.

3.4.2.2 P2: Increase in negative nitrogen-vacancy to neutral nitrogen-vacancy ratio

As discussed previously (see Section 1.1), the diamond NV centre can exist in either the NV^- or NV^0 charge state, and can switch between the two (e.g. photochromically [21]). The NV^- charge state is interesting as it shows spin polarisation and long coherence times at room temperature [20], and so the ratio of NV centres in charge state NV^- compared to NV^0 is a relevant property for other fields. This ratio was measured by taking the ratio of the areas under the curve corresponding to the ZPL of NV^- and NV^0 centres in the PL spectrum. The resulting data, shown in Fig. 3.13 for varying pump powers, indicate an increase in this ratio after incorporation into the tellurite glass. This

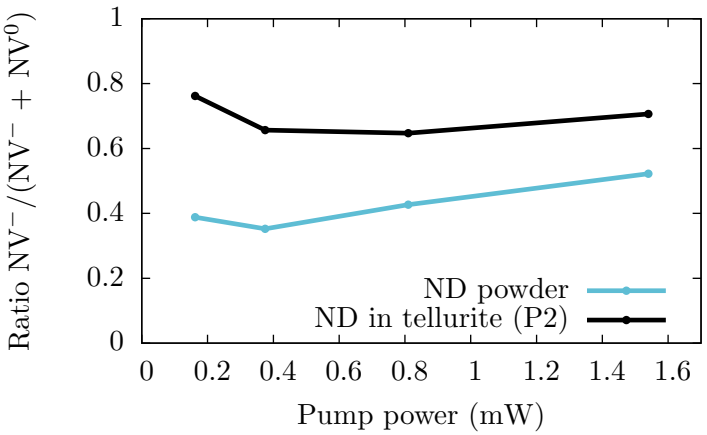

FIGURE 3.13: Ratio of PL, integrated over the ZPLs, of NV^- to total (NV^0 + NV^-). Shown for preform P2 and ND powder, indicating an increase in this ratio for diamond-tellurite glass.

is thought to be due to sp^2 carbon removal and oxygen termination of the nanodiamond surface from the fabrication process, and is consistent with that seen in single crystal diamond when oxidised through annealing [93].

3.4.2.3 P2: Preferential graphite oxidation in glass melt conditions

Raman spectroscopy confirmed the presence of diamond in the preform sample, as shown in Fig. 3.14. This measurement also showed that the graphite present in the ND powder, from a graphitic outer layer formed during production, was not present in the diamond-tellurite sample. This can be explained by preferential oxidation of the graphite layer due to the high glass melting temperatures of ∼700 °C.

The melting temperature is well above that at which graphite begins to oxidise (400 °C), but is, comparatively, only slightly over the diamond oxidation temperature of 630 °C to 670 °C [82]. This has been seen previously in 55 nm ND [81], where a reduction by a factor of 10 was seen in the graphite G-band of the Raman spectrum at 1600 cm^{-1} after annealing the powder at 400 °C for 20 min.

3.4.2.4 F2: Confocal microscopy

A confocal scan, shown in Fig. 3.15, was taken from the endface of the fibre F2. The fibre was cleaved and the pump beam was incident perpendicular to the endface such that the scan was over the plane of the endface (see Section 3.3.1). The edge of the fibre can be seen in the lower part of the image. Anti-bunching data was obtained for an NV emitter in this sample, also shown in Fig. 3.15, and a background-corrected $g^{(2)}(0)$

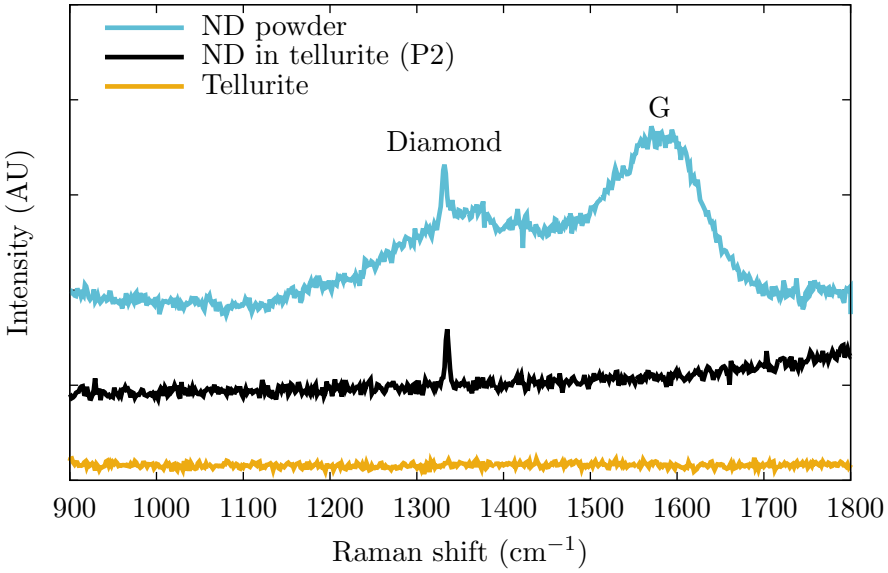

FIGURE 3.14: Raman spectrum of preform P2, compared to undoped tellurite and ND powder. The diamond and graphite G-band peaks have been labelled. It can be seen that the graphite G-band peak is no longer visible in the preform spectrum. The tellurite spectrum shows no Raman features in this range.

value of 0.04 confirmed that single photon emission could be seen from the NV after fibre processing (see Section 3.3.2). The tellurite background signal was ∼5 k counts s^{-1}, compared to the single photon emission rate of ∼45 k counts s^{-1}, with 1 mW excitation at 532 nm.

3.4.2.5 F2: Scanning electron microscopy

SEM imaging of the unstructured fibre was performed (see Section 3.3.4). Small defects in the cleaved cross-section were visible, as seen in Fig. 3.16. From investigation under the SEM (by zooming and changing depth-of-focus), these defects appeared to be bubbles.

Further investigation would be needed to confirm the cause of these defects, although several possibilities are now discussed. The defects could be due to particulates being removed during the cleaving process or gas bubbles formed during the glass fabrication. Possible particulates include compounds formed by reaction with the nanodiamond, such as tellurium (formed by reduction of TeO_2), or the nanodiamond itself; although the bubble edges are very regular and so inconsistent with the expected rough and irregularly shaped nanodiamond. Gases could have been produced by graphite or diamond burn-off creating CO or CO_2, reaction of the nanodiamonds with other glass components, or inclusion of air during swirling or casting. At the lower temperature of 700 °C the glass has a higher viscosity, which could hinder the release of trapped bubbles.

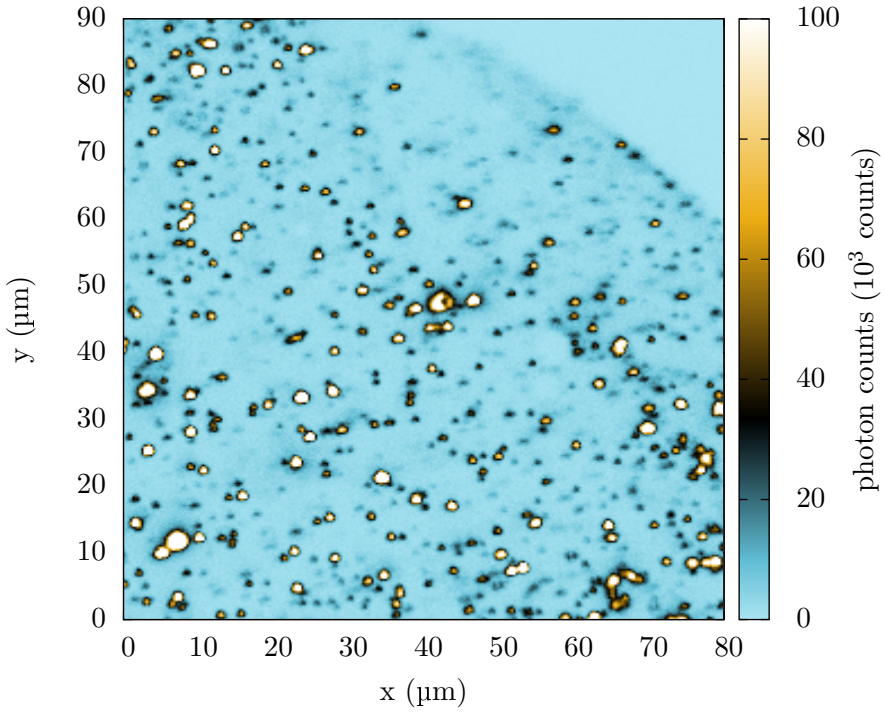

(A)

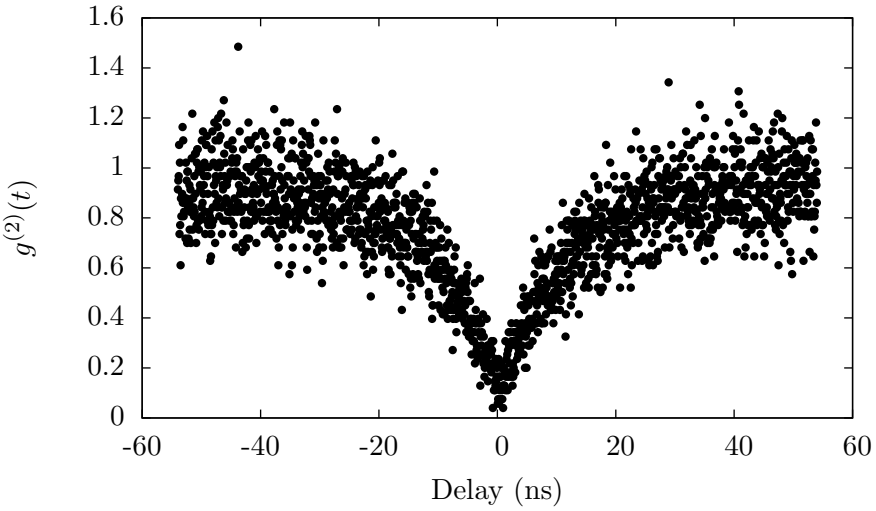

(B)

FIGURE 3.15: (a) Confocal image of fibre F2 cleaved cross-section showing emission from ND embedded in the fibre and (b) background-corrected anti-bunching data for an embedded NV centre, showing a $g^{(2)}(0)$ value of 0.04 (indicating single photon emission).

These defects are also seen in later bare fibres F3 and F4, as shown in Fig. 3.17. They are not seen in later structured fibres (see Section 4.2.3), however. This may be due to the smaller diamond doped region in the structured fibres, such that a lower volume of doped glass was viewed and (in combination with a low defect concentration) not enough cross-sections were investigated. The structured fibres also undergo an additional fibre draw-like process (called caning — see Section 4.1) which may have an effect.

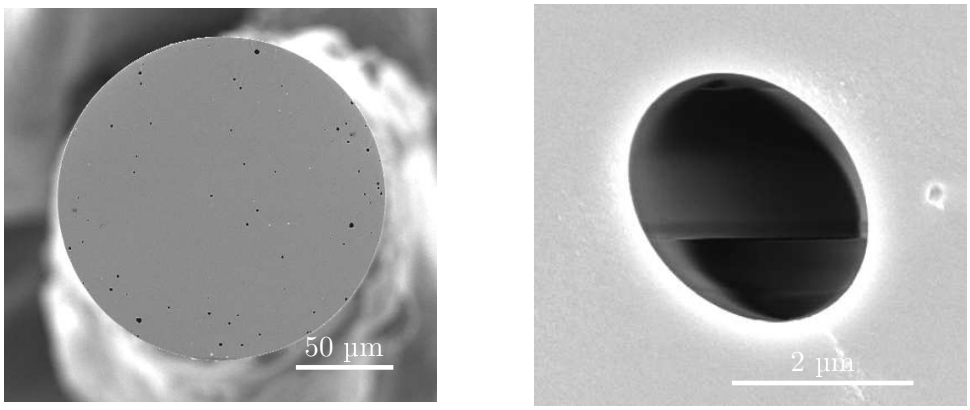

(A) (B)

FIGURE 3.16: SEM images of fibre F2, showing (a) the bare fibre and (b) a magnified image showing one of the holes in detail.

3.4.3 G3 reduced nanodiamond concentration

The dark appearance and confocal imaging of sample G2 showed that the ND concentration was too high. This would be a source of high loss in the fibre and would reduce the chance of finding and characterising single emitters, as the finite resolution of the confocal system would not be able to resolve closely agglomerated single centres. Sample G3 was made with the aim of reducing this concentration by as much as possible, while still allowing confocal characterisation of the centres. The maximum confocal scan window was 100 µm × 100 µm and so the concentration had to be high enough to show a quantity of emitters on each scan (generally of the order of 20) such that single centres could be found in a reasonable timeframe.

In this sample 0.94 mg of dry ND powder was added to the glass melt, which was the minimum amount practical using a pure dry powder. The limitation was due to the weighing equipment precision (±0.01 mg) and handling considerations; there are small losses in powder from transport in the laboratory and through the glovebox airlock, and when pouring into the crucible (due to static and air suspension). These losses become a

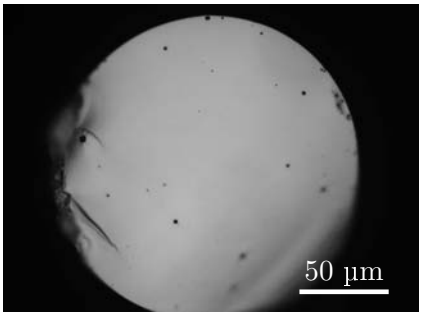

(A) Fibre F2

(B) Fibre F3

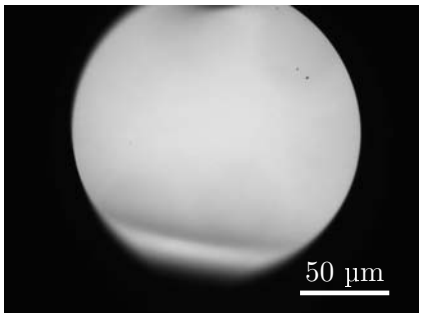

(C) Fibre F4

FIGURE 3.17: Microscope images comparing defects seen in (a) fibre F2 to those of fibre (b) F3 (see Section 3.4.3) and (c) F4 (see Section 3.5.1).

large proportion of such low sample quantities, which limits the measurement accuracy of the added ND mass.

Unfortunately, the preform P3, made from the billet G3, began bending during extrusion and so only a short piece was available for drawing. The fibre draw, F3, was not successful in pulling the target 160 µm diameter unstructured fibre, but produced lengths of glass with diameters ranging from around 0.5 to 2 mm. Confocal imaging was performed on these sections of F3.

3.4.3.1 P3: Loss measurements

Loss measurements, using UV-Vis, were performed on the resulting preform (P3). The loss spectrum is shown in Fig. 3.19a and, as for glass G1 (see Section 3.4.1.1), is also plotted as a function of inverse wavelength to the 4^{th} power (λ^{-4}) in Fig. 3.19b. Both spectra have been normalised to the sample thickness of 4.7 ± 0.1 mm after subtracting Fresnel reflections (see Section C.3).

FIGURE 3.18: G3 billet.

Interestingly, this spectrum does not show a Rayleigh scattering-like dependence, where the loss is proportional to λ^{-4}, as for glass G1. This suggests that scattering from particles much smaller than the wavelength (400–800 nm) is not the main mechanism for loss in this sample. The background loss is reduced, compared to glass G1, from $\sim$2000 dB m^{-1} to $\sim$500 dB m^{-1}. This may be a result of the much lower diamond concentration (9.4 ppm wt. compared to 320 ppm wt. in glass G1).

There is a pronounced dip in the loss between 450–550 nm, which explains a blue tint to the glass in transmission (unfortunately not visible in Fig. 3.18, but see later glass sample images such as Fig. 3.25 and Fig. 4.4). This blue tint appears in all later samples (G4, G5, G6), and the origin of this dip in absorption is currently being investigated.

3.4.3.2 F3: Confocal microscopy

Confocal imaging of fibre F3 showed a reduced concentration of NV emitters compared to the high concentration sample F2, as expected. These are compared in Fig. 3.20, showing the concentration reduction. As can be seen, the emitters are much more widely spaced in sample F3 and particle sizes are smaller, indicating that ND agglomeration is reduced. This reduced concentration makes it easier to find separate emitters for single emission characterisation. Two or more emitters within the confocal pump beam (300 nm diameter and $\sim$1 µm focal length) degrades the anti-bunching data as the single emission from each centre combines into a multi-emitter signal. With a larger spacing between NDs, there is a much higher chance that two or more single emitters are separated enough to be resolved by the confocal system. Anti-bunching data from one of the centres, along with the confocal image showing the centre measured, is shown in Fig. 3.21 and confirms that single emission is seen in the final fibre (see Section 3.3.2).

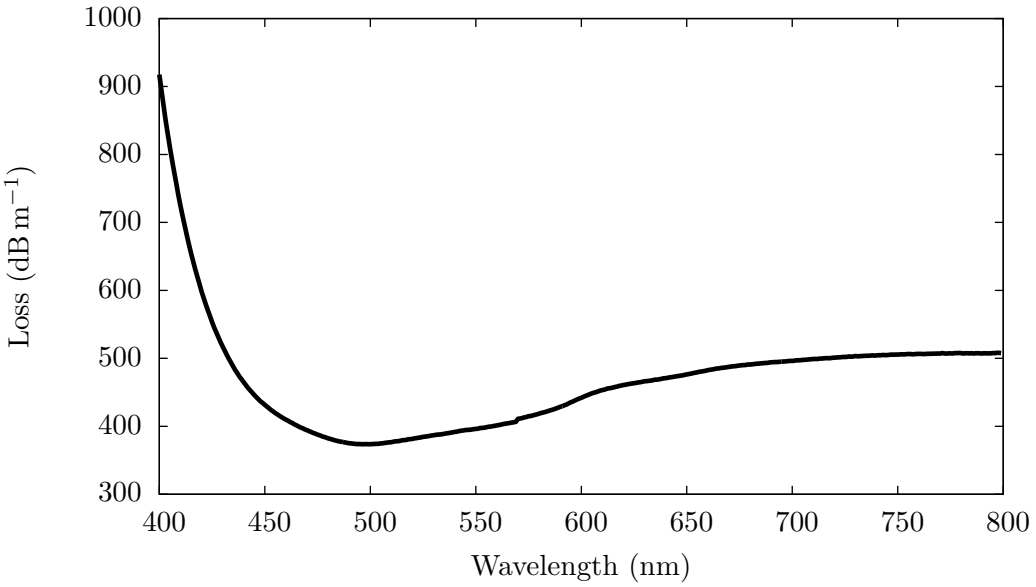

(A)

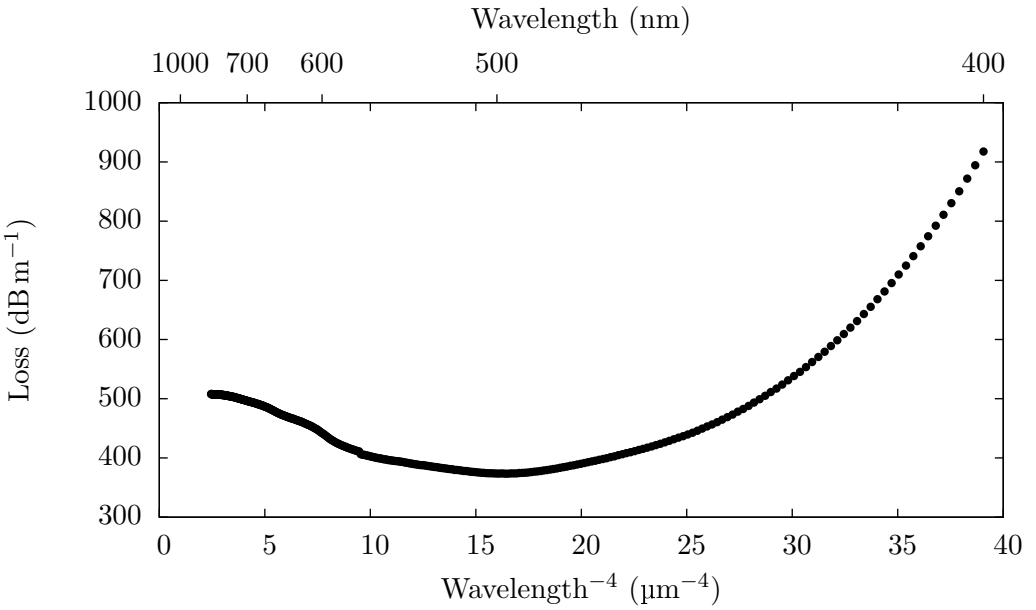

(B)

FIGURE 3.19: (a) Loss vs. wavelength for sample P3 measured using UV-Vis. (b) Loss vs. wavelength^{-4} for sample P3. Spectra have been normalised to the sample thickness of 4.7 ± 0.1 mm. Loss due to Fresnel reflection has been subtracted from both spectra (see Section C.3).

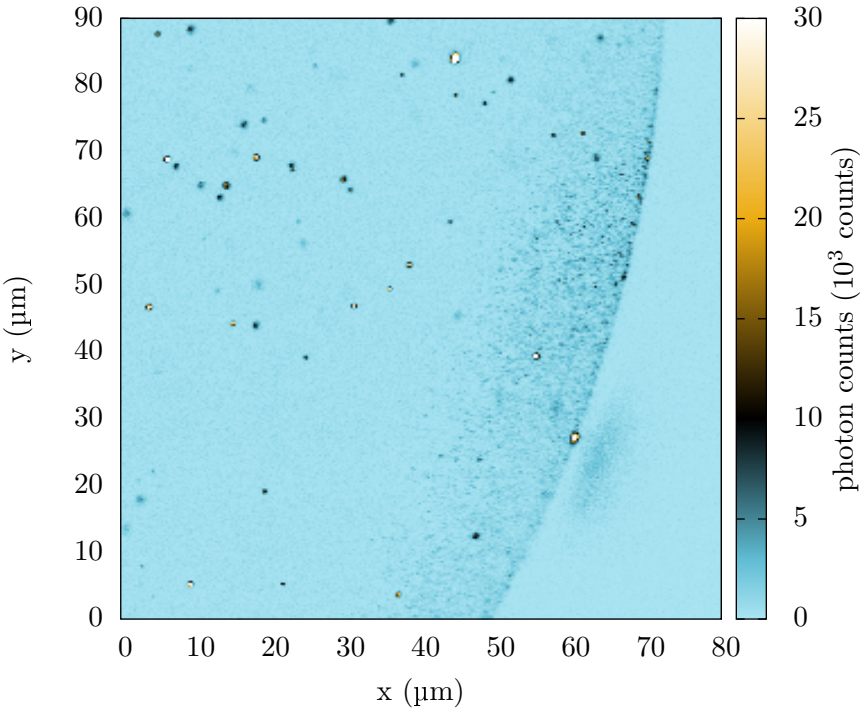

(A) F3: 9.4 ppm wt. ND

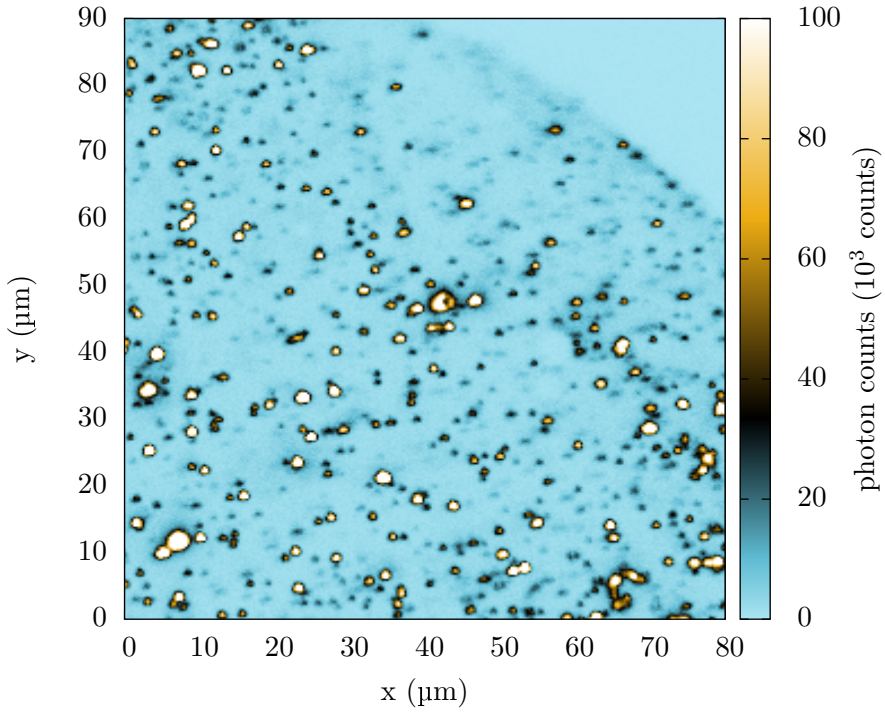

(B) F2: 280 ppm wt. ND

FIGURE 3.20: Comparison of NV density for (a) the low concentration (9.4 ppm wt. ND) F3 sample and (b) the high (280 ppm wt. ND) concentration F2 sample.

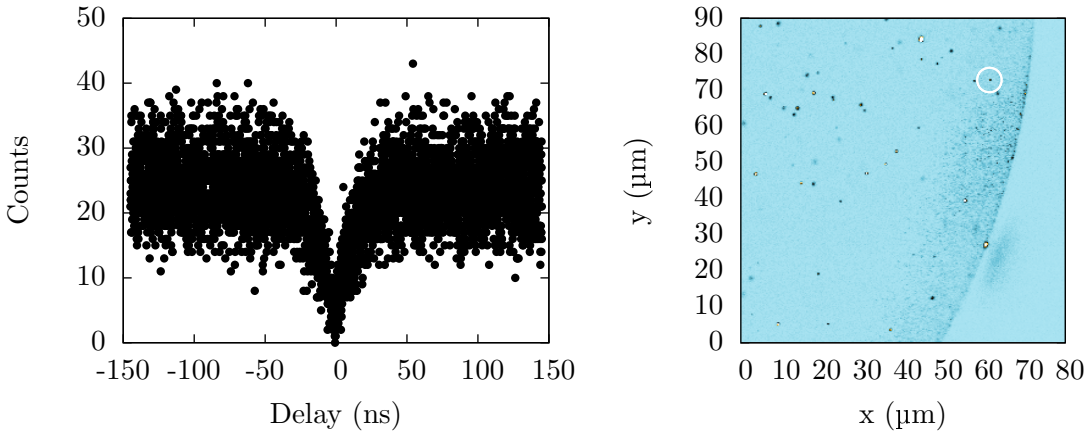

(A) (B)

FIGURE 3.21: (a) Anti-bunching data (see Section 3.3.2) and (b) the corresponding confocal scan with the anti-bunched NV centre circled in white (see Fig. 3.20a for the complete confocal scan) for fibre F3. The dip at zero delay time indicates single photon emission, showing that the NV emitters have retained single emission characteristics throughout the fibre fabrication process.

3.5 Further reducing nanodiamond concentration

The results shown thus far demonstrate that it was important to find a method of reducing the concentration of ND incorporated into the glass to reach the goal of well-spaced single emitters for single photon source applications. From the previous glass sample, G3 (see Section 3.4.3), it was clear that, effectively, the minimum concentration had been reached for methods based on adding dry powder. Reducing it further by this method would involve increasing the glass melt mass (as the minimum dry powder amount had already been used) and this would not scale well — for example, in order to reduce the concentration by only a factor of 10, a glass billet mass of 1 kg is required. A billet of this size is difficult to manufacture using most laboratory equipment, and so reducing this concentration by an order of magnitude or more would become unviable using this method.

The lowest concentration obtained using dry powder addition (as seen in Fig. 3.20a) is still far too high to allow the fibre length to be separated into separate devices, each containing a single NV, for the fabrication of a single photon source (see Chapter 1). Although the ND is well separated for confocal characterisation, each small section of fibre would still contain many single emitters. A scalable dilution method is required to allow customisation of the ND concentration due to variation in fibre core size, device length and proportion of NDs containing an NV colour centre.

3.5.1 G4 nanodiamond dilution

Sample G4 was a trial to reduce the ND concentration by diluting the fabricated ND-tellurite glass into a new undoped melt of tellurite. Instead of adding dry powder to the melt, we instead added 0.511 09 g of preform P3, made from glass G3 (see Section 3.4.3). This would give an ND mass of 4.8×10^{-3} mg for the 100 g glass melt (assuming no losses from either of the melts).

FIGURE 3.22: Image of billet G4.

This billet was used to fabricate a bare fibre (F4). Although emitters in the fibre were visible on the confocal system, no signs of single photon emission was seen from any of the 40+ emitters characterised. From experience with previous glass samples and other NV samples it was expected that single emission (or weak signs of anti-bunching from 2- or 3-centre ND) would have been seen after this number of emitters. Figure 3.23 shows one of these confocal scans for comparison to the previous bare fibre samples.

Very recent work done at IPAS, University of Adelaide, has shown that undoped tellurite glass melted at the low temperature of 700 °C contains fluorescent nanoparticles. These are assumed to be gold nanoparticles, originating from dissolution of the gold crucible. The relatively high number of (non-single) emitting centres could thus be gold nanoparticles and the longer melting time of the dilution trial might have destroyed the ND in the glass. This is supported by the high concentration of emitters, compared to that expected from this amount of dilution. The undiluted fibre F3 should contain ∼200 times the quantity of diamond of this diluted fibre, but a comparison of the confocal images (Fig. 3.20a for F3 and Fig. 3.23 for F4) shows a similar concentration — suggesting that these emitters are not diamond.

More investigation into ND dilution would likely be required for the realisation of a useable device. This was not studied further in this project, as a relatively high concentration was required for the confocal measurements (due to a small scanning area of $100 \times 100\,\mu$m) and the previous sample, G3, was already an effective concentration

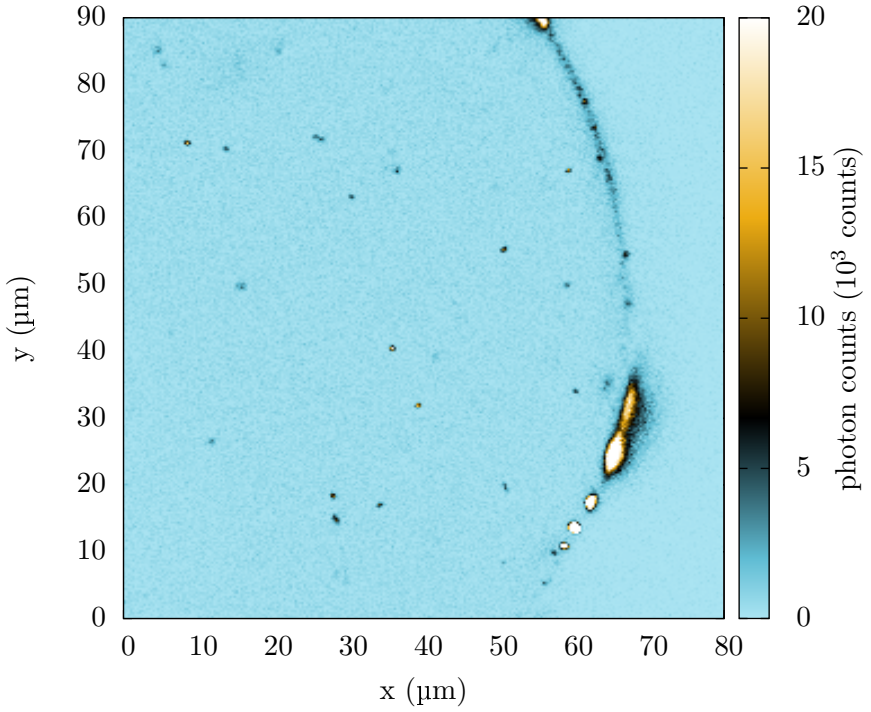

FIGURE 3.23: Confocal scan of fibre F4, from glass billet G4. This billet was made by diluting an ∼0.5 g piece of preform P3 (from billet G3). This dilution gives a theoretical ND concentration, assuming no losses from either melt, of 4.8×10^{-2} ppm wt.

for this. Once single emission capture into the fibre guided modes had been shown experimentally, the dilution experiments would become much more relevant. This would involve investigation into the reasons behind loss of single photon behaviour from the dilution method discussed here, and into alternate dilution methods.

3.6 Irradiated nanodiamond

Irradiated ND was also embedded in tellurite glass. This 50 nm ND was irradiated with 2 MeV electrons at 10^{18} cm^{-2} to create vacancies and then annealed at 800 °C for 2 h to allow movement of these vacancies to nitrogen impurities in the diamond, to create additional NV colour centres. After this process a much larger proportion of NDs contain centres and so show emission, and generally emission from each ND is much brighter (see Fig. 3.24) from the higher NV concentration.

A disadvantage of using irradiated diamond is that, for the ND size and irradiation parameters here, most ND will contain more than one NV centre and so the probability of finding a single photon emitter is actually reduced. Because of this, the irradiated 50 nm ND would most likely not be used for a final device. However, for trial glasses

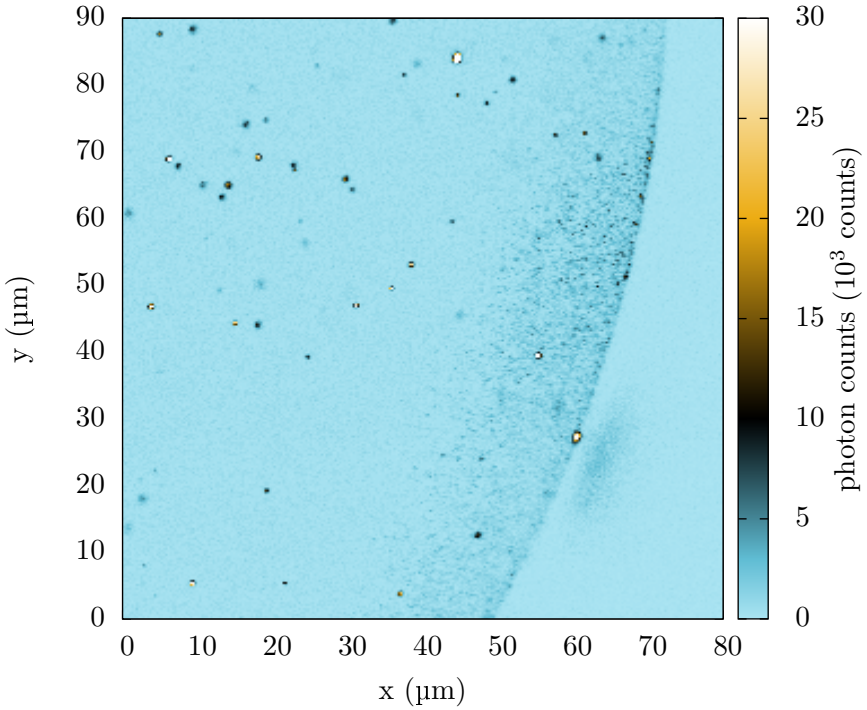

(A) Non-irradiated (F3)

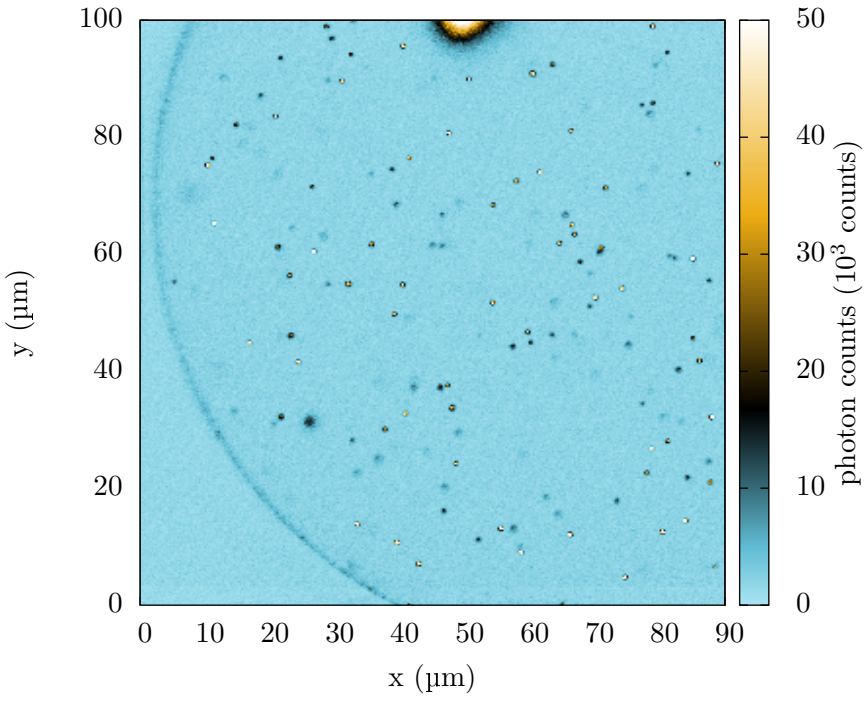

(B) Irradiated (F5)

FIGURE 3.24: Comparison of emission from (a) non-irradiated ND (9.4 ppm wt.) sample F3 (see Section 3.4.3) and (b) irradiated ND (8 ppm wt.) sample F5 (see Section 3.6.1). Notice that the irradiated ND shows more emitters and also the average brightness of the emitters is higher.

these nanocrystals increase the detectable photon count rate; which is an advantage for locating the ND in challenging geometry, such as small-core fibres, and also improves the signal-to-noise of measurements such as emission spectra. These irradiated ND glass samples are thus useful for proof-of-concept experiments of the emission capture into the fabricated fibres, in advance of single photon capture.

3.6.1 G5 irradiated nanodiamond-doped

This glass sample, G5, was a 100 g cylindrical 3 cm diameter tellurite billet, adding 0.8 mg of 50 nm irradiated ND. An image of the billet is shown in Fig. 3.25. This billet was extruded into a rod preform (P5) and drawn into a 160 µm outer diameter unstructured fibre (F5). A confocal scan of the endface of fibre F5 is shown in Fig. 3.24. As expected, the fibre shows a higher concentration and overall brightness of NV emitters when compared to the non-irradiated ND-doped fibre F3, which has been doped equivalently (similar in method and ND concentration).

Glass sample G5, and the resulting fibre sample F5, showed that the irradiated ND was suitable for inclusion in tellurite, and for fibre fabrication. Future work would involve fabrication of a structured fibre using this ND type and demonstration of emission capture from the NV into the fibre guided modes. Although single photon emission would not likely be possible, this would demonstrate the fundamental experiment of NV pumping and emission collection from a doped fibre.

(A) Side view (B) Bottom view

FIGURE 3.25: Images of G5 billet.

3.7 Conclusion

The glass fabrication presented in this chapter was the first demonstration of a hybrid nanodiamond-glass material, leveraging the advantages of room-temperature, stable single photon emission and a flexible, well-researched fabrication pipeline. Tellurite glasses with embedded diamond nanocrystals were fabricated and drawn into unstructured fibres. Confocal imaging and anti-bunching measurements confirmed that the diamond survives the fibre processing steps and still shows single photon emission.

Fabrication of a hybrid diamond-tellurite material was not only successful, but also improved aspects of the included diamond. Raman spectroscopy showed that the graphite present in the diamond powder is removed during the glass melting and analysis of the emitted NV spectra showed an increase in the desirable NV^- charge state of the centre due to the surrounding tellurite material.

This hybrid material can be used in almost any fabrication processes applicable to the base tellurite glass, from the extrusion and fibre drawing process described here to focused ion beam-milled, photonic crystal, or femtosecond direct-write slab waveguides or cavities. Other uses of the NV centre, such as in magnetometry [22], can also benefit from the wide fabrication experience in tellurite and leverage the advantages of a fibre platform — long interaction lengths, strong field interaction and confinement, and remote read-out.

Future work would be needed to investigate the mechanisms behind the high transmission loss of this material in more detail, and reduce this background loss. The losses of the fabricated glasses presented here are high for an optical fibre and limit the effective fibre length to centimeters.

These results showed that, through the extrusion process that has been validated here, a fibre with a more complicated cross-sectional design, such as a suspended core structure, would be possible with this hybrid glass. In Chapter 4 the results of this next step, towards an efficient single photon fibre device, are show with the fabrication of a small-core, high index contrast, diamond-tellurite suspended core fibre.

4

Microstructured Fibres

Optical fibres require a refractive index variation to guide light, by either inducing total internal reflection or a bandgap effect (i.e. photonic crystals). This variation can be done using selective doping of the same material (e.g. germanium doping in silica), combining two or more materials with differing indices, or, as for this project, introducing regions of air by shaping the material.

In this chapter, the results of the microstructured fibre fabrication and characterisation will be presented. The previous chapter (see Chapter 3) showed results for the fabrication of the diamond doped glass and unstructured fibres, which became the basis for the fabrication of the microstructured fibres presented here.

Similarly to Chapter 3, the samples will be shown from initial glass to final fibre with characterisation data and discussions. The progression from the initial fibre to the final design will be shown, with the measurement results explaining the reasoning behind each new design or process. The chapter will then be completed with a conclusion of the results.

The focus of this fibre fabrication has been on a variation of a suspended core structure, called a 'wagon-wheel' fibre, consisting of a central core region suspended in air by three supporting struts, which connect the core to the outer cladding. The design is effectively a glass core surrounded by an air cladding, leading to a high refractive index contrast — the function of the outer glass cladding is for structural robustness only. This wagon-wheel design is a well-known [1, 48, 49, 50, 51] and routinely fabricated fibre design. It forms the basis for the fibre fabrication presented here precisely because of this familiarity with its construction.

A derivative of the wagon-wheel fibre is the exposed core wagon-wheel, where a section of the outer cladding is removed. This has been previously fabricated in a lead-silicate glass [94, 95], called F2, and is useful in applications where access to the core is an

advantage (such as for sensing). This fibre structure is discussed later in the chapter (see Section 4.3), where a similar fibre design is required for successful side imaging of the wagon-wheel core. In this case a thin section of cladding glass was left to protect the core from debris and damage, and so is referred to as a 'lidded' wagon-wheel to distinguish it from the case where the core is fully exposed.

4.1 Wagon-wheel fabrication

Wagon-wheel fibre fabrication uses the same basic extrusion and drawing techniques as for the previously shown unstructured fibre (see Section 3.2.4), but with additional steps to deal with the non-trivial structure. For reference, the full process is shown below and a schematic is shown in Fig. 4.1.

The preforms for these fibres generally use a 50 mm diameter billet, compared to the 30 mm billets used for unstructured fibre fabrication (see Section 3.2.4). For extrusion the same glass volume is fed into the die, and so the ram feed rate is reduced to $0.07\,\mathrm{mm\,min^{-1}}$ because of the larger billet area (the ratio of areas gives $(15)^2/(25)^2 \times 0.2\,\mathrm{mm\,min^{-1}} = 0.07\,\mathrm{mm\,min^{-1}}$).

There are two main differences to the fabrication of an unstructured fibre. Firstly, the use of a complex die pattern to create the structure in the preform (see Fig. 4.2) needed for the fibre to guide light. Secondly, a preliminary draw step, called 'caning', is performed, where this complex preform is reduced in diameter before the final draw step. This cane section is then fit into an undoped tellurite tube, with an outer diameter similar to the unstructured fibre preforms (around 10 mm) and an inner hole for accepting the cane. This caning, done on the fibre draw tower, is used to increase the cladding size enough for a robust (160–200 µm diameter) fibre without the entire cladding thickness needing to be fabricated on the initial preform. The die diameter is limited and so this caning allows larger feature sizes for the core region — without this step, most of the die would be needed for the cladding and feature sizes are limited due to machining tolerance and the extrusion process.

The assembled cane-in-tube preforms were mounted into a fibre draw tower and drawn down into optical fibres.

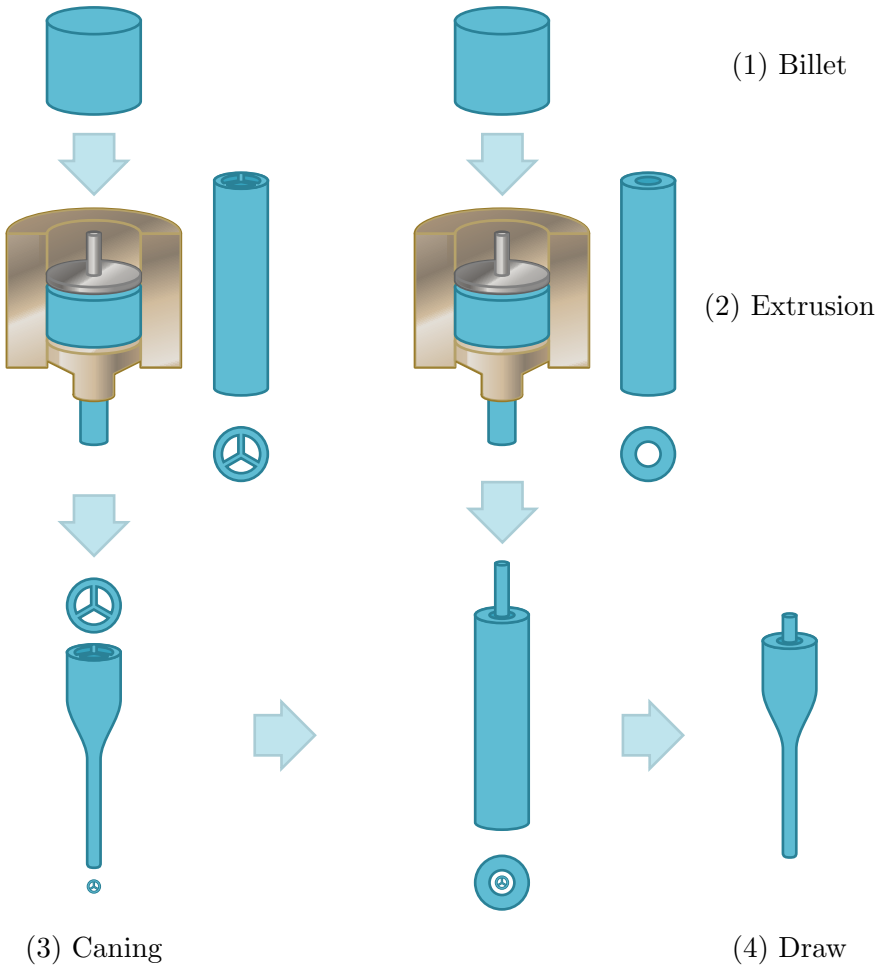

FIGURE 4.1: Structured fibre fabrication schematic.

Structured fibre fabrication

1. Fabricate two glass billets for core and cladding (see Section 3.2.3).
2. Extrude cladding tube and wagon-wheel preform (see Section 3.2.4).
3. Reduce wagon-wheel preform structure on fibre draw tower to create cane.
4. Insert well-fitting cane piece into tube preform and draw into fibre on tower.

Components were annealed after each step before the final fibre draw.

FIGURE 4.2: Die design used to fabricate a wagon-wheel preform.

4.1.1 Using pressurisation and vacuum

The cane and tube sections are separate components and need to be fused. This gap seals as the cladding collapses and the cane inflates during the fibre draw. Some of the fibre draws required external pressurisation or vacuum applied during the draw to expand the microstructured holes or to help in the fusion of the cane and cladding sections. The general procedure for this pressurisation will be discussed here and, if used, will be noted in the individual sample descriptions below.

The simplest case of pressurisation involves sealing the cane section at the end and using the trapped air to pressurise the hole regions (called 'self-pressurisation'). Pressure can also be manipulated in either the core holes or the area between the cane and the cladding tube; by applying actively controlled pressure to the cane section to inflate the holes, or applying a vacuum to the cladding tube (effectively inflating the cane section, but without actively pressurising this area), respectively. Schematics of these different techniques are shown in Fig. 4.3.

4.2 Wagon-wheel fibre samples

4.2.1 G6 non-irradiated nanodiamond-doped 50mm billet

As the first sample made for wagon-wheel fabrication, G6 was batched as a 300 g melt. It was melted as for the previous samples (see Section 3.2.3), adding 1 mg of non-irradiated nanodiamond. The melt was cast into a 50 mm diameter cylindrical mold and the final billet height was 28 mm.

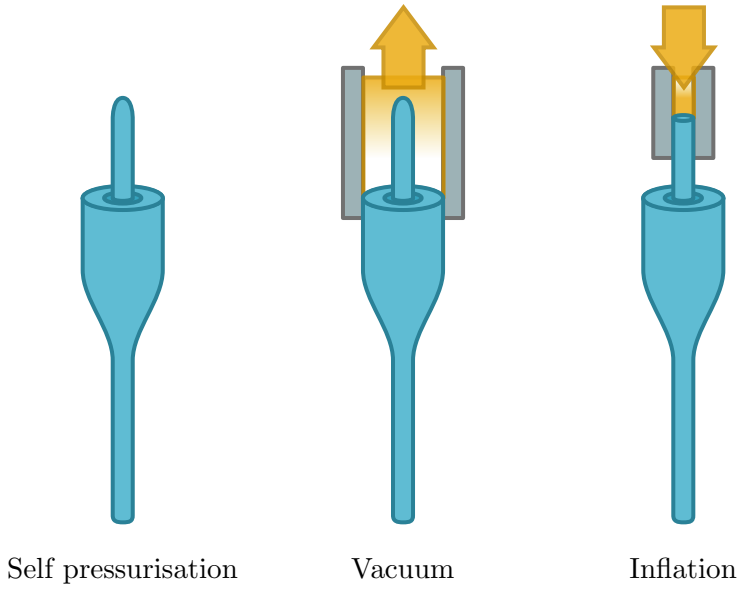

FIGURE 4.3: Diagram of the different pressurisation schemes.

(A) Side view (B) Bottom view

FIGURE 4.4: Images of G6 billet.

4.2.2 P6 wagon-wheel preform

The preform P6 was extruded at 360 °C with a ram speed of 0.07 mm min^{-1} (see Section 4.1). The preform images are shown in Fig. 4.5. This preform was caned down for insertion into a jacket tube and drawing into fibre. The cane sections were used for the fibres F6a, F6b, and F6c (see below).

4.2.3 F6a wagon-wheel fibre

F6a was the first wagon-wheel fibre draw with an ND-doped core, using cane from preform P6. The fibre was drawn (see Section 4.1) to an outer diameter of 160 µm.

(A) Cross-section (B) Side

FIGURE 4.5: Images of wagon-wheel preform P6.

From SEM images (see Fig. 4.6), the core diameter (measured by the largest circle that would fit in the core area) was found to be 1.47 µm.

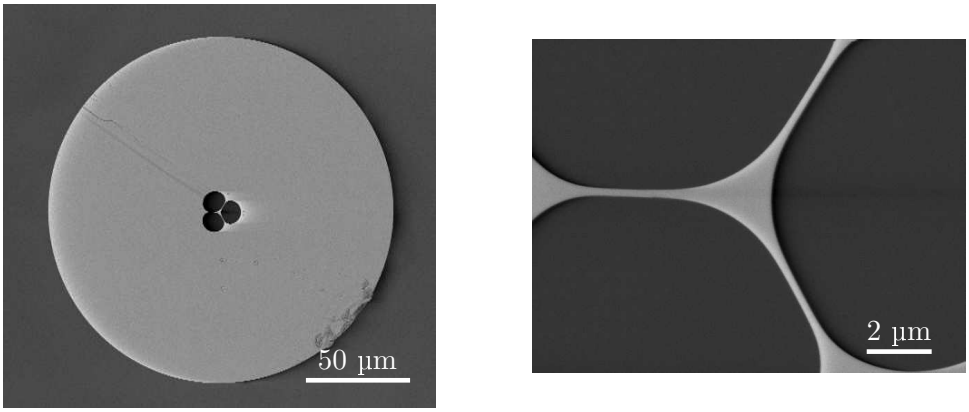

(A) Cross-section (B) Core region

FIGURE 4.6: SEM image of wagon-wheel fibre F6a.

Confocal imaging was performed, as for the previous fibre samples (see Section 3.3.1), to verify that the NV centre properties were retained after the new processing steps required by the wagon-wheel fibre fabrication. Also, confocal microscopy is a convenient way to investigate single photon capture, as a single centre can be pre-characterised and then individually pumped to look for a guided single photon signal from the fibre. A typical endface scan image of the fibre is shown in Fig. 4.7a, where the confocal image is taken facing the cleaved end of the fibre (similarly to the unstructured fibres, for example Sections 3.4.2.4, 3.4.3.2 or 3.5.1). The confocal image shows two PL features; strong emission in the fibre core region, and an outer 'ring' (labelled on Fig. 4.7a) surrounding the fibre hole geometry.

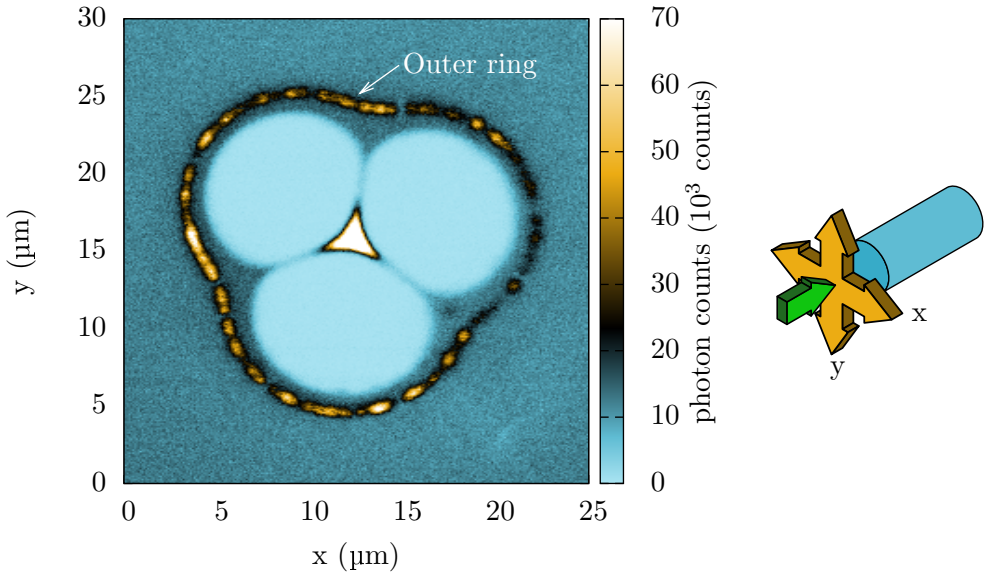

(A) Confocal image

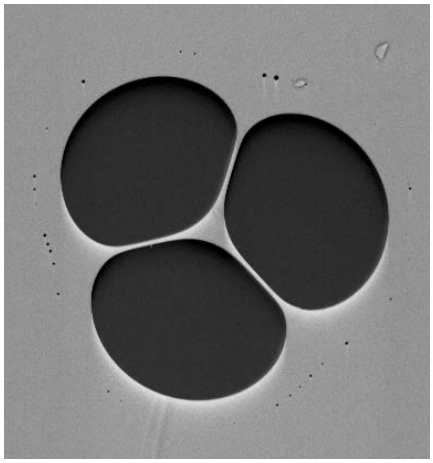

(B) SEM image

FIGURE 4.7: (a) Confocal image of the endface of wagon-wheel fibre F6a, with a schematic of the confocal scan axes (orange arrows) and laser incidence (green arrow). (b) SEM image showing the cane-tube interface by the small holes surrounding the main wagon-wheel holes (due to incomplete fusion).

The outer ring of fluorescence is thought to be from contaminates (such as dust) introduced during fabrication, either present on the cane piece or inner section of the tube preform before the final fibre draw (see Section 4.1). The feature is in a similar location to where the cane-tube interface would typically be in a wagon-wheel fibre (see Fig. 4.7b) and the counts from this region photobleach quickly, which is consistent with results from contaminates seen on the surface of other characterised samples. The

contaminates are distinguishable from NV, which does not photobleach.

The strong core emission is due to the increase in background glass fluorescence from the guiding nature of the wagon-wheel fibre. PL spectra taken by the confocal microscope at the core region showed tellurite glass fluorescence and did not show any features consistent with NV emission. Previously, the fibres imaged by confocal were bare, unstructured fibres. Due to the large (160 µm) core diameter, the guided light (and so the captured glass fluorescence) is spread over a very large area. Creating the wagon-wheel structure has tightly confined the guided modes and so an increase in glass fluorescence is seen because of two effects: (a) a stronger recapture of the glass fluorescence due to the higher fibre NA, and (b) a higher intensity due to the smaller mode area. This background signal obscures the low signal counts of the embedded NV such that the confocal characterisation of the NV centres cannot be performed by scanning the endface, as was done previously for the bare fibre.

Confocal imaging through the side of the fibre was tried, to reduce the background signal seen when end-pumping the fibre by exciting a smaller glass volume with the pump (avoiding pump guidance and also simply imaging through a shorter section of glass). One problem with this configuration was the distortion associated with imaging through the cladding — a section of high index material approximately 80 µm thick, with a curved interface. The core diameter of ∼2 µm was a small feature to pick out with a confocal resolution of 0.3 µm and so any distortion would create imaging problems. As suspected, imaging through the entire fibre cladding with the confocal distorted the pump beam and blurred the fine detail needed to image the small core area. Figure 4.17 shows this effect with an image of the fibre cross-section taken from the side face (i.e. the fibre is moved towards/away from the lens, moving the lens focus into the fibre material, instead of the more conventional side-to-side movement). As can be seen in this image, the core region loses detail as a result of the cladding distortion.

Methods of removing cladding material, including etching and mechanical polishing, were unsuccessful. Mechanical polishing left a poor surface quality due to scratching and the deposition of contaminates, and etching created a precipitate that was difficult to remove. Any debris or particulates create a strong PL signal from the sensitive photodetectors that make imaging more challenging. It was later found (again referring to Fig. 4.17) that even a small section of material distorted the core details significantly. These methods would not allow the control needed to create the thin cladding sections needed (see Section 4.3.5). Mechanical polishing would either break the fibre as it became too thin, or would not have the resolution needed for this thin a section and would break through to the core. Etching would remove material from the entire

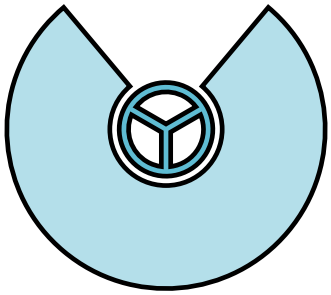

FIGURE 4.8: Schematic showing the fabrication of the lidded wagon-wheel fibre using a wagon-wheel cane and a slotted cladding tube.

cladding perimeter, and so to reduce the cladding to this thickness would weaken the fibre structure considerably and make manual handling almost impossible.

A proposed solution was to fabricate a fibre with an exposed, or near-exposed, core section, while retaining the cladding structure around the non-exposed areas. This fabrication is discussed in the next section.

4.3 Lidded wagon-wheel fibre

The next step to attempt to improve imaging of the core region was to fabricate a wagon-wheel fibre with a length of exposed core, where the cladding material is removed. The aim was to leave a small section of cladding material to protect the core area from debris, which would cause additional loss and also contribute background PL to the confocal scans, and prevent damage. As discussed above (see Section 4.2.3, and also shown below in section 4.3.5), the thickness of intervening material is critical to the success of confocally imaging the core and so a thin section was required. Such a thin section of cladding could be more easily fabricated by including it from the beginning of the fibre fabrication, rather than removing material post-fabrication. By fabricating this thin cladding section as a part of the preform, it could be made at macroscopic dimensions and then drawn down into the final fibre, using the scaling effect of the draw process to allow a lower tolerance on the fabrication and still produce very small features (as for other fibre features).

The proposed design for this exposed fibre was to fabricate a 'lidded' wagon-wheel, where a thin section of glass is left from the cladding to protect the core. The first trials (F6b and F6c) used a slotted cladding tube and a standard wagon-wheel shaped cane (doped with ND) from preform P6, so that the thin lid section would be created by the outer wall of the cane (see Fig. 4.8).

4.3.1 T6b tube with extruded slot

For the first lidded wagon-wheel fibre, F6b, a slot was introduced in the tube wall along the entire length of the tube. This outer tube design was successfully used to fabricate a lead-silicate glass (called F2) exposed-core wagon-wheel fibre [95]. By creating a tube die with a slot-shaped pin a slotted tube could be extruded. The pin design was shaped to create a circular hole below the slot so that the cane piece would be well-fitted within the cladding tube. The extrusion die and resulting preform, T6b, are shown in Figs. 4.9 and 4.10, respectively.

FIGURE 4.9: Images of the extrusion die used for the outer tube preform T6b.

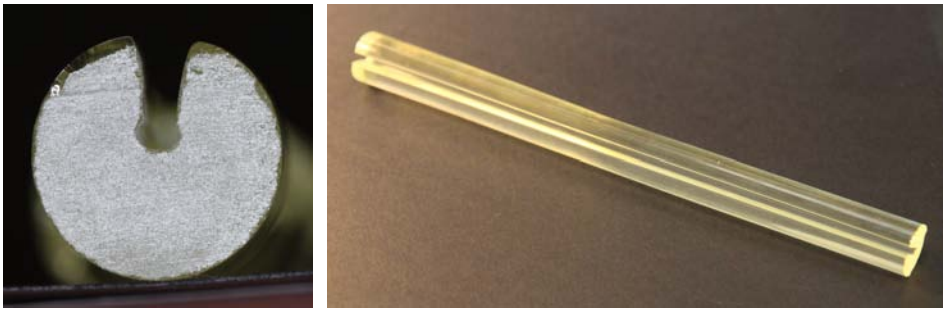

FIGURE 4.10: Images of the final preform shape obtained for the outer tube preform T6b. Note that the slot runs the complete length of the tube.

4.3.2 F6b lidded wagon-wheel fibre

A microscope image of the pulled fibre, using the slotted preform tube T6b and cane fabricated from preform P6, is shown in Fig. 4.11. This image shows that the fibre draw failed, the cane and tube sections did not fuse during the fibre pull and the slot in the tube distorted due to the glass surface tension. Two changes were made in the draw process for the second trial (see Section 4.3.3) from the results of this fibre. Firstly, a gradual slot was cut into a solid tube using a cutting saw, so that the sections would be

allowed to fuse before reaching the slotted section of the tube. Secondly, the cane was actively pressurised to assist in fusing the cane and tube.

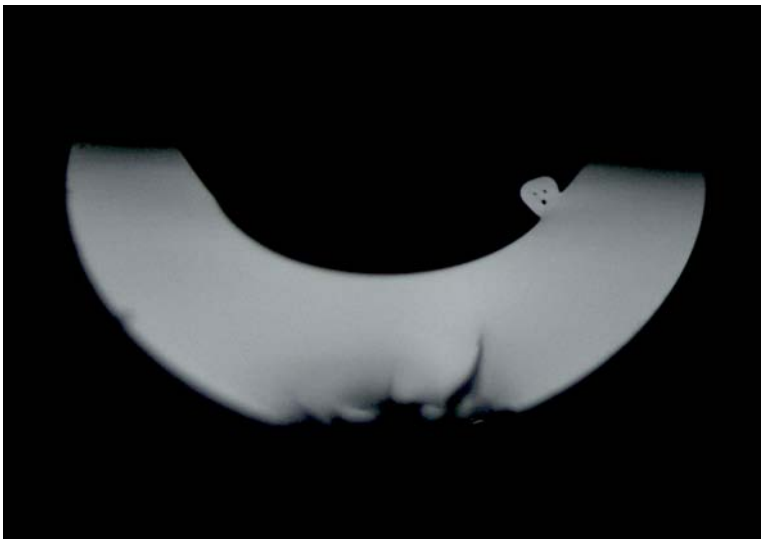

FIGURE 4.11: Microscope image of the first lidded wagon-wheel trial F6b. Using a jacket tube with an extruded slot that ran the length of the tube, and a diamond-doped wagon-wheel cane piece (from P6).

4.3.3 T6c tube with cut slot

The first lidded trial, F6b (see Section 4.3.2), showed that the cladding slot opened out due to the glass surface tension. To prevent this from happening, the cladding tube for the second lidded fibre, F6c (see Section 4.3.4), was designed to start as a standard wagon-wheel tube and gradually introduce the slot feature. This was done to allow the cane section to fuse to the cladding tube all the way around the circumference before the slot appeared, which could then prevent the slot feature from opening up excessively in the fibre draw process.

To fabricate this half-slot cladding tube (T6c) a standard tube, extruded from undoped tellurite, was partially cut with a glass saw, as shown in Fig. 4.12. The cross-section of this cut section is shown in Fig. 4.13b and the gradual introduction of the slot can be seen in Fig. 4.13a. The tube is uncut on the left side of the image, the cut appears after ~70 mm and gradually deepens until it cuts through to the tube hole.

4.3.4 F6c lidded wagon-wheel fibre

An ND-doped wagon-wheel cane piece, from preform P6, was inserted into the slotted cladding tube T6c and was drawn down, under active inflation of the cane (see Section 4.1), starting from the uncut section of the tube to help seal the core and cladding

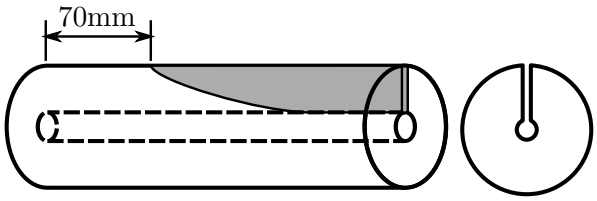

FIGURE 4.12: Schematic showing the cut made in the cladding tube to create the slot needed for fabrication of the lidded wagon-wheel fibre F6c.

(A) Side, showing limited slot (B) Cross-section

FIGURE 4.13: Tube preform T6c after a thin slot has been cut. (a) Preform begins as a standard uncut tube (left side of image) and the slot is gradually introduced along the preform length until it cuts through into the tube hole. (b) Cross-section of preform.

pieces. Pressure was gradually increased in the cane section to obtain cane-tube fusion. The fibre draw underwent several stages as the slot gradually appeared and opened (the evolution can be seen in Fig. 4.14). The end result is a wagon-wheel fibre with an area of open access to the core, apart from a very thin ($< 1\,\mu m$ from SEM images — see Fig. 4.17b) lid section of glass.

4.3.5 Confocal imaging of lidded wagon-wheel

Confocal imaging scans through the fibre cross-section were used to compare the lidded wagon-wheel structure to the standard wagon-wheel. Figure 4.15 shows SEM cross-section images of a standard wagon-wheel fibre and two sections of the lidded wagon-wheel fibre, with labels defining the nomenclature used in this section in Fig. 4.15b.

The resulting confocal images (see Fig. 4.16 for schematic diagrams of the confocal scan directions used) are shown in Fig. 4.17 and were obtained by traversing the fibre towards the lens (moving the lens focus into the sample with the pump beam incident from the side of the fibre, see Fig. 4.16b) rather than the previous endface scanning (Fig. 4.16a).

The confocal setup was limited to a two-dimensional scan and so the planned fibre characterisation involved scanning down the length of the core from the side of the fibre to find suitable NV emitters. This would allow scanning of $100\,\mu m$ of fibre core in one scan, but the focal depth would need to be set for each scan and the core would need to be imaged through the side of the fibre.

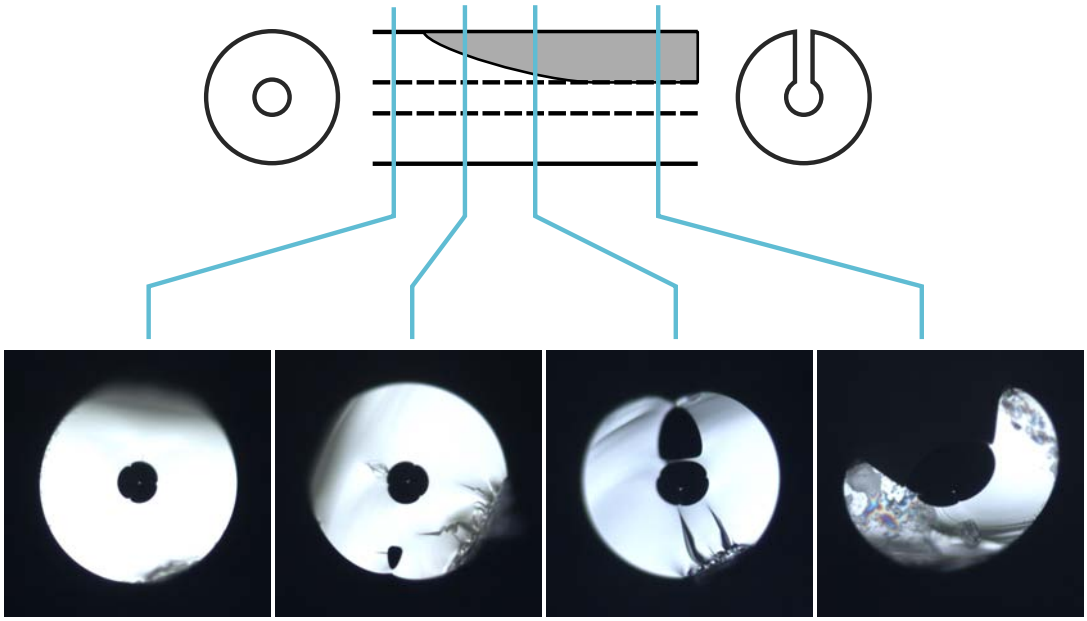

FIGURE 4.14: Series of images showing the evolution of the fibre draw for the lidded wagon-wheel fibre F6c. The fibre draw begins with the uncut section of the preform tube (left). Above these images is a schematic showing the approximate region of tube T6c that corresponds to each fibre cross-section.

The cross-sectional side scan (Fig. 4.16b) was used to see if there would be imaging distortions associated with side scanning and whether the severity of the distortion would prevent imaging of the core region. It also gave the position at which the core would be in focus so that the proposed length scans of the fibre would be of the correct depth 'slice' to see the core — it is difficult, and time-consuming, to find the core region, with a size of less than 2 µm, by slow (up to 15 min) longitudinal scans of varying depth (i.e. scanning through 30 µm of material in 2 µm steps). This technique confirmed that the core was visible in the fully exposed lidded fibre and allowed fast set up of the depth for scanning along the fibre length.

These cross-sectional side scans (Fig. 4.17) show that thick cladding glass sections distort the core image excessively. The full (80 µm) cladding of the standard wagon-wheel fibre shows some little detail of the hole region around the core (see Fig. 4.17a), but the struts and core cannot be resolved. Interestingly, even the relatively thin glass of the closed slot (Fig. 4.17b) of the lidded wagon-wheel distorts the imaging enough to hide the core geometry (even the lid section is not visible on this confocal scan). Note that the beam is incident from the top of the image in all of these confocal scans. The lidded wagon-wheel fibre pieces were aligned on a microscope before confocal imaging such that the 'lidded' hole section was front-on to the pump beam, so that the system was imaging through the thinnest glass section.

As seen in Fig. 4.17b, the core is not visible when the slot is partially closed (imaging

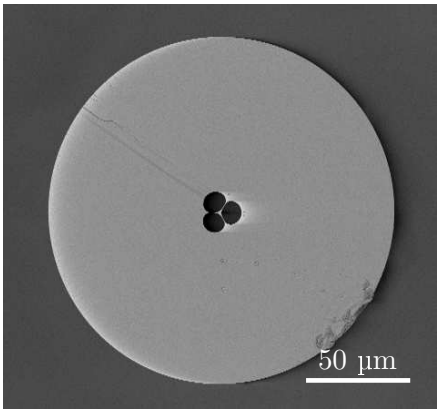

(A) Standard wagon-wheel

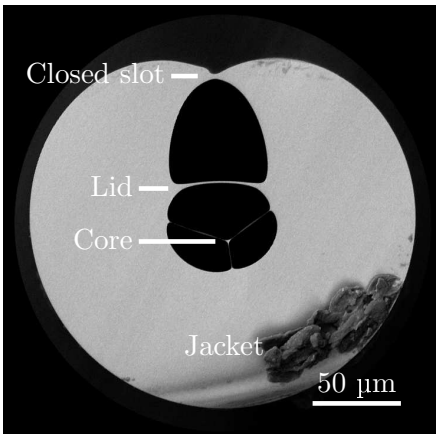

(B) F6c closed lidded wagon-wheel

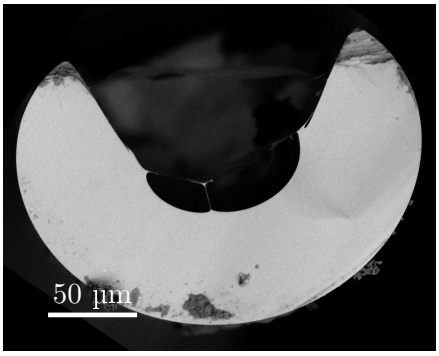

(C) F6c fully exposed lidded wagon-wheel

FIGURE 4.15: SEM images of a standard wagon-wheel fibre and two sections of F6c lidded wagon-wheel fibre, from different times in the draw process. (a) Standard wagon-wheel, (b) F6c lidded wagon-wheel with closed slot, and (c) F6c lidded wagon-wheel with fully exposed lid. Image (b) has also been labelled with the nomenclature used here to describe the fibre geometry.

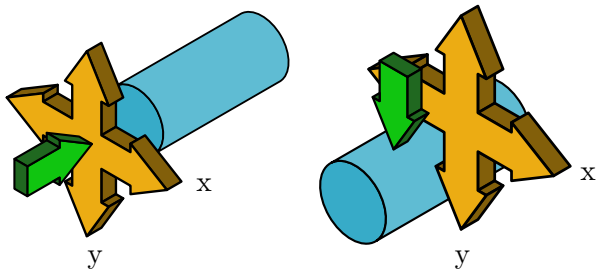

(A) Endface (B) Side scan

FIGURE 4.16: Schematic images showing the confocal raster scan axes (orange arrows) and the direction of the incident laser pump beam (green arrow) relative to the fibre geometry (blue). (a) The standard endface scan of the fibre, as used in previous images. (b) Side scan of the cross-section.

through ∼5 µm of glass) and only becomes visible when the cladding glass is almost completely removed (only a thin lid of <1 µm, see Fig. 4.17c). In this second lidded fibre piece (Fig. 4.17c) the cladding slot had opened completely and only a thin section remained (originating from the core cane section, see Fig. 4.8). This section is visible in the confocal image sample, but is not seen clearly in the SEM as the thin glass is fragile and had broken for the particular fibre sample used for the SEM imaging.

The cross-sectional side scans showed that the core was visible for the open lidded wagon-wheel fibre (as pictured in Fig. 4.17c), and so this fibre was then scanned along the length to look for single colour centre emitters. Cross-sectional side scans were used to find the depth of the core, and this was set as the depth position of the length scans. The 100 µm scans were generally performed 3-5 times in an area of the fibre, translating by ∼90 µm each time to leave a 10 µm overlap region between scans. No single emitters were seen while scanning several different pieces of the open lidded fibre.

4.4 Conclusion

Successful fabrication of a structured fibre from ND doped tellurite glass is a good step towards a fibre-based single photon source, using a high index contrast fibre structure for efficient photon collection.

Confocal imaging of the wagon-wheel fibre endface showed strong background fluorescence from the core region, resulting from strong pump light guidance and efficient capture of the glass fluorescence, which would make end pumping of the NV centres difficult without a large amount of filtering. A possible solution to this problem may be side pumping of the colour centres, and this was investigated by side scanning the

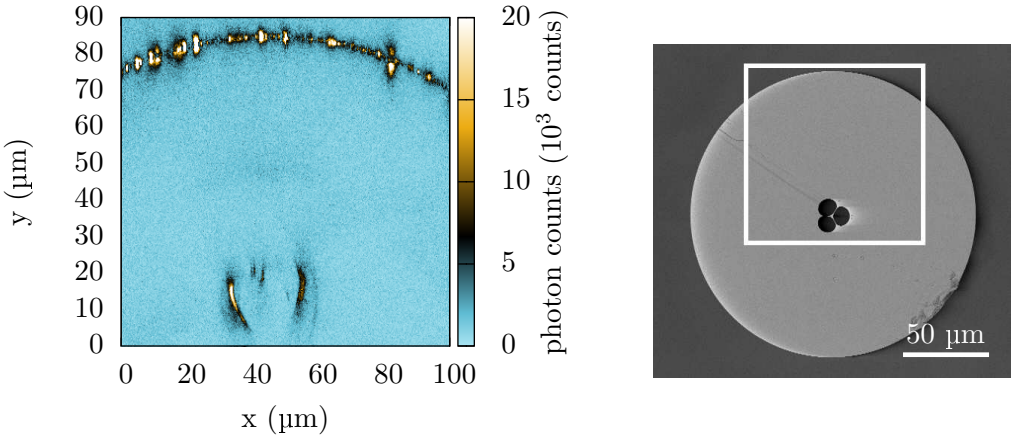

(A) Standard wagon-wheel

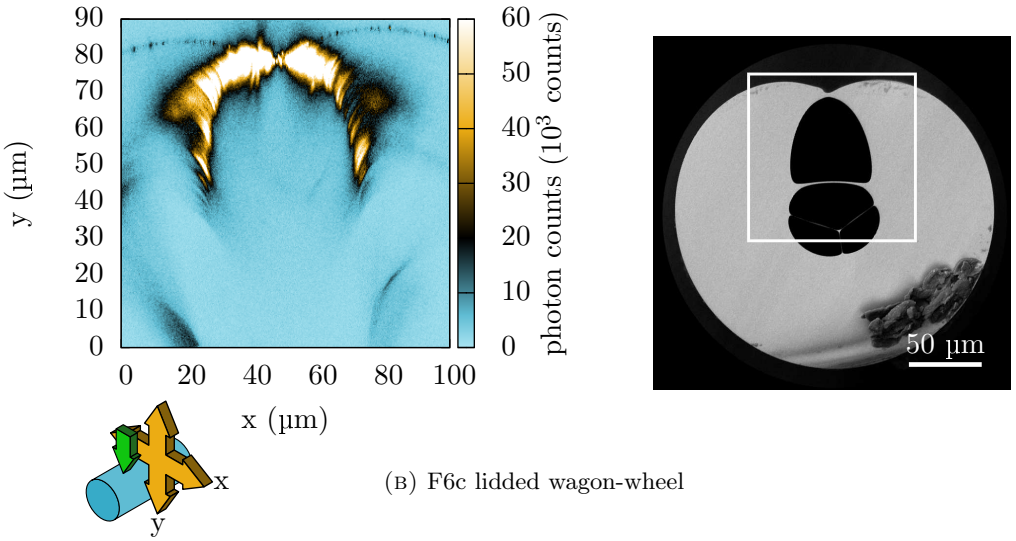

(B) F6c lidded wagon-wheel

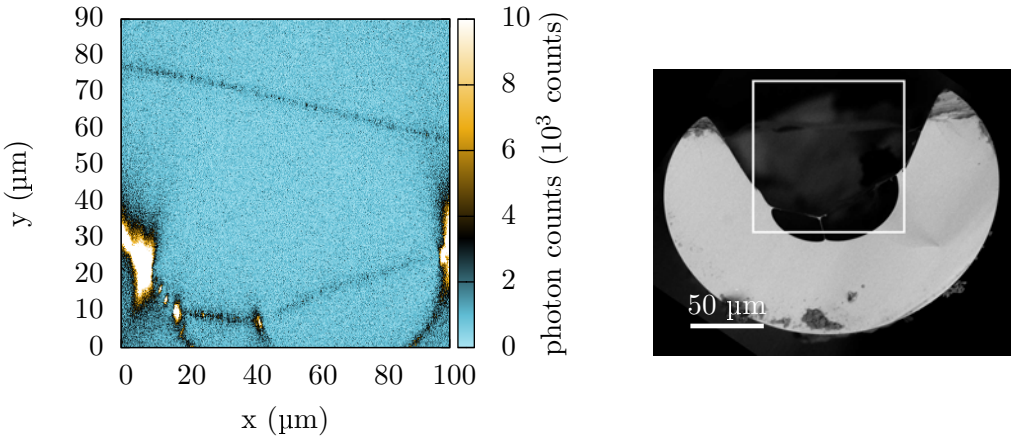

(C) F6c lidded wagon-wheel

FIGURE 4.17: Comparison between the confocal images obtained for standard and lidded wagon-wheel fibres. The confocal scans are slices through the cross-section of the fibre to show the effect of the cladding glass on the core image, along with the corresponding SEM image showing a representation of the actual cross-section. Significant distortion occurs for a relatively thin glass section. The confocal pump beam was incident from the top of the scans. The SEM images also show the approximate region of the corresponding confocal scan using a white rectangle.

wagon-wheel fibre using the confocal system. These side images showed large distortions due to the thick fibre cladding glass, and so an exposed core design, described as a 'lidded' wagon-wheel, was used to fabricate the later fibres. The fabricated lidded wagon-wheel fibre showed a large decrease in the previously seen distortions with the confocal side imaging. No embedded ND was seen in the fabricated fibres, but the core was visible though the remaining thin lid.

Future work would involve showing colour centre emission coupled into the fibre modes, which might be more readily performed using a lidded wagon-wheel doped with irradiated ND. Most of the irradiated diamond would show NV colour centre emission, in contrast to the unirradiated ND (where many of the nanoparticles do not contain NV centres), and many of the NDs would be much brighter (containing many NV). This would reduce the probability of finding a single emitter, but experimentally verifying colour centre emission in the fibre core, and collection of this emission into the fibre guided modes, would be made easier using irradiated diamond. Once NV emission coupling was verified, the next step would be to show single photon coupling (most likely doping with different ND, such as the original unirradiated diamond, for a higher probability of single emitters).

Although single emission was not observed in the structured fibre, the results presented in this chapter have shown that fabrication of a diamond doped wagon-wheel fibre is feasible and that side pumping of the NV centres can be used, employing an exposed core fibre design, with the aim of decreasing transmitted pump laser and background fluorescence light.

5

Conclusion

In this work, diamond nanocrystals were successfully embedded within an optical fibre. By using tellurite, ND was incorporated within the glass at a low processing temperature, reducing or avoiding oxidation of the diamond, and characterisation of the hybrid diamond-glass showed that the ND survived the glass melting procedure. The successful fabrication of a suspended core MOF from the diamond-tellurite glass demonstrated that the material was able to be used for complex fibre structures. Development of a general theoretical model describing an emitter in the vicinity of an optical fibre allowed calculations of emitter-fibre coupling. The modelling also theoretically demonstrated the creation of a self-aligned cavity, by the coupling of the emitter to fibre WGMs.

A hybrid diamond-glass material should be able to leverage all of the well-developed fabrication techniques available for soft glasses, and here it was demonstrated for the extrusion method. The embedded NV colour centres were imaged using a confocal microscope, and the collected signal could be directed to a HBT measurement for characterisation of single photon emission, or to a spectrometer for PL spectrum measurements. Single photon emission was seen from the embedded NV both before and after fibre drawing and spectral measurements confirmed that the emitters were NV centres. A MOF, using a suspended core fibre design, was successfully fabricated and the creation of such a complex structure showcases the degree of flexibility available from the hybrid material. The MOF design allows a high NA, from a large core-cladding refractive index contrast (due to the use of air holes), and is expected to lead to a high degree of coupling of emission from the diamond colour centres to the optical fibre guided modes. Strong coupling to the embedded NV centre would be advantageous for fabrication of a diamond-based fibre single photon source or magnetometer with remote fibre readout, for instance. The difficulties involved in fabricating optical structures in diamond makes the hybrid diamond-glass material an attractive option, with a large range of fabrication methods and flexibility in the device structure.

Embedding ND within tellurite showed two unforeseen benefits. There was a measured improvement in the NV^- to NV^0 ratio, an important parameter for applications using NV^-. Secondly, the absence of a graphite Raman signal from the hybrid diamond-tellurite glass indicated that there was preferential oxidation of the graphitic outer layer of the ND during inclusion.

The theoretical model developed here incorporated the effects of the optical fibre on the emission properties of the emitter, including total emission power and radiation pattern. The expected capture fraction, that is the fraction of total dipole emission coupled into the fibre guided modes, was calculated, and showed coupling of up to 81% for a tellurite core in an air cladding. Several different FDTD calculations verified the results of the model. Purcell effects, from proximity to the core-cladding interface, were also explored and showed that the total emitted power can vary dramatically from that of the same emitter in a bulk, homogeneous material. The Purcell effect caused by the fibre geometry also affected the calculated capture fraction. The change to capture fraction was demonstrated by comparing the capture fraction obtained with the model derived here to that calculated by assuming the total emitted power of an emitter in a bulk material. Calculation of the Purcell effect involved the use of fibre radiation modes, and this led to the interesting result of seeing WGM resonances in the radiated power emission. Total power at the resonances was shown to be as much as 400 times that of emission in a bulk material.

WGM resonances from the circular step-index fibre geometry were seen in the fibre radiation mode modelling calculations. The fibre geometry is longitudinally and rotationally symmetric and so the WGM positions are not predetermined by the structure. Placing the dipole in the vicinity of the fibre defines the WGM and realises a self-aligned cavity. The resonances were identified as WGMs by the electric field distribution of the coupled emission and a strong correlation of the resonance peaks to the positions of pure WGM modal solutions. The electric field distribution was confirmed using FDTD modelling. The WGMs did not, however, necessarily show the degradation in quality factor expected by the lack of confinement along the fibre length. Some WGMs showed almost no leakage from skew rays due to the lack of confinement, with Q-factors approaching that expected from modelling the pure WGM solution. For example, the Q-factor of the TE(29,1) mode was calculated to be 1.3×10^9. The WGMs also showed a high sensitivity to the cladding refractive index.

While an optical fibre with embedded diamond has been demonstrated, there are many obstacles remaining for the realisation of a single photon source based on this technology. Single photon emission into the fibre guided modes has not yet been observed and so demonstrating emission capture would likely be the next step towards a fibre-coupled

single photon device, possibly by fabrication of a MOF using irradiated ND. Experimental demonstration of coupled emission would also allow linking of experimental data to the capture fraction modelling shown here.

Many interesting experiments could follow once diamond emission has been verified in a structured fibre. Applying the hybrid diamond-tellurite material to the magnetometry applications of the NV colour centre would be of interest, and could result in fibre-coupled nano-magnetometry or the demonstration of unusual effects due to the embedding. The fibre fabrication shown here is only a beginning to the variety of possible photonic structures able to be fabricated from a diamond-tellurite material. Bragg gratings or different cross-sectional designs are possible, allowing investigation into the emitter behaviour with the 1-dimensional system of the fibre (compared to, for example, current research using 2-D photonic crystals). Introducing a cavity, such as by writing Bragg gratings around the colour centre, could be investigated for enhancing single photon emission behaviour or magnetometry performance.

For the theoretical work, as mentioned above, marrying the predicted emission behaviour with experimental data would be an exciting next step in this body of work, tying the main loose thread of the single emitter modelling. There are also a wide range of investigations using the multiple dipole emitter model and it could, for example, be applied to calculations of particle detection (looking at differences when placing a second dipole) or the effect of multiple single emitters on the behaviour of a fibre single photon source. Experimentally investigating the predictions of the WGM modelling, although challenging, could also lead to interesting results. There was also little chance to delve much below the surface of the WGM modelling and there is the opportunity for a much larger exploration in this area.

The research presented here has shown that a combined diamond-glass material is possible, and could pave the way towards an integrated diamond photonic platform using embedded diamond nanocrystals.

A

Derivations

A.1 Step-index guided mode fields

For a derivation of the step-index guided modes, see Refs. [63] and [96]. The guided mode field expressions [96] are shown below for completeness.

For the following step-index guided mode expressions

$$u = r_{\text{core}}(k_0^2 n_{\text{core}}^2 - \beta^2)^{1/2}, \tag{A.1}$$

$$w = r_{\text{core}}(\beta^2 - k_0^2 n_{\text{clad}}^2)^{1/2}, \tag{A.2}$$

$$s = \frac{n\left(\frac{1}{u^2} + \frac{1}{w^2}\right)}{\left[\frac{J_n'(u)}{uJ_n(u)} + \frac{K_n'(w)}{wK_n(w)}\right]}, \tag{A.3}$$

n is an integer, ψ is the phase, $s_0 = \frac{\beta^2}{k_0^2 n_{\text{clad}}^2} s$, and $s_1 = \frac{\beta^2}{k_0^2 n_{\text{core}}^2} s$.

A.1.1 Hybrid (HE) modes

$$E_r = \begin{cases} -iA\beta\frac{r_{\text{core}}}{u}\left[\frac{1-s}{2}J_{n-1}(\frac{ur}{r_{\text{core}}}) - \frac{1+s}{2}J_{n+1}(\frac{ur}{r_{\text{core}}})\right]\cos(n\theta+\psi) & 0 \le r \le r_{\text{core}} \\ -iA\beta\frac{r_{\text{core}}J_n(u)}{wK_n(w)}\left[\frac{1-s}{2}K_{n-1}(\frac{wr}{r_{\text{core}}}) + \frac{1+s}{2}K_{n+1}(\frac{wr}{r_{\text{core}}})\right]\cos(n\theta+\psi) & r > r_{\text{core}}. \end{cases} \tag{A.4}$$

$$E_\theta = \begin{cases} iA\beta\frac{r_{\text{core}}}{u}\left[\frac{1-s}{2}J_{n-1}(\frac{ur}{r_{\text{core}}}) + \frac{1+s}{2}J_{n+1}(\frac{ur}{r_{\text{core}}})\right]\sin(n\theta+\psi) & 0 \le r \le r_{\text{core}} \\ iA\beta\frac{r_{\text{core}}J_n(u)}{wK_n(w)}\left[\frac{1-s}{2}K_{n-1}(\frac{wr}{r_{\text{core}}}) - \frac{1+s}{2}K_{n+1}(\frac{wr}{r_{\text{core}}})\right]\sin(n\theta+\psi) & r > r_{\text{core}}. \end{cases} \tag{A.5}$$

$$E_z = \begin{cases} AJ_n(\frac{ur}{r_{\text{core}}})\cos(n\theta+\psi) & 0 \le r \le r_{\text{core}} \\ A\frac{J_n(u)}{K_n(w)}K_n(\frac{wr}{r_{\text{core}}})\cos(n\theta+\psi) & r > r_{\text{core}}. \end{cases} \tag{A.6}$$

$$H_r = \begin{cases} -iA\omega\epsilon_0 n_{\text{core}}^2 \frac{r_{\text{core}}}{u}\left[\frac{1-s_1}{2}J_{n-1}(\frac{ur}{r_{\text{core}}}) + \frac{1+s_1}{2}J_{n+1}(\frac{ur}{r_{\text{core}}})\right]\sin(n\theta+\psi) & 0 \le r \le r_{\text{core}} \\ -iA\omega\epsilon_0 n_{\text{clad}}^2 \frac{r_{\text{core}}J_n(u)}{wK_n(w)}\left[\frac{1-s_0}{2}K_{n-1}(\frac{wr}{r_{\text{core}}}) - \frac{1+s_0}{2}K_{n+1}(\frac{wr}{r_{\text{core}}})\right]\sin(n\theta+\psi) & r > r_{\text{core}}. \end{cases} \tag{A.7}$$

$$H_\theta = \begin{cases} -iA\omega\epsilon_0 n_{\text{core}}^2 \frac{r_{\text{core}}}{u}\left[\frac{1-s_1}{2}J_{n-1}(\frac{ur}{r_{\text{core}}}) - \frac{1+s_1}{2}J_{n+1}(\frac{ur}{r_{\text{core}}})\right]\cos(n\theta+\psi) & 0 \le r \le r_{\text{core}} \\ -iA\omega\epsilon_0 n_{\text{clad}}^2 \frac{r_{\text{core}}J_n(u)}{wK_n(w)}\left[\frac{1-s_0}{2}K_{n-1}(\frac{wr}{r_{\text{core}}}) + \frac{1+s_0}{2}K_{n+1}(\frac{wr}{r_{\text{core}}})\right]\cos(n\theta+\psi) & r > r_{\text{core}}. \end{cases} \tag{A.8}$$

$$H_z = \begin{cases} -A\frac{\beta}{\omega\mu_0}sJ_n(\frac{ur}{r_{\text{core}}})\sin(n\theta+\psi) & 0 \le r \le r_{\text{core}} \\ -A\frac{\beta}{\omega\mu_0}s\frac{J_n(u)}{K_n(w)}K_n(\frac{wr}{r_{\text{core}}})\sin(n\theta+\psi) & r > r_{\text{core}}. \end{cases} \tag{A.9}$$

A.1.2 Transverse electric (TE) modes

$$E_r = E_z = H_\theta = 0. \tag{A.10}$$

$$E_\theta = \begin{cases} -i\omega\mu_0\frac{r_{\text{core}}}{u}AJ_1(\frac{ur}{r_{\text{core}}}) & 0 \le r \le r_{\text{core}} \\ i\omega\mu_0\frac{r_{\text{core}}}{w}\frac{J_0(u)}{K_0(w)}AK_1(\frac{wr}{r_{\text{core}}}) & r > r_{\text{core}}. \end{cases} \tag{A.11}$$

$$H_r = \begin{cases} i\beta\frac{r_{\text{core}}}{u}AJ_1(\frac{ur}{r_{\text{core}}}) & 0 \le r \le r_{\text{core}} \\ -i\beta\frac{r_{\text{core}}}{w}\frac{J_0(u)}{K_0(w)}AK_1(\frac{wr}{r_{\text{core}}}) & r > r_{\text{core}}. \end{cases} \tag{A.12}$$

$$H_z = \begin{cases} AJ_0(\frac{ur}{r_{\text{core}}}) & 0 \le r \le r_{\text{core}} \\ \frac{J_0(u)}{K_0(w)}AK_0(\frac{wr}{r_{\text{core}}}) & r > r_{\text{core}}. \end{cases} \tag{A.13}$$

A.1.3 Transverse magnetic (TM) modes

$$E_\theta = H_r = H_z = 0. \tag{A.14}$$

$$E_r = \begin{cases} i\beta\frac{r_{\text{core}}}{u}AJ_1(\frac{ur}{r_{\text{core}}}) & 0 \le r \le r_{\text{core}} \\ -i\beta\frac{r_{\text{core}}}{w}\frac{J_0(u)}{K_0(w)}AK_1(\frac{wr}{r_{\text{core}}}) & r > r_{\text{core}}. \end{cases} \tag{A.15}$$

$$E_z = \begin{cases} AJ_0(\frac{ur}{r_{\text{core}}}) & 0 \le r \le r_{\text{core}} \\ \frac{J_0(u)}{K_0(w)}AK_0(\frac{wr}{r_{\text{core}}}) & r > r_{\text{core}}. \end{cases} \tag{A.16}$$

$$H_\theta = \begin{cases} i\omega\epsilon_0 n_{\text{core}}^2 AJ_1(\frac{ur}{r_{\text{core}}}) & 0 \le r \le r_{\text{core}} \\ -i\omega\epsilon_0 n_{\text{core}}^2\frac{r_{\text{core}}}{w}\frac{J_0(u)}{K_0(w)}AK_1(\frac{wr}{r_{\text{core}}}) & r > r_{\text{core}}. \end{cases} \tag{A.17}$$

A.2 Step-index radiation mode fields

The radiation modes are of the form [63]:

$$e_z = \begin{cases} a_\nu J_\nu(UR) f_\nu(\theta) & 0 \le r < r_{\text{core}} \\ \left[c_\nu^f J_\nu(QR) + c_\nu^s H_\nu^{(1)}(QR)\right] f_\nu(\theta) & r_{\text{core}} \le r < \infty \end{cases} \tag{A.18}$$

$$h_z = \begin{cases} b_\nu J_\nu(UR) g_\nu(\theta) & 0 \le r < r_{\text{core}} \\ \left[d_\nu^f J_\nu(QR) + d_\nu^s H_\nu^{(1)}(QR)\right] g_\nu(\theta) & r_{\text{core}} \le r < \infty \end{cases} \tag{A.19}$$

$$f_\nu(\theta) = \begin{cases} \cos(\nu\theta) & \text{even modes} \\ \sin(\nu\theta) & \text{odd modes} \end{cases} \tag{A.20}$$

$$g_\nu(\theta) = \begin{cases} -\sin(\nu\theta) & \text{even modes} \\ \cos(\nu\theta) & \text{odd modes} \end{cases} \tag{A.21}$$

where ν is an azimuthal mode index, a_ν, b_ν, c_ν^f, c_ν^s, d_ν^f and d_ν^s are constants found by applying the continuity conditions at the core-cladding interface, $U = r_{\text{core}}(k_0^2 n_{\text{core}}^2 - \beta^2)^{1/2}$, $Q = r_{\text{core}}(k_0^2 n_{\text{clad}}^2 - \beta^2)^{1/2}$, $R = r/r_{\text{core}}$, and the superscripts f and s denote the 'free-space' and scattering terms, respectively. The radial and azimuthal field expressions can be calculated from $\mathbf{E}_z$ and $\mathbf{H}_z$ by

$$e_r = \frac{i}{k_0^2 n^2 - \beta^2}\left[\beta\frac{\partial e_z}{\partial r} + \left(\frac{\mu_0}{\epsilon_0}\right)^{\frac{1}{2}}\frac{k_0}{r}\frac{\partial h_z}{\partial \theta}\right] \tag{A.22}$$

$$e_\theta = \frac{i}{k_0^2 n^2 - \beta^2}\left[\frac{\beta}{r}\frac{\partial e_z}{\partial \theta} - \left(\frac{\mu_0}{\epsilon_0}\right)^{\frac{1}{2}} k_0 \frac{\partial h_z}{\partial r}\right] \tag{A.23}$$

Substituting the expressions for e_z and h_z, Eqs. (A.18) and (A.19), into the above equations, Eqs. (A.22) and (A.23), gives:

For $0 \leq r < r_{\text{core}}$

$$e_r = \frac{f_\nu(\theta)}{k_0^2 n_{\text{core}}^2 - \beta^2}\frac{iU}{2r_{\text{core}}}\left\{\beta a_\nu \left[J_{\nu-1}(UR) - J_{\nu+1}(UR)\right] - \left(\frac{\mu_0}{\epsilon_0}\right)^{\frac{1}{2}} k_0 b_\nu \left[J_{\nu-1}(UR) + J_{\nu+1}(UR)\right]\right\} \tag{A.24}$$

$$e_\theta = \frac{g_\nu(\phi)}{k_0^2 n_{\text{core}}^2 - \beta^2}\frac{iU}{2r_{\text{core}}}\left\{\beta a_\nu \left[J_{\nu-1}(UR) + J_{\nu+1}(UR)\right] - \left(\frac{\mu_0}{\epsilon_0}\right)^{\frac{1}{2}} k_0 b_\nu \left[J_{\nu-1}(UR) - J_{\nu+1}(UR)\right]\right\} \tag{A.25}$$

For $r_{\text{core}} \leq r < \infty$

$$e_r = \frac{f_\nu(\theta)}{k_0^2 n_{\text{clad}}^2 - \beta^2}\frac{iQ}{2r_{\text{core}}}\left(\beta\left\{c_\nu^f\left[J_{\nu-1}(QR) - J_{\nu+1}(QR)\right] + c_\nu^s\left[H_{\nu-1}^{(1)}(QR) - H_{\nu+1}^{(1)}(QR)\right]\right\}\right.$$
$$\left. -k_0\left(\frac{\mu_0}{\epsilon_0}\right)^{\frac{1}{2}}\left\{d_\nu^f\left[J_{\nu-1}(QR) + J_{\nu+1}(QR)\right] + d_\nu^s\left[H_{\nu-1}^{(1)}(QR) + H_{\nu+1}^{(1)}(QR)\right]\right\}\right) \tag{A.26}$$

$$e_\theta = \frac{g_\nu(\phi)}{k_0^2 n_{\text{clad}}^2 - \beta^2}\frac{iQ}{2r_{\text{core}}}\left(\beta\left\{c_\nu^f\left[J_{\nu-1}(QR) + J_{\nu+1}(QR)\right] + c_\nu^s\left[H_{\nu-1}^{(1)}(QR) + H_{\nu+1}^{(1)}(QR)\right]\right\}\right.$$
$$\left. -k_0\left(\frac{\mu_0}{\epsilon_0}\right)^{\frac{1}{2}}\left\{d_\nu^f\left[J_{\nu-1}(QR) - J_{\nu+1}(QR)\right] + d_\nu^s\left[H_{\nu-1}^{(1)}(QR) - H_{\nu+1}^{(1)}(QR)\right]\right\}\right) \tag{A.27}$$

The radiation mode coefficients (in Ref. [63] Table 25-3, page 525) appearing in Eqs. (A.18) and (A.19) are shown here in Table A.1 for completeness. These coefficients are calculated by applying the boundary conditions to the electric and magnetic field expressions at the fiber core-cladding interface, i.e. e_z, e_θ, h_z, and h_θ are continuous at the interface.

TABLE A.1: Coefficients appearing in Eqs. (A.18) and (A.19) for 'TM-like' (ITM) and 'TE-like' (ITE) radiation modes. These correspond to the pure TM and TE modes in the 'free-space' terms that are subsequently altered by the perturbation of the waveguide. From [63].

	ITE modes	ITM modes
a_ν	$-\frac{4}{\pi}\frac{\beta}{k_0 n_{\text{core}}^2}\frac{\nu}{k_0 r_{\text{core}}}\frac{V^2}{U^2Q^3}\frac{1}{J_\nu(U)H_\nu^{(1)}(Q)M_\nu}$	$-\frac{4}{\pi}\frac{n_{\text{clad}}^2}{n_{\text{core}}^2}\frac{1}{\beta r_{\text{core}}Q}\frac{F_\nu}{J_\nu(U)H_\nu^{(1)}(Q)M_\nu}$
b_ν	$-\frac{4}{\pi}\left(\frac{\epsilon_0}{\mu_0}\right)^{\frac{1}{2}}\frac{1}{Qkr_{\text{core}}}\frac{G_\nu}{J_\nu(U)H_\nu^{(1)}(Q)M_\nu}$	$-\frac{4}{\pi}\frac{n_{\text{clad}}^2}{n_{\text{core}}^2}\left(\frac{\epsilon_0}{\mu_0}\right)^{\frac{1}{2}}\frac{\nu}{kr_{\text{core}}}\frac{V^2}{U^2Q^3}\frac{1}{J_\nu(U)H_\nu^{(1)}(Q)M_\nu}$
c_ν^f	0	$2i\frac{Q}{\beta r_{\text{core}}}$
c_ν^s	$-\frac{4}{\pi}\frac{\beta}{k_0 n_{\text{core}}^2}\frac{\nu}{kr_{\text{core}}}\frac{V^2}{U^2Q^3}\frac{1}{\left\{H_\nu^{(1)}(Q)\right\}^2 M_\nu}$	$-2i\frac{Q}{\beta r_{\text{core}}}\frac{J_\nu(Q)}{H_\nu^{(1)}(Q)}\frac{A_\nu}{M_\nu}$
d_ν^f	$2i\left(\frac{\epsilon_0}{\mu_0}\right)^{\frac{1}{2}}\frac{Q}{r_{\text{core}}k_0}$	0
d_ν^s	$-2i\left(\frac{\epsilon_0}{\mu_0}\right)^{\frac{1}{2}}\frac{Q}{r_{\text{core}}k_0}\frac{J_\nu(Q)}{H_\nu^{(1)}(Q)}\frac{B_\nu}{M_\nu}$	$-\frac{4}{\pi}\frac{n_{\text{clad}}^2}{n_{\text{core}}^2}\left(\frac{\epsilon_0}{\mu_0}\right)^{\frac{1}{2}}\frac{\nu}{r_{\text{core}}k_0}\frac{V^2}{U^2Q^3}\frac{1}{\left\{H_\nu^{(1)}(Q)\right\}^2 M_\nu}$
N_j	$\frac{2\pi r_{\text{core}}^2}{Q}\left(\frac{\epsilon_0}{\mu_0}\right)^{\frac{1}{2}}\frac{\beta}{k_0}\times\begin{cases}1 & \text{for } \nu>0\\ 2 & \text{for } \nu=0\end{cases}$	$\frac{2\pi r_{\text{core}}^2}{Q}\left(\frac{\epsilon_0}{\mu_0}\right)^{\frac{1}{2}}\frac{k_0 n_{\text{clad}}^2}{\beta}\times\begin{cases}1 & \text{for } \nu>0\\ 2 & \text{for } \nu=0\end{cases}$

$$V^2 = U^2 - Q^2 \tag{A.28}$$

$$F_\nu = \frac{J_\nu'(U)}{UJ_\nu(U)} - \frac{H_\nu^{(1)'}(Q)}{QH_\nu^{(1)}(Q)} \tag{A.29}$$

$$G_\nu = \frac{J_\nu'(U)}{UJ_\nu(U)} - \frac{n_{\text{clad}}^2}{n_{\text{core}}^2}\frac{H_\nu^{(1)'}(Q)}{QH_\nu^{(1)}(Q)} \tag{A.30}$$

$$A_\nu = M_\nu - \frac{2i}{\pi}\frac{n_{\text{clad}}^2}{n_{\text{core}}^2}\frac{F_\nu}{Q^2J_\nu(Q)H_\nu^{(1)}(Q)} \tag{A.31}$$

$$B_\nu = M_\nu - \frac{2i}{\pi}\frac{G_\nu}{Q^2J_\nu(Q)H_\nu^{(1)}(Q)} \tag{A.32}$$

$$M_\nu = \left(\frac{\nu\beta}{kn_{\text{core}}}\right)^2\left(\frac{V}{UQ}\right)^4 - F_\nu G_\nu \tag{A.33}$$

A.3 Single emitter coupling to step-index fibre modes

We model the single emitter as a dipole at position $\mathbf{r} = \mathbf{r_0}$, oscillating with frequency ω_f and having a dipole moment $\mathbf{p} = \mathbf{p}_0 e^{-i\omega_f t}$. The polarisation density, $\mathbf{P}$, associated with this dipole is

$$\mathbf{P} = \sum_{i=1}^{N} \mathbf{p}_i \delta(\mathbf{r} - \mathbf{r}_i) \tag{A.34}$$

$$\mathbf{P} = \mathbf{p}_0 e^{-i\omega_f t} \delta(\mathbf{r} - \mathbf{r_0}) \tag{A.35}$$

And the current density, $\mathbf{J}$, is

$$\mathbf{J} = \frac{\partial \mathbf{P}}{\partial t} = -i\omega_f \, \mathbf{p}_0 e^{-i\omega_f t} \delta(\mathbf{r} - \mathbf{r_0}) \tag{A.36}$$

We now use the reciprocity theorem as shown in Ref. [63],

$$\frac{\partial}{\partial z} \int\limits_{A_\infty} \mathbf{F}_c \cdot \hat{z} \; \mathrm{d}A = \int\limits_{A_\infty} \nabla \cdot \mathbf{F}_c \; \mathrm{d}A \tag{A.37}$$

with

$$\mathbf{F}_c = \mathbf{E} \times \bar{\mathbf{H}}^* + \bar{\mathbf{E}}^* \times \mathbf{H} \tag{A.38}$$

We take the barred variables to be of a system consisting only of one mode j in the fibre, with no current sources ($\bar{\mathbf{J}} = 0$), and the unbarred variables as a system of all modes of the fibre (forward, backward and radiation) with a current source (the radiating dipole) such that

$$\bar{\mathbf{E}} = \mathbf{e}_j e^{-i\beta_j z} \tag{A.39}$$

$$\bar{\mathbf{H}} = \mathbf{h}_j e^{-i\beta_j z} \tag{A.40}$$

$$\bar{\mathbf{J}} = 0 \tag{A.41}$$

and

$$\mathbf{E} = \sum_k \overbrace{a_k(z)\,\mathbf{e}_k e^{-i\beta_k z}}^{\text{forward propagating}} + \overbrace{a_{-k}(z)\,\mathbf{e}_{-k} e^{i\beta_k z}}^{\text{backward propagating}} + \text{radiation modes} \tag{A.42}$$

$$\mathbf{H} = \sum_k a_k(z)\,\mathbf{h}_k e^{-i\beta_k z} + a_{-k}(z)\,\mathbf{h}_{-k} e^{i\beta_k z} + \text{ radiation modes} \tag{A.43}$$

$$\mathbf{J} = -i\omega_f\,\mathbf{p}_0 e^{-i\omega_f t}\delta(\,\mathbf{r} - \,\mathbf{r_0}) \tag{A.44}$$

Substituting these expressions into to L.H.S. of Equation (A.37) gives

$$\frac{\partial}{\partial z}\int\limits_{A_\infty} \mathbf{F}_c \cdot \hat{z}\ \mathrm{d}A = \frac{\partial}{\partial z}\int\limits_{A_\infty} \left(\mathbf{E} \times \bar{\mathbf{H}}^* \cdot \hat{z} + \bar{\mathbf{E}}^* \times \mathbf{H} \cdot \hat{z}\right)\ \mathrm{d}A \tag{A.45}$$

$$\begin{aligned} = \frac{\partial}{\partial z}\int\limits_{A_\infty} \sum_k \Big\{ &\Big(a_k(z)\,\mathbf{e}_k e^{-i\beta_k z} + a_{-k}(z)\,\mathbf{e}_{-k} e^{i\beta_k z} + \text{rad.}\Big) \times \mathbf{h}_j^* e^{i\beta_j z} \\ &+ \mathbf{e}_j^* e^{i\beta_j z} \times \Big(\mathbf{h}_k e^{-i\beta_k z} + a_{-k}(z)\,\mathbf{h}_{-k} e^{i\beta_k z} + \text{ rad.}\Big)\Big\} \cdot \hat{z}\ \mathrm{d}A \end{aligned} \tag{A.46}$$

Now,

$$\int\limits_{A_\infty} \mathbf{e}_j \times \mathbf{h}_k^* \cdot \hat{z}\ \mathrm{d}A = \int\limits_{A_\infty} \mathbf{e}_j^* \times \mathbf{h}_k \cdot \hat{z}\ \mathrm{d}A = 0 \quad \text{for } j \neq k \tag{A.47}$$

and so

$$\frac{\partial}{\partial z}\int\limits_{A_\infty} \mathbf{F}_c \cdot \hat{z}\ \mathrm{d}A = \frac{\partial}{\partial z} a_j(z) \int\limits_{A_\infty} \left(\mathbf{e}_j e^{-i\beta_j z} \times \mathbf{h}_j^* e^{i\beta_j z} + \mathbf{e}_j^* e^{i\beta_j z} \times \mathbf{h}_j e^{-i\beta_j z}\right) \cdot \hat{z}\ \mathrm{d}A \tag{A.48}$$

$$\frac{\partial}{\partial z}\int\limits_{A_\infty} \mathbf{F}_c \cdot \hat{z}\ \mathrm{d}A = \frac{\partial}{\partial z} 2a_j(z) \int\limits_{A_\infty} \mathbf{e}_j \times \mathbf{h}_j^* \cdot \hat{z}\ \mathrm{d}A \tag{A.49}$$

If we now set

$$N_j = \frac{1}{2}\int\limits_{A_\infty} \mathbf{e}_j \times \mathbf{h}_j^* \cdot \hat{z}\ \mathrm{d}A \tag{A.50}$$

then Equation (A.49) becomes

$$\frac{\partial}{\partial z}\int\limits_{A_\infty} \mathbf{F}_c \cdot \hat{z}\ \mathrm{d}A = 4N_j \frac{\partial a_j(z)}{\partial z} \tag{A.51}$$

Now we take the L.H.S. of Equation (A.37).

$$\begin{aligned}
\int\limits_{A_\infty} \nabla\cdot\mathbf{F}_c\ \mathrm{d}A &= \int\limits_{A_\infty} \nabla\cdot(\mathbf{E}\times\bar{\mathbf{H}}^* + \bar{\mathbf{E}}^*\times\mathbf{H})\ \mathrm{d}A && \text{(A.52)}\\
&= \int\limits_{A_\infty} \nabla\cdot(\mathbf{E}\times\bar{\mathbf{H}}^*) + \nabla\cdot(\bar{\mathbf{E}}^*\times\mathbf{H})\ \mathrm{d}A && \text{(A.53)}\\
&= \int\limits_{A_\infty} \left\{\bar{\mathbf{H}}^*\cdot(\nabla\times\mathbf{E}) - \mathbf{E}\cdot(\nabla\times\bar{\mathbf{H}}^*)\right.\\
&\quad \left. + \mathbf{H}\cdot(\nabla\times\bar{\mathbf{E}}^*) - \bar{\mathbf{E}}^*\cdot(\nabla\times\mathbf{H})\right\}\ \mathrm{d}A && \text{(A.54)}\\
&= \int\limits_{A_\infty} \bar{\mathbf{H}}^*\cdot\left(-\mu\frac{\partial\mathbf{H}}{\partial t}\right) - \mathbf{E}\cdot\left(\bar{\mathbf{J}}^* + \bar{\epsilon}^*\frac{\partial\bar{\mathbf{E}}^*}{\partial t}\right)\\
&\quad + \mathbf{H}\cdot\left(-\bar{\mu}^*\frac{\partial\bar{\mathbf{H}}^*}{\partial t}\right) - \bar{\mathbf{E}}^*\cdot\left(\mathbf{J} + \epsilon\frac{\partial\mathbf{E}}{\partial t}\right)\ \mathrm{d}A && \text{(A.55)}\\
&= \int\limits_{A_\infty} \bar{\mathbf{H}}^*\cdot(-i\omega_f\mu\,\mathbf{H}) - \mathbf{E}\cdot\left(\bar{\mathbf{J}}^* - i\omega_f\bar{\epsilon}^*\,\bar{\mathbf{E}}^*\right)\\
&\quad + \mathbf{H}\cdot\left(i\omega_f\bar{\mu}^*\,\bar{\mathbf{H}}^*\right) - \bar{\mathbf{E}}^*\cdot(\mathbf{J} + i\omega_f\epsilon\,\mathbf{E})\ \mathrm{d}A && \text{(A.56)}
\end{aligned}$$

and finally,

$$\begin{aligned}
\int\limits_{A_\infty} \nabla\cdot\mathbf{F}_c\ \mathrm{d}A = \int\limits_{A_\infty} &-i\omega_f\mu\left(\bar{\mathbf{H}}^*\cdot\mathbf{H}\right) - \mathbf{E}\cdot\bar{\mathbf{J}}^* + i\omega_f\bar{\epsilon}^*\left(\mathbf{E}\cdot\bar{\mathbf{E}}^*\right)\\
&+ i\omega_f\bar{\mu}^*\left(\mathbf{H}\cdot\bar{\mathbf{H}}^*\right) - \bar{\mathbf{E}}^*\cdot\mathbf{J} - i\omega_f\epsilon\left(\bar{\mathbf{E}}^*\cdot\mathbf{E}\right)\ \mathrm{d}A
\end{aligned} \tag{A.57}$$

Evaluating the dot product terms gives

$$\bar{\mathbf{E}}^*\cdot\mathbf{E} = \sum_k \mathbf{e}_j e^{i\beta_j z}\cdot\left\{a_k(z)\,\mathbf{e}_k e^{-i\beta_k z} + a_{-k}(z)\,\mathbf{e}_{-k}e^{i\beta_k z} + \text{rad.}\right\} \tag{A.58}$$

As the modes form an orthogonal basis, the dot product $e_j\cdot e_k = 0$ unless $j = k$. This simplifies the above equation to

$$\bar{\mathbf{E}}^* \cdot \mathbf{E} = \mathbf{e}_j e^{i\beta_j z} \cdot a_j(z)\, \mathbf{e}_j e^{-i\beta_j z} \tag{A.59}$$

$$= a_j(z)(\, \mathbf{e}_j \cdot \mathbf{e}_j) \tag{A.60}$$

$$= \mathbf{E} \cdot \bar{\mathbf{E}}^* \tag{A.61}$$

and similarly for $\mathbf{H}$,

$$\bar{\mathbf{H}}^* \cdot \mathbf{H} = \sum_k \mathbf{h}_j e^{i\beta_j z} \cdot \left\{ a_k(z)\, \mathbf{h}_k e^{-i\beta_k z} + a_{-k}(z)\, \mathbf{h}_{-k} e^{i\beta_k z} + \text{rad.} \right\} \tag{A.62}$$

$$= \mathbf{h}_j e^{i\beta_j z} \cdot a_j(z)\, \mathbf{h}_j e^{-i\beta_j z} \tag{A.63}$$

$$= a_j(z)(\, \mathbf{h}_j \cdot \mathbf{h}_j) \tag{A.64}$$

$$= \mathbf{H} \cdot \bar{\mathbf{H}}^* \tag{A.65}$$

Substituting for these expressions in Equation (A.57) gives

$$\begin{aligned} \int_{A_\infty} \nabla \cdot \mathbf{F}_c \; \mathrm{d}A = \int_{A_\infty} & \left(i\omega_f \bar{\mu}^* - i\omega_f \mu\right) \bar{\mathbf{H}}^* \cdot \mathbf{H} + \left(i\omega_f \bar{\epsilon}^* - i\omega_f \epsilon\right) \mathbf{E} \cdot \bar{\mathbf{E}}^* \\ & - \left(\bar{\mathbf{E}}^* \cdot \mathbf{J} + \mathbf{E} \cdot \bar{\mathbf{J}}^* \right) \; \mathrm{d}A \end{aligned} \tag{A.66}$$

The materials and wavelengths for the barred and unbarred fields are the same, giving $\bar{\epsilon} = \epsilon$. If we now assume that the materials are non-absorbing, such that $\bar{\epsilon}^* = \bar{\epsilon}$, then $\bar{\epsilon}^* = \epsilon$. We also make the assumption that $\bar{\mu}^* = \bar{\mu} = \mu_0$. Equation (A.66) then becomes

$$\int_{A_\infty} \nabla \cdot \mathbf{F}_c \; \mathrm{d}A = \int_{A_\infty} - \left(\bar{\mathbf{E}}^* \cdot \mathbf{J} + \mathbf{E} \cdot \bar{\mathbf{J}}^* \right) \; \mathrm{d}A \tag{A.67}$$

Now, $\bar{\mathbf{J}} = 0$ so

$$\int_{A_\infty} \nabla \cdot \mathbf{F}_c \; \mathrm{d}A = \int_{A_\infty} - \bar{\mathbf{E}}^* \cdot \mathbf{J} \; \mathrm{d}A \tag{A.68}$$

By substituting the expression for $\mathbf{J}$ given by Equation (A.36) into the above equation we obtain

$$\int_{A_\infty} \nabla \cdot \mathbf{F}_c \ \mathrm{d}A = \int_{A_\infty} -\bar{\mathbf{E}}^* \cdot \left\{ -i\omega_f \, \mathbf{p_0} e^{-i\omega_f t} \delta(\mathbf{r} - \mathbf{r_0}) \right\} \ \mathrm{d}A \tag{A.69}$$

We now simplify and rearrange to find an expression for the mode coefficients, a_j.

$$\int_{A_\infty} \nabla \cdot \mathbf{F}_c \ \mathrm{d}A = i\omega_f e^{-i\omega_f t} \int_{A_\infty} (\mathbf{e}_j^* \cdot \mathbf{p}_0) e^{i\beta_j z} \delta(\mathbf{r} - \mathbf{r_0}) \ \mathrm{d}A \tag{A.70}$$

$$4N_j \frac{\partial a_j(z)}{\partial z} = i\omega_f e^{-i\omega_f t} \int_{A_\infty} (\mathbf{e}_j^* \cdot \mathbf{p}_0) e^{i\beta_j z} \delta(\mathbf{r} - \mathbf{r_0}) \ \mathrm{d}A \tag{A.71}$$

$$\frac{\partial a_j(z)}{\partial z} = \frac{i\omega_f}{4N_j} e^{-i\omega_f t} \int_{A_\infty} (\mathbf{e}_j^* \cdot \mathbf{p}_0) e^{i\beta_j z} \delta(\mathbf{r} - \mathbf{r_0}) \ \mathrm{d}A \tag{A.72}$$

Integrating over z gives

$$a_j(z) = \frac{i\omega_f}{4N_j} e^{-i\omega_f t} \int_{V} (\mathbf{e}_j^* \cdot \mathbf{p}_0) e^{i\beta_j z} \delta(\mathbf{r} - \mathbf{r_0}) \ \mathrm{d}V \tag{A.73}$$

where the integral is now over the volume, V (i.e. over A_∞ and z or equivalently r,θ, and z). We now perform the integration, using the fact that the integrand contains a delta function: $\delta(\mathbf{r} - \mathbf{r_0})$. This gives us our final expression

$$a_j(z) = \frac{i\omega_f}{4N_j} e^{-i\omega_f t} e^{i\beta_j z_0} \left\{ \mathbf{e}_j^*(\mathbf{r}_0) \cdot \mathbf{p}_0(\mathbf{r}_0) \right\} \tag{A.74}$$

A.4 Extension to multiple emitters

For multiple emitters, we now have a slightly more complicated expression for the current. We now have N dipoles: the ith dipole having dipole moment $\mathbf{p_i} e^{i\omega_i t}$ and position $\mathbf{r}_i$. This gives a polarisation density of

$$\mathbf{P} = \sum_{i=1}^{N} \mathbf{p_i} e^{i\omega_i t} \delta(\mathbf{r} - \mathbf{r}_i) \tag{A.75}$$

which gives a current density of

$$\mathbf{J} = \frac{\partial \mathbf{P}}{\partial t} = -\sum_{i=1}^{N} i\omega_i \, \mathbf{p_i} e^{-i\omega_i t} \delta(\mathbf{r} - \mathbf{r}_i) \tag{A.76}$$

If we follow the same derivation as that for the single emitter above in section A.3, it follows identically until we make the substitution for $\mathbf{J}$. At that point we have the expression

$$4N_j \frac{\partial a_j(z)}{\partial z} = \int_{A_\infty} -\bar{\mathbf{E}}^* \cdot \mathbf{J} \; \mathrm{d}A \tag{A.77}$$

Substituting our expression for $\mathbf{J}$ in Equation (A.76) into this equation gives

$$4N_j \frac{\partial a_j(z)}{\partial z} = \int_{A_\infty} \bar{\mathbf{E}}^* \cdot \sum_{i=1}^{N} i\omega_i \, \mathbf{p_i} e^{-i\omega_i t} \delta(\mathbf{r} - \mathbf{r}_i) \; \mathrm{d}A \tag{A.78}$$

$$\frac{\partial a_j(z)}{\partial z} = \sum_{i=1}^{N} \frac{i\omega_i e^{-i\omega_i t}}{4N_j} \int_{A_\infty} \left(\mathbf{e}_j^* \cdot \mathbf{p_i} \right) e^{\beta_j z} \delta(\mathbf{r} - \mathbf{r}_i) \; \mathrm{d}A \tag{A.79}$$

Integrating over z gives

$$a_j(z) = \sum_{i=1}^{N} \frac{i\omega_i e^{-i\omega_i t}}{4N_j} \int_{V_\infty} \left(\mathbf{e}_j^* \cdot \mathbf{p_i} \right) e^{\beta_j z} \delta(\mathbf{r} - \mathbf{r}_i) \; \mathrm{d}V \tag{A.80}$$

where the integral is now over the whole volume of the domain, V_∞, rather than the r, θ plane A_∞. The delta functions, coming from the point-like nature of the dipoles, simplify the volume integral and the final expression becomes

$$a_j(z) = \sum_{i=1}^{N} \frac{i\omega_i}{4N_j} e^{-i\omega_i t} e^{\beta_j z_i} \left\{ \mathbf{e}_j^*(\mathbf{r}_i) \cdot \mathbf{p_i} \right\} \tag{A.81}$$

where z_i is the z-position of the ith dipole, i.e. in cylindrical co-ordinates $\mathbf{r}_i = (r_i, \theta_i, z_i)$.

A.5 Mode power from coupling coefficients

$$P = \frac{1}{2} \int_{A_\infty} (\mathbf{E} \times \mathbf{H}) \cdot \hat{z} \; \mathrm{d}A \tag{A.82}$$

$$P_j = \frac{1}{2} \int\limits_{A_\infty} (a_j \, \mathbf{e_j} \times a_j \, \mathbf{h_j}) \cdot \hat{z} \;\; \mathrm{d}A \tag{A.83}$$

$$P_j = |a_j|^2 \frac{1}{2} \int\limits_{A_\infty} (\, \mathbf{e_j} \times \, \mathbf{h_j}) \cdot \hat{z} \;\; \mathrm{d}A \tag{A.84}$$

$$P_j = |a_j|^2 N_j \tag{A.85}$$

B

Published papers

B.1 Diamond in Tellurite Glass: a New Medium for Quantum Information

Henderson, M.R., Gibson, B.C., Ebendorff-Heidepriem, H., Kuan, K., Afshar V, S., Orwa, J.O., Aharonovich, I., Tomljenovic-Hanic, S., Greentree, A.D., Prawer, S. & Monro, T.M. (2011) Diamond in Tellurite Glass: a New Medium for Quantum Information.
Advanced Materials, v. 23, pp. 2806-2810

NOTE:
This publication is included on pages 116-120 in the print copy of the thesis held in the University of Adelaide Library.

It is also available online to authorised users at:

http://doi.org/10.1002/adma.201100151

B.2 Dipole emitters in fiber: interface effects, collection efficiency and optimization

Dipole emitters in fiber: interface effects, collection efficiency and optimization

Matthew R. Henderson,[1,*] Shahraam Afshar V.,[1] Andrew D. Greentree,[2] and Tanya M. Monro[1]

[1] *Institute for Photonics & Advanced Sensing, School of Chemistry & Physics, University of Adelaide, Adelaide, SA 5005, Australia*

[2] *School of Physics, University of Melbourne, VIC 3010, Australia*

[*] *matthew.henderson@adelaide.edu.au*

Abstract: Single photon emitters coupled to optical fibers are becoming important as sources of non-classical light and nano-scale sensors. At present it is not possible to efficiently interface single photon emitters with the optical fiber platform, and there are particular challenges associated with the need to ensure highly efficient collection and delivery of emitted photons. To model single particle emission, we have considered the coupling of a dipole to an optical fiber mode as a function of orientation and position with respect to the core-cladding interface. Our model shows that it is possible to significantly enhance the collection efficiency into the guided modes as a result of modifications to the dipole emission pattern and power resulting from the surrounding fiber environment. For certain geometries the fiber-dipole coupling can result in a factor of 2.6 increase in the power emitted by the dipole.

© 2011 Optical Society of America

OCIS codes: (060.0060) Fiber optics and optical communications; (270.0270) Quantum optics.

References and links

1. I. Aharonovich, S. Castelletto, D. A. Simpson, C.-H. Su, A. D. Greentree, and S. Prawer, "Diamond based single photon emitters," Rep. Prog. Phys. **74**, 076501 (2011).
2. S. Afshar V., S. C. Warren-Smith, and T. M. Monro, "Enhancement of fluorescence-based sensing using microstructured optical fibres," Opt. Express **15**, 17891–17901 (2007).
3. E. M. Purcell, "Spontaneous emission probabilities at radio frequencies," Phys. Rev. **69**, 681 (1946).
4. W. Żakowicz and M. Janowicz, "Spontaneous emission in the presence of a dielectric cylinder," Phys. Rev. A **62**, 013820 (2000).
5. T. Søndergaard and B. Tromborg, "General theory for spontaneous emission in active dielectric microstructures: example of a fiber amplifier," Phys. Rev. A **64**, 033812 (2001).
6. J.-P. Hermier, M. Dahan, X. Brokmann, and L. Coolen, "Emission properties of single CdSe/ZnS quantum dots close to a dielectric interface," Chem. Phys. **318**, 91–98 (2005).
7. P. Anger, P. Bharadwaj, and L. Novotny, "Enhancement and quenching of single-molecule fluorescence," Phys. Rev. Lett. **96**, 113002 (2006).
8. I.-K. Hwang, S.-K. Kim, J.-K. Yang, S.-H. Kim, S. H. Lee, and Y.-H. Lee, "Curved-microfiber photon coupling for photonic crystal light emitter," Appl. Phys. Lett. **87**, 131107 (2005).
9. K.-M. C. Fu, P. E. Barclay, C. Santori, A. Faraon, and R. G. Beausoleil, "Low-temperature tapered-fiber probing of diamond nitrogen-vacancy ensembles coupled to GaP microcavities," New J. Phys. **13**, 055023 (2011).
10. D. D. Awschalom, R. Epstein, and R. Hanson, "The diamond age of spintronics," Sci. Am. **297**, 84–91 (2007).
11. H. Benisty, H. De Neve, and C. Weisbuch, "Impact of planar microcavity effects on light extraction — part I: basic concepts and analytical trends," IEEE J. Quantum Electron. **34**, 1612–1631 (1998).
12. M. R. Henderson, B. C. Gibson, H. Ebendorff-Heidepriem, K. Kuan, S. Afshar V., J. O. Orwa, I. Aharonovich, S. Tomljenovic-Hanic, A. D. Greentree, S. Prawer, and T. M. Monro, "Diamond in tellurite glass: a new medium for quantum information," Adv. Mater. **23**, 2806–2810 (2011).

#147939 - $15.00 USD Received 23 May 2011; revised 11 Jul 2011; accepted 13 Jul 2011; published 9 Aug 2011

13. T. M. Babinec, B. J. M. Hausmann, M. Khan, Y. Zhang, J. R. Maze, P. R. Hemmer, and M. Loncar, "A diamond nanowire single-photon source," Nat. Nanotechnol. **5**, 195–199 (2010).
14. A. Faraon, P. E. Barclay, C. Santori, K.-M. C. Fu, and R. G. Beausoleil, "Resonant enhancement of the zero-phonon emission from a colour centre in a diamond cavity," Nat. Photonics **5**, 301–305 (2011).
15. P. Siyushev, F. Kaiser, V. Jacques, I. Gerhardt, S. Bischof, H. Fedder, J. Dodson, M. Markham, D. Twitchen, F. Jelezko, and J. Wrachtrup, "Monolithic diamond optics for single photon detection," Appl. Phys. Lett. **97**, 241902 (2010).
16. T. Schröder, F. Gädeke, M. J. Banholzer, and O. Benson, "Ultra-bright and efficient single photon generation based on n-v centres in nanodiamonds on a solid immersion lens," New J. Phys. **13**, 055017 (2011).
17. L. Marseglia, J. P. Hadden, A. C. Stanley-Clarke, J. P. Harrison, B. Patton, Y.-L. D. Ho, B. Naydenov, F. Jelezko, J. Meijer, P. R. Dolan, J. M. Smith, J. G. Rarity, and J. L. O'Brien, "Nano-fabricated solid immersion lenses registered to single emitters in diamond," Appl. Phys. Lett. **98**, 189902 (2011).
18. P. E. Barclay, C. Santori, K.-M. Fu, R. G. Beausoleil, and O. Painter, "Coherent interference effects in a nano-assembled diamond NV center cavity-QED system," Opt. Express **17**, 8081–8097 (2009).
19. D. Englund, B. Shields, K. Rivoire, F. Hatami, J. Vučković, H. Park, and M. D. Lukin, "Deterministic coupling of a single nitrogen vacancy center to a photonic crystal cavity," Nano Lett. **10**, 3922–3926 (2010).
20. Y.-S. Park, A. K. Cook, and H. Wang, "Cavity QED with diamond nanocrystals and silica microspheres," Nano Lett. **6**, 2075–2079 (2006).
21. J. Rabeau, S. Huntington, A. Greentree, and S. Prawer, "Diamond chemical-vapor deposition on optical fibers for fluorescence waveguiding," Appl. Phys. Lett. **86**, 134104 (2005).
22. S. Kuhn, C. Hettich, C. Schmitt, J. Poizat, and V. Sandoghdar, "Diamond colour centres as a nanoscopic light source for scanning near-field optical microscopy," J. Microsc. **202**, 2–6 (2001).
23. E. Ampem-Lassen, D. A. Simpson, B. C. Gibson, S. Trpkovski, F. M. Hossain, S. T. Huntington, K. Ganesan, L. C. Hollenberg, and S. Prawer, "Nano-manipulation of diamond-based single photon sources," Opt. Express **17**, 11287–11293 (2009).
24. T. Schroder, A. W. Schell, G. Kewes, T. Aichele, and O. Benson, "Fiber-integrated diamond-based single photon source," Nano Lett. **11**, 198–202 (2011).
25. I. Aharonovich, A. D. Greentree, and S. Prawer, "Diamond photonics," Nat. Photonics **5**, 397–405 (2011).
26. M. R. Oermann, H. Ebendorff-Heidepriem, Y. Li, T.-C. Foo, and T. M. Monro, "Index matching between passive and active tellurite glasses for use in microstructured fiber lasers: erbium doped lanthanum-tellurite glass," Opt. Express **17**, 15578–15584 (2009).
27. T. M. Monro, S. Warren-Smith, E. P. Schartner, A. François, S. Heng, H. Ebendorff-Heidepriem, and S. Afshar V., "Sensing with suspended-core optical fibers," Opt. Fiber Technol. **16**, 343–356 (2010).
28. A. Snyder and J. Love, *Optical Waveguide Theory* (Springer, 1983).
29. A. F. Oskooi, D. Roundy, M. Ibanescu, P. Bermel, J. D. Joannopoulos, and S. G. Johnson, "MEEP: a flexible free-software package for electromagnetic simulations by the FDTD method," Comput. Phys. Commun. **181**, 687–702 (2010).

1. Introduction

There is a considerable impetus to improve the collection of single photon emission for quantum key distribution and quantum metrological applications [1]. However collection of emission from nano-scale objects is problematic, and in most practical settings, sensitivity is limited by photon collection efficiency. Here we explore a fiber-based approach to photon collection from dipole emitters. Some examples of the broad range of systems that are applicable to such analysis include fluorescence capture into optical fibers, crystal defect emission patterns and quantum dot radiation. In addition to single photon emission, our results also guide the exploration of the limits of sensing. The ultimate limit is single atom-scale sensors interacting with atomic objects of interest. Although there are many methods for signal transduction, optical readout provides one of the most convenient and robust methods.

The emission capture of fluorescence into the guided modes of optical fibers has been modelled previously [2], although this did not take into account the effects of the interface on the emitters and assumed an isotropic and homogeneous distribution of emitters. Both the spontaneous emission rate and radiation pattern [3–7] of dipoles are known to change near an interface between two materials. The spontaneous emission rate and radiation pattern changes have been modelled for the case of a dielectric cylinder [4, 5]. Measurements and modelling of the effect of a planar interface [6] and a gold nanoparticle [7] on dipole emission have been performed.

#147939 - $15.00 USD Received 23 May 2011; revised 11 Jul 2011; accepted 13 Jul 2011; published 9 Aug 2011
(C) 2011 OSA

Emission capture into a tapered fiber from an emitter in a photonic crystal cavity has been demonstrated [8, 9], showing theoretical and experimental collection efficiencies of 84% and an estimated 70% respectively. Here we examine the coupling between a dipole and an optical fiber. Although this is a general problem, for concreteness we illustrate our theory by focussing on diamond color centers coupled to optical fibers. With minor modifications, our results can be translated to any nanoscale emitter coupled to any fiber mode.

Diamond color centers, defects in the diamond lattice, have been identified as an important platform for solid-state quantum information processing [10]. In particular, diamond can host a variety of room temperature, photostable bright single photon sources [1]. Photon collection from color centers in bulk diamond is limited in efficiency by the large refractive index contrast of the diamond/air interface, as seen previously in semiconductor LEDs [11]. Such poor efficiencies ($\sim$4–5% [11]) limit the application of these sources to tasks such as quantum key distribution and quantum metrology. Incorporation of these color centers into photonic structures is important, in order to fabricate devices with these quantum properties. Access to a hybrid diamond-glass material [12] could allow the en-masse fabrication of such a device in the form of drawn optical fiber.

Advances in this area have previously been achieved by coupling the color centers to a photonic structure in order to modify the emission pattern for practical collection. Diamond nanopillars [13], microrings [14] and solid immersion lenses [15–17] with embedded color centers have been fabricated from bulk diamond. Color center emission has been coupled to non-diamond cavity structures such as microdisk resonators [18], photonic crystals [19], or microspheres [20] by nanopositioning the diamond nanocrystal onto the surface of the structure and coupling evanescently to the cavity. Color centers have been coupled to fiber structures by growing [21], or nanopositioning [22–24], diamond nanocrystals onto the endfaces of fibers. For a review of diamond photonics see [25].

We consider a new configuration for the capture of dipole emission, by either embedding the emitters within the core of a glass optical fiber [12] or coating them onto the core surface. As demonstrated in this work, these architectures enable the performance of devices based on dipoles to be enhanced. Because the treatment we present here is applicable to a range of types of dipoles, we do not specify a precise emitter or wavelength. However, many of the most practical room-temperature single photon sources have their main emission features in the red to near infra-red band (e.g. negatively charged nitrogen vacancy, silicon-vacancy, NE8, silicon-nickel and chromium-related color centers) [1], hence this band is used as the starting point for our fiber designs. Due to our recent demonstration of a versatile new nanodiamond-glass hybrid material [12] based on tellurite [26], a soft glass, we will focus on a tellurite core design in this work. This modelling work can be employed to exploit the potential of fiber devices made using this material by guiding the fiber design and can be used for the optimization of a broad range of emitters and fiber materials.

Here we derive an equation to describe the nanocrystal emission, in a fashion similar to [4], and use this to investigate the emitted power coupled into the fiber. This begins in Section 2, with the derivation of the equations that describe this capture, by representing the diamond emission as a summation of guided fiber modes and radiation modes and calculating the power in each of these modes. In Section 3 we explore the effect of varying core diameter, index contrast, and dipole position and orientation on the emission captured into the fiber's guided modes. High capture efficiencies and an enhancement of emission power from the high index contrast fiber are observed, which bodes well for future work towards highly efficient single photon devices based on microstructured optical fiber designs.

#147939 - $15.00 USD Received 23 May 2011; revised 11 Jul 2011; accepted 13 Jul 2011; published 9 Aug 2011
(C) 2011 OSA

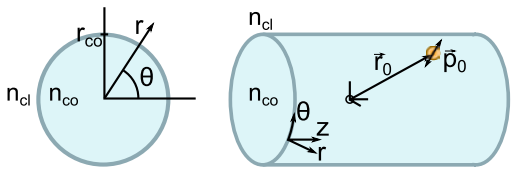

Fig. 1. Schematic of the modelling system.

2. Theory

We model the diamond color center as a dipole with dipole moment $\mathbf{p}_0$ and position $\mathbf{r}_0 = [r_0, \theta_0, z_0]$ oscillating with a frequency ω. Here we do not consider the linewidth of the dipole emission and assume that the emission is at a single wavelength. Since the typical dimensions of the diamond nanocrystals to be embedded in the tellurite [12] is 40nm and most single photon diamond center emission is at a wavelength of $\sim$ 650–750 nm [1], it is reasonable to assume that the refractive index of the background medium (in this case tellurite glass, $n = 2.02$) is not significantly perturbed by the introduction of low concentrations (ideally isolated) of diamond nanocrystals ($n \approx 2.4$) and so we treat the optical properties of the material as isotropic. The fiber is modelled as an infinitely long dielectric cylinder of radius r_{co} and refractive index n_{co} surrounded by an infinite region of refractive index n_{cl}. This geometry (shown in Fig. 1) is a reasonable approximation for the guided modes of step-index optical fibers, nanowires, or some classes of microstructured optical fibers such as suspended core optical fibers [27].

We expand the total field emitted by the dipole into two main components: the guided modes of the fiber and radiation modes, which is defined to be any part of the total field that cannot be expressed in terms of guided modes, as per Ref. [28]. Guided modes have discrete propagation constants ($kn_{\text{cl}} < \beta_j \leq kn_{\text{co}}$) and are solutions to the wave equation in the step-index fiber, while radiation modes span a continuum of propagation constants ($0 \leq \beta_{\text{rad}} < kn_{\text{cl}}$). The total electric field emitted by the dipole can be written as:

$$\mathbf{E} = \sum_j a_j(z)\mathbf{e}_j e^{-i\beta_j z} + a_{-j}(z)\mathbf{e}_{-j} e^{i\beta_{-j} z} + \text{radiation modes} \tag{1}$$

where β is the mode propagation constant, $\mathbf{e}$ is the mode electric field expression, and a is the mode coefficient, for the jth mode of the fiber (with $-j$ denoting a backward propagating mode). The magnetic field is expanded similarly. We can then solve for the mode coefficients, a, to find the power coupled into each mode from the dipole's emission. The $\mathbf{e}_j$ and β_j can be calculated by solving Maxwell's equations. For the guided modes, this gives the expected step-index mode field expressions [28]. To calculate the radiation modes, we separate the field into two terms, one representing the field in the absence of the waveguide ('free-space') and a second term that includes scattering from the waveguide. This separation appears in the cladding field as a Hankel function expression for boundary condition matching due to the presence of the fiber. Inside the fiber, as with the guided modes, a J bessel function fully satisfies the boundary condition. The radiation modes are then of the form [28]:

$$e_z = \begin{cases} a_\nu J_\nu(UR) f_\nu(\theta) & 0 \leq r < r_{\text{co}} \\ \left[c_\nu^f J_\nu(QR) + c_\nu^s H_\nu^{(1)}(QR)\right] f_\nu(\theta) & r_{\text{co}} \leq r < \infty \end{cases} \tag{2}$$

$$h_z = \begin{cases} b_\nu J_\nu(UR) g_\nu(\theta) & 0 \leq r < r_{\text{co}} \\ \left[d_\nu^f J_\nu(QR) + d_\nu^s H_\nu^{(1)}(QR)\right] g_\nu(\theta) & r_{\text{co}} \leq r < \infty \end{cases} \tag{3}$$

#147939 - $15.00 USD Received 23 May 2011; revised 11 Jul 2011; accepted 13 Jul 2011; published 9 Aug 2011
(C) 2011 OSA

$$f_\nu(\theta) = \begin{cases} \cos(\nu\theta) & \text{even modes} \\ \sin(\nu\theta) & \text{odd modes} \end{cases} \tag{4}$$

$$g_\nu(\theta) = \begin{cases} -\sin(\nu\theta) & \text{even modes} \\ \cos(\nu\theta) & \text{odd modes} \end{cases} \tag{5}$$

where ν is an azimuthal mode index, a_ν, b_ν, c_ν^f, c_ν^s, d_ν^f and d_ν^s are constants (see Appendix) found by applying the continuity conditions at the core-cladding interface, Q is used instead of β and is defined as

$$Q = r_{\text{co}}(k^2 n_{\text{cl}}^2 - \beta^2)^{1/2}, \tag{6}$$

and the superscripts f and s denote the 'free-space' and scattering terms, respectively. The four other components of the electric and magnetic field, e_r, e_θ, h_r and h_θ, can be expressed in terms of the derivatives of e_z and h_z [28] (see Appendix).

A collection of dipoles with dipole moments $\mathbf{p}_j$, frequencies ω_j and positions $\mathbf{r}_j$ contribute to a polarisation density given by:

$$\mathbf{P}(\mathbf{r}) = \sum_j \mathbf{p}_j e^{i\omega_j t}\delta(\mathbf{r} - \mathbf{r}_j) \tag{7}$$

For the case of a single dipole, this becomes $\mathbf{P}(\mathbf{r}) = \mathbf{p}_0 \exp(i\omega t)\delta(\mathbf{r} - \mathbf{r}_0)$. The current density associated with this dipole is:

$$\mathbf{J} = \frac{\partial \mathbf{P}}{\partial t} = i\omega \mathbf{p}_0 e^{i\omega t}\delta(\mathbf{r} - \mathbf{r}_0) \tag{8}$$

We use the reciprocity theorem [28]

$$\frac{\partial}{\partial z}\int_{A_\infty} \mathbf{F}\cdot\hat{z}\,\mathrm{d}A = \int_{A_\infty} \nabla\cdot\mathbf{F}\,\mathrm{d}A \tag{9}$$

with $\mathbf{F} = \mathbf{E}\times\bar{\mathbf{H}}^* + \bar{\mathbf{E}}^*\times\mathbf{H}$. In this equation $\mathbf{E}$ and $\mathbf{H}$ are the total fields as defined above in Eq. (1) with an associated current density $\mathbf{J}$ as defined in Eq. (8). Here the barred variables ($\bar{\mathbf{E}}$, $\bar{\mathbf{H}}$ and associated current density $\bar{\mathbf{J}}$) correspond to a system with no dipole and a single mode, such that $\bar{\mathbf{E}}$ and $\bar{\mathbf{H}}$ consist of any one mode from the expansion in Eq. (1), to give:

$$\bar{\mathbf{E}} = \mathbf{e}_j e^{i\beta_j z}, \quad \bar{\mathbf{H}} = \mathbf{h}_j e^{i\beta_j z}, \quad \bar{\mathbf{J}} = 0 \tag{10}$$

We then use Eq. (9) to solve for the mode coefficients, a_j, by substituting for these values. By assuming a non-absorbing waveguide (tellurite has a material loss of less than 1 dBm^{-1} from 600–1400 nm [26]) and using the orthogonality of the modes, shown in Eqs. (13) and (14), we find the mode coefficients to be:

$$a_j = \frac{i\omega}{4N_j} e^{-i\omega t} e^{i\beta_j z_0}\left[\mathbf{e}_j^*(\mathbf{r}_0)\cdot\mathbf{p}_0(\mathbf{r}_0)\right] \tag{11}$$

where ω is the frequency of the dipole and N_j is a normalisation term given by:

$$N_j = \frac{1}{2}\int_{A_\infty} (\mathbf{e}\times\mathbf{h}^*)\cdot\hat{z} \quad \mathrm{d}A \tag{12}$$

The guided modes satisfy the orthogonality condition

#147939 - $15.00 USD Received 23 May 2011; revised 11 Jul 2011; accepted 13 Jul 2011; published 9 Aug 2011
(C) 2011 OSA

$$\int_{A_\infty} (\mathbf{e}_j \times \mathbf{h}_k^*) \cdot \hat{z} \quad \mathrm{d}A = \int_{A_\infty} \left(\mathbf{e}_j^* \times \mathbf{h}_k\right) \cdot \hat{z} \quad \mathrm{d}A = 0 \qquad \text{for } j \neq k \tag{13}$$

and in a similar fashion for the radiation modes, taking into account the continuous nature of the propagation constant,

$$\int_{A_\infty} \left[\mathbf{e}_j(Q) \times \mathbf{h}_k^*(Q')\right] \cdot \hat{z} \quad \mathrm{d}A = \int_{A_\infty} \left[\mathbf{e}_j^*(Q') \times \mathbf{h}_k(Q)\right] \cdot \hat{z} \quad \mathrm{d}A = 0$$
$$\text{for all } Q \text{ if } j \neq k, \text{ and for } Q \neq Q' \text{ if } j = k \tag{14}$$

The power in each mode, P_j, can then be calculated from these mode coefficients by $P_j = |a_j|^2 N_j$. The total dipole emission power is also calculated from the mode coefficients by summing the power captured into all modes (all guided and radiation modes), i.e.

$$P_{\text{total}} = \sum_j P_j + \sum_\nu \int P_\nu(Q)\, \mathrm{d}Q \tag{15}$$

Summation of the radiation power includes an integral due to the continuous nature of the allowed β values, where β has been re-defined in terms of Q as in Eq. (6). The total power emitted by the dipole must be calculated in this way, rather than as in a bulk material, because of the creation of a cavity due to the fiber core-cladding interface. This alters the dipole emission characteristics [3–7] and leads to constructive or destructive interference resonances as the core diameter changes. Such resonances lead to the enhancement in the dipole emission in some cases. By using the mode coefficients, we include the effects of the core and cladding on the total field, and hence on the total power. This allows the full effect of the fiber on the emission to be calculated, and enables the estimation of both the capacity of the fiber to capture the emitted photons and also the changes in the dipole emission due to the surrounding environment.

3. Results

The total power emitted by a radially-oriented dipole located in the center (labeled 'center') and at the core-cladding interface (labeled 'interface') of the tellurite fiber is shown in Fig. 2a. The surrounding environment clearly has a significant effect on the dipole emission behaviour, with both the total emission power and the emission pattern changing significantly when constructive or destructive interference occurs due to the core-cladding interface. This is consistent with previous reports [4, 5] that placing the dipole in the vicinity of the step-index waveguide can increase the emitted power above that of a dipole in a bulk (homogeneous) material. Here we have calculated this power change as a function of the fiber's core diameter. This power has been normalized to the power emitted in bulk tellurite to highlight the effect of the waveguide.

Our results show that the total power oscillates above and below the bulk power as the varying core diameter changes the resonance condition of the dipole emission. It can be seen from Fig. 2a that the power emitted by a dipole on the core-cladding interface is approximately double that of a dipole located in the core center for the case of a radially oriented dipole. It can also be seen that, for a dipole located in the core center, as the core diameter increases, the emitted power tends towards the bulk power. In other words, the fiber begins to resemble the bulk tellurite at large core diameters, as expected. For the case of a dipole at the center, the power approaches zero for small core diameters rather than the cladding emission power. This can be understood by looking at the dipole environment. Regardless of core size, the dipole remains located in the core material and, as the core diameter reduces, the dipole approaches the core-cladding interface. In contrast, for a dipole located on the interface the surroundings approach an environment that consists only of the cladding material.

#147939 - $15.00 USD Received 23 May 2011; revised 11 Jul 2011; accepted 13 Jul 2011; published 9 Aug 2011
(C) 2011 OSA

Simulations based on the equations derived in Section 2 show good agreement (see 'center' curve in Fig. 2a) with data obtained computationally using the finite-difference time domain (FDTD) method, shown as black dots in Fig. 2a. This confirms the validity of this model as the FDTD method directly calculates the electric and magnetic fields in a grid system using Maxwell's equations and so is an independent method to the equations shown here. The FDTD package Meep [29] was used to perform these calculations. The boundaries of the computational space consisted of absorbing perfectly matched layers (PMLs) with a thickness of 1 distance unit for all calculations. The distance unit was defined as the free-space wavelength of 700 nm, to which all distances were normalized. Grid resolutions (the number of calculated points per distance unit) of 55, 55, and 30 were used for the 0.2, 0.42 and 0.6 μm core diameter calculations, respectively. The power was calculated by summing the integral of the Poynting vector normal to a sphere (with radius greater than the core radius and centered on the dipole emitter) at each time step in the calculation. Figure 2b shows convergence data for the FDTD method as a function of increasing grid resolution for the 0.42 μm core diameter case.

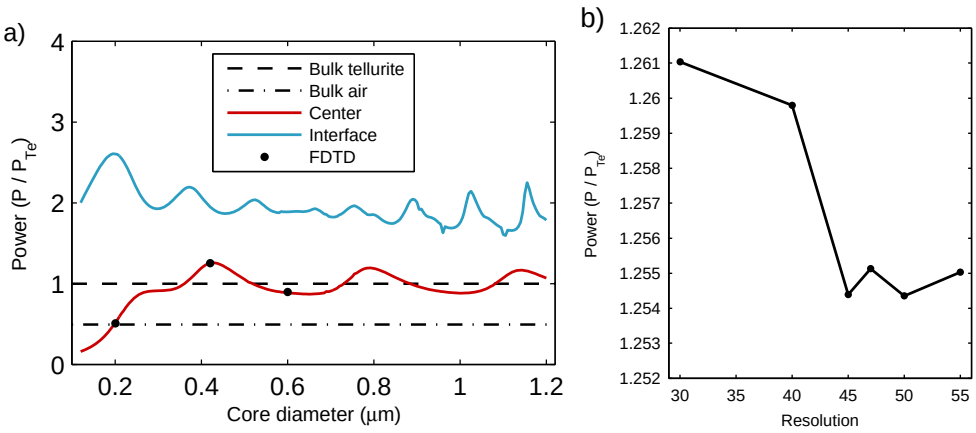

Fig. 2. (a) Power emitted by dipole vs. core diameter for a tellurite (n = 2.025) core fiber with an air cladding. A radially oriented dipole emitting at a wavelength of 700nm is located in the core center (red line) and alternately on the cladding side (blue line) of the core-cladding interface. Black dots show the comparison of data calculated using expressions in this paper to that obtained via the finite-difference time domain (FDTD) method. Power has been normalized to the power in a bulk material of the same index. The power oscillates above and below the bulk emitted power from changes in the interference condition due to the varying core diameter. (b) Total power vs. FDTD resolution showing convergence of FDTD solution for 0.4 μm core diameter fiber. Resolution is number of sampling points per wavelength (700 nm).

The power captured into the guided modes of the fiber is shown in Fig. 3 for a range of core diameters and two dipole positions (at the core center and on the core surface). The captured power has been normalized to the total power emitted by a dipole in bulk diamond, rather than bulk tellurite, to highlight the changes from the addition of the fiber structure and to more easily compare the captured fiber power to that obtained with the more traditional approach of collecting from a color center in a diamond crystal. Due to the large capture efficiency of the fiber and the increase in total power of the dipole, we find that the power captured into the guided modes of the fiber can be greater than the total emitted power of a dipole in bulk diamond. This is shown in Fig. 3a with a radially oriented dipole at the core-cladding interface. That is, for a specific dipole orientation and position, a fiber can collect $\sim$ 102% of the power

#147939 - $15.00 USD Received 23 May 2011; revised 11 Jul 2011; accepted 13 Jul 2011; published 9 Aug 2011
(C) 2011 OSA

emitted in total in a bulk diamond environment. More generally, for many core diameters and dipole positions, the power captured is greater than 20% of the power emitted in bulk diamond and it is typically higher for a radially oriented dipole ($\sim$ 50–60%). The discontinuities in the plots are due to the appearance of new guided modes as the core diameter is increased. Note that the radial and azimuthal orientations are equivalent for the case of a dipole at the center of the core.

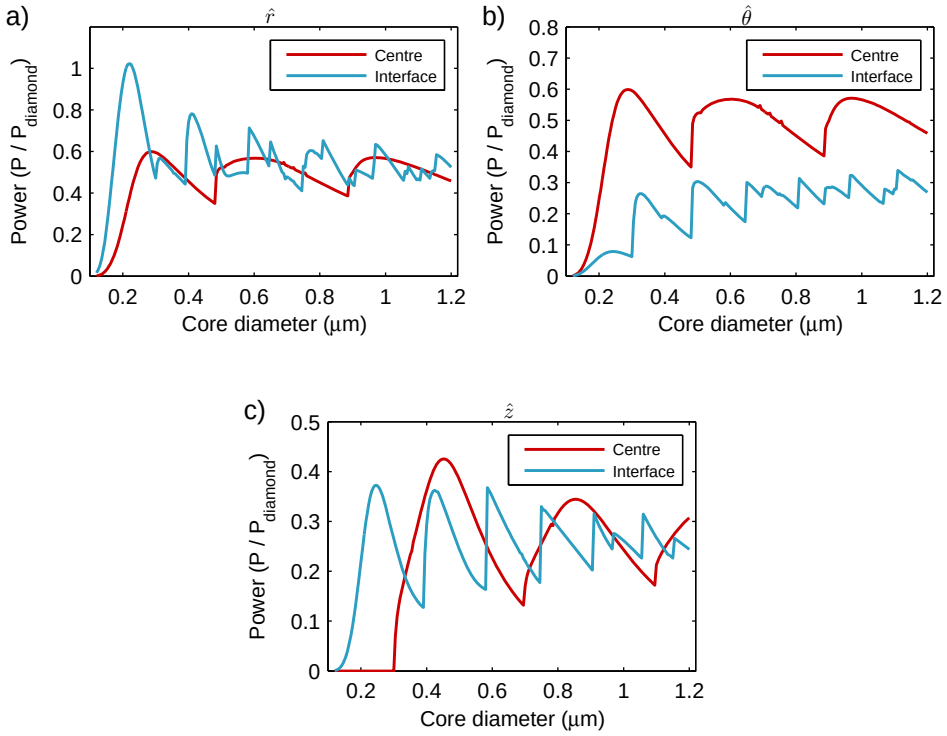

Fig. 3. Power captured into the fiber guided modes vs. core diameter for a tellurite core fiber in air cladding with a dipole emitting at a wavelength of 700nm in the core center and also on the cladding side of the core-cladding interface. Power is normalized to the total power emitted by the dipole in a bulk (homogeneous) diamond material. (a) Radially ($\hat{r}$) oriented dipole. (b) Azimuthally ($\hat{\theta}$) oriented dipole. (c) longitudinally ($\hat{z}$) oriented dipole. For most core diameters and dipole orientations the power captured into the guided modes of the fiber is greater than 20% of the power emitted in bulk diamond. For a specific orientation and core diameter (radial dipole at 0.22 μm) the captured power can be greater than the total power emitted in bulk diamond. Note that at the center of the core the radial and azimuthal orientations are equivalent.

Figure 4 shows the effect of the choice of the core material on the emission capture. The plot shows the captured power, in Figs. 4a and 4c, and the total power, in Figs. 4b and 4d, from the dipole at varying core diameters for three core materials: F2, SF57, (both commercially available silicate glasses) and tellurite ($n = 1.61$, 1.83 and 2.02 respectively at 700 nm wavelength). This shows that, as might be expected, strong capture is best achieved with a higher core refractive index. This effect is due to both the total emission power increasing and an increase in capture from the higher index, which can be seen by comparing the increase in total and guided power. As can be seen in Fig. 4, the peak total power increase from F2 to tellurite for a dipole at the interface is $2.2/1.39 = 1.58$, whereas the peak guided power increase is $1.02/0.49 = 2.08$,

#147939 - $15.00 USD Received 23 May 2011; revised 11 Jul 2011; accepted 13 Jul 2011; published 9 Aug 2011
(C) 2011 OSA

showing that the increase in total power alone does not account for the guided power increase.

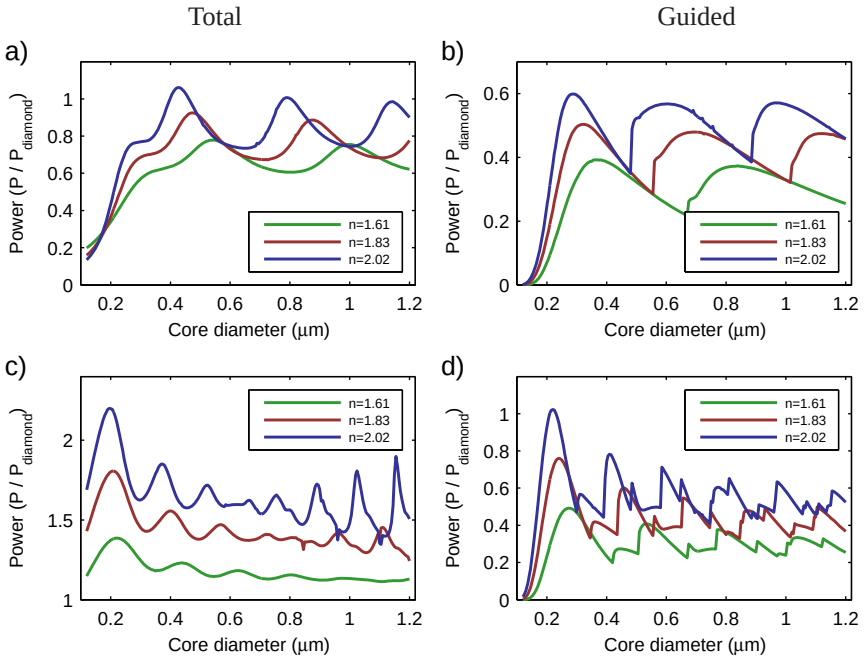

Fig. 4. Power vs. core diameter for an air-clad step index fiber with three different core materials: F2, SF57 and tellurite ($n = 1.61$, 1.83 and 2.02 respectively at 700 nm). (a) Total power and (b) guided power for a dipole positioned at the core center. (c) Total power and (d) guided power for a dipole positioned on the cladding side of the core-cladding interface. The dipole is radially oriented and emitting at a wavelength of 700nm. Power is normalized to the total power emitted by the dipole in a bulk (homogeneous) diamond material. As might be expected, captured power increases as the core index is increased.

The dipole position and orientation also has an effect on the capture of the dipole emission into the guided modes. Figure 5 shows the captured power as a function of dipole radial position for a radially oriented dipole. The discontinuity of the electric field at the core-cladding interface, visible at $r = r_{\mathrm{co}}$, generates a large radial electric field for the guided modes on the core surface (the cladding side of the core-cladding interface). As the dipole coupling equation, Eq. (11), includes an $\mathbf{E} \cdot \mathbf{p}$ term, this large radial field leads to a large capture into the guided modes for a radially oriented dipole.

4. Conclusion

We have presented a full-vectorial model describing the emission of a dipole in the vicinity of a step-index optical fiber. We show that the total power of the dipole changes depending on its orientation and position with respect to the fiber and that the emitted power can be ~ 2.6 times that of a dipole in a bulk material with the same refractive index. Interestingly, we have found that due to changes in the emitted power from interface effects, the emission power collected by the fiber can be larger than the total power emitted by a center in bulk diamond. This shows that a high index contrast fiber could perform well for single photon collection, due to both efficient capture and increased emission power. This model can be used to guide the fabrication of a single photon source which, because of the large capture efficiency obtainable, could be used in applications such as quantum key distribution or quantum metrology. The fabrication

#147939 - $15.00 USD Received 23 May 2011; revised 11 Jul 2011; accepted 13 Jul 2011; published 9 Aug 2011
(C) 2011 OSA

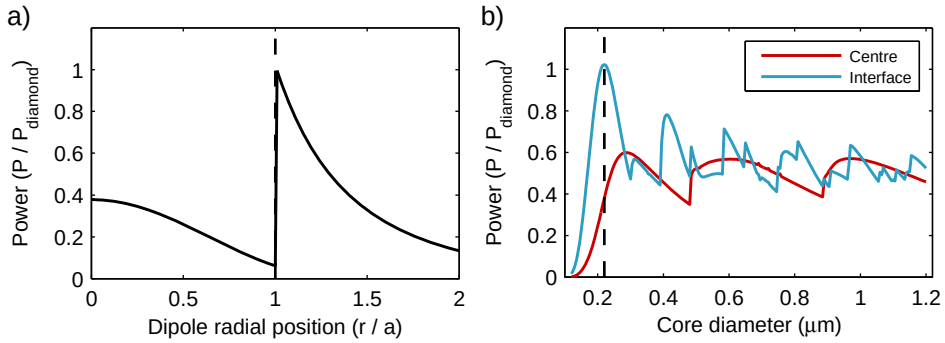

Fig. 5. Plots for a tellurite core fiber in air cladding with a radially oriented dipole emitting at a wavelength of 700nm. (a) Power captured into the fiber guided modes vs. dipole radial position for a fiber with a core diameter of 0.22 μm. (b) Power captured vs. core diameter, showing the core diameter at which the previous plot was calculated. Power is normalized to the total power emitted by the dipole in a bulk (homogeneous) diamond material. The discontinuity at the core-cladding interface is due to the discontinuity of the radial field.

of such a device presents many practical challenges, such as reducing the background photon count (from both the pump source and material fluorescence) and preventing the excitation of multiple color centers. However, these results show that such a device design could be a candidate for an efficient single photon source.

Appendix

The radiation mode expressions for the radial and azimuthal fields can be found using [28]

$$e_r = \frac{i}{k^2 n^2 - \beta^2}\left[\beta \frac{\partial e_z}{\partial r} + \left(\frac{\mu_0}{\varepsilon_0}\right)^{\frac{1}{2}} \frac{k}{r}\frac{\partial h_z}{\partial \theta}\right] \tag{16}$$

$$e_\theta = \frac{i}{k^2 n^2 - \beta^2}\left[\frac{\beta}{r}\frac{\partial e_z}{\partial \theta} - \left(\frac{\mu_0}{\varepsilon_0}\right)^{\frac{1}{2}} k \frac{\partial h_z}{\partial r}\right] \tag{17}$$

Substituting the expressions for e_z and h_z, Eqs. (2) and (3), into the above equations, Eqs. (16) and (17), gives:

For $0 \le r < r_{\text{co}}$

$$e_r = \frac{f_\nu(\theta)}{k^2 n_{\text{core}}^2 - \beta^2}\frac{iU}{2r_{\text{co}}}\left\{\beta a_\nu \left[J_{\nu-1}(UR) - J_{\nu+1}(UR)\right] - \left(\frac{\mu_0}{\varepsilon_0}\right)^{\frac{1}{2}} k b_\nu \left[J_{\nu-1}(UR) + J_{\nu+1}(UR)\right]\right\} \tag{18}$$

$$e_\theta = \frac{g_\nu(\phi)}{k^2 n_{\text{core}}^2 - \beta^2}\frac{iU}{2r_{\text{co}}}\left\{\beta a_\nu \left[J_{\nu-1}(UR) + J_{\nu+1}(UR)\right] - \left(\frac{\mu_0}{\varepsilon_0}\right)^{\frac{1}{2}} k b_\nu \left[J_{\nu-1}(UR) - J_{\nu+1}(UR)\right]\right\} \tag{19}$$

#147939 - $15.00 USD Received 23 May 2011; revised 11 Jul 2011; accepted 13 Jul 2011; published 9 Aug 2011
(C) 2011 OSA

For $r_{\mathrm{co}} \leq r < \infty$

$$e_r = \frac{f_\nu(\theta)}{k^2 n_{\mathrm{clad}}^2 - \beta^2} \frac{iQ}{2r_{\mathrm{co}}} \left(\beta \left\{ c_\nu^f \left[J_{\nu-1}(QR) - J_{\nu+1}(QR) \right] + c_\nu^s \left[H_{\nu-1}^{(1)}(QR) - H_{\nu+1}^{(1)}(QR) \right] \right\} \right.$$
$$\left. -k \left(\frac{\mu_0}{\varepsilon_0} \right)^{\frac{1}{2}} \left\{ d_\nu^f \left[J_{\nu-1}(QR) + J_{\nu+1}(QR) \right] + d_\nu^s \left[H_{\nu-1}^{(1)}(QR) + H_{\nu+1}^{(1)}(QR) \right] \right\} \right) \quad (20)$$

$$e_\theta = \frac{g_\nu(\phi)}{k^2 n_{\mathrm{clad}}^2 - \beta^2} \frac{iQ}{2r_{\mathrm{co}}} \left(\beta \left\{ c_\nu^f \left[J_{\nu-1}(QR) + J_{\nu+1}(QR) \right] + c_\nu^s \left[H_{\nu-1}^{(1)}(QR) + H_{\nu+1}^{(1)}(QR) \right] \right\} \right.$$
$$\left. -k \left(\frac{\mu_0}{\varepsilon_0} \right)^{\frac{1}{2}} \left\{ d_\nu^f \left[J_{\nu-1}(QR) - J_{\nu+1}(QR) \right] + d_\nu^s \left[H_{\nu-1}^{(1)}(QR) - H_{\nu+1}^{(1)}(QR) \right] \right\} \right) \quad (21)$$

where $U = r_{\mathrm{co}}(k^2 n_{\mathrm{co}}^2 - \beta^2)^{1/2}$, $Q = r_{\mathrm{co}}(k^2 n_{\mathrm{cl}}^2 - \beta^2)^{1/2}$, $V^2 = U^2 - Q^2$, and $R = r/r_{\mathrm{co}}$. The radiation mode coefficients (in Ref. [28] Table 25-3, page 525) appearing in Eqs. (2) and (3) are shown here in Table 1 for completeness. These coefficients are calculated by applying the boundary conditions to the electric and magnetic field expressions at the fiber core-cladding interface, i.e. e_z, e_θ, h_z, and h_θ are continuous at the interface.

#147939 - $15.00 USD Received 23 May 2011; revised 11 Jul 2011; accepted 13 Jul 2011; published 9 Aug 2011
(C) 2011 OSA

Table 1. Coefficients Appearing in Eqs. (2) and (3) for 'TM-like' (ITM) and 'TE-like' (ITE) Radiation Modes*

	ITE modes	ITM modes
a_ν	$-\frac{4}{\pi}\frac{\beta}{kn_{\rm co}^2}\frac{\nu}{kr_{\rm co}}\frac{V^2}{U^2Q^3}\frac{1}{J_\nu(U)H_\nu^{(1)}(Q)M_\nu}$	$-\frac{4}{\pi}\frac{n_{\rm cl}^2}{n_{\rm co}^2}\frac{1}{\beta r_{\rm co}Q}\frac{F_\nu}{J_\nu(U)H_\nu^{(1)}(Q)M_\nu}$
b_ν	$-\frac{4}{\pi}\left(\frac{\varepsilon_0}{\mu_0}\right)^{\frac{1}{2}}\frac{1}{Qkr_{\rm co}}\frac{G_\nu}{J_\nu(U)H_\nu^{(1)}(Q)M_\nu}$	$-\frac{4}{\pi}\frac{n_{\rm cl}^2}{n_{\rm co}^2}\left(\frac{\varepsilon_0}{\mu_0}\right)^{\frac{1}{2}}\frac{\nu}{kr_{\rm co}}\frac{V^2}{U^2Q^3}\frac{1}{J_\nu(U)H_\nu^{(1)}(Q)M_\nu}$
c_ν^f	0	$2i\frac{Q}{\beta r_{\rm co}}$
c_ν^s	$-\frac{4}{\pi}\frac{\beta}{kn_{\rm co}^2}\frac{\nu}{kr_{\rm co}}\frac{V^2}{U^2Q^3}\frac{1}{\left\{H_\nu^{(1)}(Q)\right\}^2M_\nu}$	$-2i\frac{Q}{\beta r_{\rm co}}\frac{J_\nu(Q)}{H_\nu^{(1)}(Q)}\frac{A_\nu}{M_\nu}$
d_ν^f	$2i\left(\frac{\varepsilon_0}{\mu_0}\right)^{\frac{1}{2}}\frac{Q}{r_{\rm co}k}$	0
d_ν^s	$-2i\left(\frac{\varepsilon_0}{\mu_0}\right)^{\frac{1}{2}}\frac{Q}{r_{\rm co}k}\frac{J_\nu(Q)}{H_\nu^{(1)}(Q)}\frac{B_\nu}{M_\nu}$	$-\frac{4}{\pi}\frac{n_{\rm cl}^2}{n_{\rm co}^2}\left(\frac{\varepsilon_0}{\mu_0}\right)^{\frac{1}{2}}\frac{\nu}{r_{\rm co}k}\frac{V^2}{U^2Q^3}\frac{1}{\left\{H_\nu^{(1)}(Q)\right\}^2M_\nu}$
N_j	$\frac{2\pi r_{\rm co}^2}{Q}\left(\frac{\varepsilon_0}{\mu_0}\right)^{\frac{1}{2}}\frac{\beta}{k}\times\begin{cases}1 & \text{for } \nu>0\\ 2 & \text{for } \nu=0\end{cases}$	$\frac{2\pi r_{\rm co}^2}{Q}\left(\frac{\varepsilon_0}{\mu_0}\right)^{\frac{1}{2}}\frac{kn_{\rm cl}^2}{\beta}\times\begin{cases}1 & \text{for } \nu>0\\ 2 & \text{for } \nu=0\end{cases}$

*These correspond to the pure TM and TE modes in the 'free-space' terms that are subsequently altered by the perturbation of the waveguide. From [28].

$$F_\nu = \frac{J_\nu'(U)}{UJ_\nu(U)} - \frac{H_\nu^{(1)'}(Q)}{QH_\nu^{(1)}(Q)} \tag{22}$$

$$G_\nu = \frac{J_\nu'(U)}{UJ_\nu(U)} - \frac{n_{\rm cl}^2}{n_{\rm co}^2}\frac{H_\nu^{(1)'}(Q)}{QH_\nu^{(1)}(Q)} \tag{23}$$

$$A_\nu = M_\nu - \frac{2i}{\pi}\frac{n_{\rm cl}^2}{n_{\rm co}^2}\frac{F_\nu}{Q^2J_\nu(Q)H_\nu^{(1)}(Q)} \tag{24}$$

$$B_\nu = M_\nu - \frac{2i}{\pi}\frac{G_\nu}{Q^2J_\nu(Q)H_\nu^{(1)}(Q)} \tag{25}$$

$$M_\nu = \left(\frac{\nu\beta}{kn_{\rm co}}\right)^2\left(\frac{V}{UQ}\right)^4 - F_\nu G_\nu \tag{26}$$

#147939 - $15.00 USD Received 23 May 2011; revised 11 Jul 2011; accepted 13 Jul 2011; published 9 Aug 2011
(C) 2011 OSA

Acknowledgments

A.D.G. acknowledges the support of an ARC Queen Elizabeth II Fellowship (DP0880466). T.M.M. acknowledges the support of an ARC Federation Fellowship (FF0883189). The authors acknowledge Stephen Warren-Smith for preceding fluorescence capture modelling.

#147939 - $15.00 USD Received 23 May 2011; revised 11 Jul 2011; accepted 13 Jul 2011; published 9 Aug 2011
(C) 2011 OSA

C

Glass fabrication details

C.1 Sample number conversion to in-house codes

Glass	In-house	Preform	In-house	Design
G1	KK1176			
G2	KK1350	P2	Tep71	Rod
G3	KK1382	P3	Tep79	Rod
G4	KK1392	P4	Tep82	Rod
G5	KTe020	P5	Tep125	Rod
G6	KK1410	P6	Tep89	Wagon-wheel

Table C.1: Glass and preform samples.

Fibre	In-house	Tube	In-house	Design
F2	Tef57			
F3	Tef65			
F4	Tef67			
F5	Tef102			
F6a	Tef70		Tep86	
F6b	Tef98	T6b	Tep120	Wedge tube
F6c	Tef100	T6c	Tep86	Cut slot

Table C.2: Fibre samples.

C.2 Tellurite annealing process

Tellurite billets are annealed after each processing step to relieve the introduced internal stresses, to help prevent cracking during handling, clamping and cutting. The furnace annealing temperature profile used for the samples presented here is as:

Annealing protocol

RT	→	160 °C	at 3 °C min^{-1}
160 °C	→	210 °C	at 2 °C min^{-1}
210 °C	→	260 °C	at 1 °C min^{-1}
260 °C	→	315 °C	at 0.5 °C min^{-1}
Dwell for 4 h			
315 °C	→	200 °C	at 0.1 °C min^{-1}
200 °C	→	150 °C	at 0.2 °C min^{-1}
150 °C	→	RT	at 0.5 °C min^{-1}

RT: Room temperature

C.3 Subracting Fresnel reflection from UV-Vis spectra

$$T_{\text{Fresnel}} = \frac{\left(1 - \left\{\frac{n-1}{n+1}\right\}^2\right)^2}{1 - \left(\frac{n-1}{n+1}\right)^4} \tag{C.1}$$

C.4 Calculating loss

$$\text{Loss}\,(\text{dB}) = -10 \log_{10} \frac{T}{T_0} \tag{C.2}$$

where T/T_0 is the transmission fraction through the sample.

$$\text{Loss}_{\text{glass}}\,(\text{dB m}^{-1}) = \frac{\text{Loss}_{\text{total}}\,(\text{dB}) - \text{Loss}_{\text{Fresnel}}\,(\text{dB})}{\text{Sample length}\,(\text{m})} \tag{C.3}$$

Bibliography

[1] M. R. Oermann, H. Ebendorff-Heidepriem, Y. Li, T.-C. Foo, and T. M. Monro, "Index matching between passive and active tellurite glasses for use in microstructured fiber lasers: Erbium doped lanthanum-tellurite glass," Optics Express **17**, 15578–15584 (2009).

[2] F. Jelezko and J. Wrachtrup, "Single defect centres in diamond: a review," Physica Status Solidi A **203**, 3207–25 (2006).

[3] A. Zaitsev, *Optical Properties of Diamond* (Springer, Berlin, 2001).

[4] A. Beveratos, S. Kuhn, R. Brouri, T. Gacoin, J.-P. Poizat, and P. Grangier, "Room temperature stable single-photon source," European Physical Journal D **18**, 191–6 (2002).

[5] A. Beveratos, R. Brouri, T. Gacoin, A. Villing, J.-P. Poizat, and P. Grangier, "Single photon quantum cryptography," Physical Review Letters **89**, 187901/1–4 (2002).

[6] K. Johnston and A. Mainwood, "Properties of nickel nitrogen complexes in diamond: stability and electronic structure," in "Diamond and Related Materials," , vol. 12 (Elsevier, Netherlands, 2003), vol. 12, pp. 516–20. 13th European Conference on Diamond, Diamond-like Materials, Carbon Nanotubes, Nitrides and Silicon Carbide (Diamond 2002), 3-8 Sept. 2002, Granada, Spain.

[7] E. Wu, J. Rabeau, G. Roger, F. Treussart, H. Zeng, P. Grangier, S. Prawer, and J.-F. Roch, "Room temperature triggered single-photon source in the near infrared," New Journal of Physics **9**, 434 (11 pp.) (2007).

[8] C. Wang, C. Kurtsiefer, H. Weinfurter, and B. Burchard, "Single photon emission from siv centres in diamond produced by ion implantation," Journal of Physics B: Atomic, Molecular and Optical Physics **39**, 37 (2006).

[9] I. Aharonovich, S. Castelletto, B. C. Johnson, J. C. McCallum, D. A. Simpson, A. D. Greentree, and S. Prawer, "Chromium single-photon emitters in diamond fabricated by ion implantation," Physical Review B **81**, 121201 (2010).

[10] I. Aharonovich, S. Castelletto, D. A. Simpson, C.-H. Su, A. D. Greentree, and S. Prawer, "Diamond-based single-photon emitters," Reports on Progress in Physics **74**, 076501 (2011).

[11] F. Waldermann, P. Olivero, J. Nunn, K. Surmacz, Z. Wang, D. Jaksch, R. Taylor, I. Walmsley, M. Draganski, P. Reichart, A. Greentree, D. Jamieson, and S. Prawer,

"Creating diamond color centers for quantum optical applications," Diamond and Related Materials **16**, 1887 – 1895 (2007).

[12] J. Meijer, B. Burchard, M. Domhan, C. Wittmann, T. Gaebel, I. Popa, F. Jelezko, and J. Wrachtrup, "Generation of single color centers by focused nitrogen implantation." Applied Physics Letters **87**, 261909 (2005).

[13] J. R. Rabeau, P. Reichart, G. Tamanyan, D. N. Jamieson, S. Prawer, F. Jelezko, T. Gaebel, I. Popa, M. Domhan, and J. Wrachtrup, "Implantation of labelled single nitrogen vacancy centers in diamond using ^{15}N." Applied Physics Letters **88**, 023113 (2006).

[14] C. Kurtsiefer, S. Mayer, P. Zarda, and H. Weinfurter, "Stable solid-state source of single photons," Physical Review Letters **85**, 290–3 (2000).

[15] C. Brunel, B. Lounis, P. Tamarat, and M. Orrit, "Triggered source of single photons based on controlled single molecule fluorescence," Physical Review Letters **83**, 2722–5 (1999).

[16] M. Pelton, C. Santori, J. Vuckovic, Bingyang Zhang, G. Solomon, J. Plant, and Y. Yamamoto, "Efficient source of single photons: a single quantum dot in a micropost microcavity," Physical Review Letters **89**, 233602–1–4 (2002).

[17] C. Santori, M. Pelton, G. Solomon, Y. Dale, and Y. Yamamoto, "Triggered single photons from a quantum dot," Physical Review Letters **86**, 1502–5 (2001).

[18] R. Brouri, A. Beveratos, J. Poizat, and P. Grangier, "Photon antibunching in the fluorescence of individual color centers in diamond," Optics Letters **25**, 1294–1296 (2000).

[19] A. Beveratos, R. Brouri, T. Gacoin, J.-P. Poizat, and P. Grangier, "Nonclassical radiation from diamond nanocrystals," Physical Review A (Atomic, Molecular, and Optical Physics) **64**, 061802/1–4 (2001).

[20] A. D. Greentree, B. A. Fairchild, F. M. Hossain, and S. Prawer, "Diamond integrated quantum photonics," Materials Today **11**, 22 – 31 (2008).

[21] T. Gaebel, M. Domhan, C. Wittmann, I. Popa, F. Jelezko, J. Rabeau, A. Greentree, S. Prawer, E. Trajkov, P. Hemmer, and J. Wrachtrup, "Photochromism in single nitrogen-vacancy defect in diamond," Applied Physics B (Lasers and Optics) **B82**, 243–6 (2006).

[22] V. M. Acosta, E. Bauch, A. Jarmola, L. J. Zipp, M. P. Ledbetter, and D. Budker, "Broadband magnetometry by infrared-absorption detection of nitrogen-vacancy ensembles in diamond," Applied Physics Letters **97**, 174104 (2010).

[23] J. M. Taylor, P. Cappellaro, L. Childress, L. Jiang, D. Budker, P. R. Hemmer, A. Yacoby, R. Walsworth, and M. D. Lukin, "High-sensitivity diamond magnetometer with nanoscale resolution," Nature Physics **4**, 810–816 (2008).

[24] G. Balasubramanian, R. Bratschitsch, I. Chan, T. Hanke, P. R. Hemmer, M. A. Hmoud, F. Jelezko, C. Kim, R. Kolesov, A. Krueger, A. Leitenstorfer, C. Shin, J. Tisler, A. Wojcik, and J. Wrachtrup, "Nanoscale imaging magnetometry with diamond spins under ambient conditions," Nature **455**, 648 (2008).

[25] E. van Oort, N. B. Manson, and M. Glasbeek, "Optically detected spin coherence of the diamond n-v centre in its triplet ground state," Journal of Physics C: Solid State Physics **21**, 4385 (1988).

[26] I. Aharonovich, A. D. Greentree, and S. Prawer, "Diamond photonics," Nature Photonics **5**, 397–405 (2011).

[27] T. M. Babinec, B. J. M. Hausmann, M. Khan, Y. Zhang, J. R. Maze, P. R. Hemmer, and M. Loncar, "A diamond nanowire single-photon source," Nature Nanotechnology **5**, 195–199 (2010).

[28] B. J. Hausmann, M. Khan, Y. Zhang, T. M. Babinec, K. Martinick, M. McCutcheon, P. R. Hemmer, and M. Loncar, "Fabrication of diamond nanowires for quantum information processing applications," Diamond and Related Materials **19**, 621 – 629 (2010). Proceedings of Diamond 2009, The 20th European Conference on Diamond, Diamond-Like Materials, Carbon Nanotubes and Nitrides, Part 1.

[29] J. P. Hadden, J. P. Harrison, A. C. Stanley-Clarke, L. Marseglia, Y.-L. D. Ho, B. R. Patton, J. L. O'Brien, and J. G. Rarity, "Strongly enhanced photon collection from diamond defect centers under microfabricated integrated solid immersion lenses," Applied Physics Letters **97**, 241901 (2010).

[30] L. Marseglia, J. P. Hadden, A. C. Stanley-Clarke, J. P. Harrison, B. Patton, Y.-L. D. Ho, B. Naydenov, F. Jelezko, J. Meijer, P. R. Dolan, J. M. Smith, J. G. Rarity, and J. L. O'Brien, "Nanofabricated solid immersion lenses registered to single emitters in diamond," Applied Physics Letters **98**, 133107 (2011).

[31] P. Olivero, S. Rubanov, P. Reichart, B. Gibson, S. Huntington, J. Rabeau, A. Greentree, J. Salzman, D. Moore, D. Jamieson, and S. Prawer, "Ion-beam-assisted lift-off technique for three-dimensional micromachining of freestanding single-crystal diamond," Advanced Materials **17**, 2427–2430 (2005).

[32] M. P. Hiscocks, K. Ganesan, B. C. Gibson, S. T. Huntington, F. Ladouceur, and S. Prawer, "Diamond waveguides fabricated by reactive ion etching," Optics Express **16**, 19512–19519 (2008).

[33] B. A. Fairchild, P. Olivero, S. Rubanov, A. D. Greentree, F. Waldermann, R. A. Taylor, I. Walmsley, J. M. Smith, S. Huntington, B. C. Gibson, D. N. Jamieson, and S. Prawer, "Fabrication of ultrathin single-crystal diamond membranes," Advanced Materials **20**, 4793–4798 (2008).

[34] E. Ampem-Lassen, D. A. Simpson, B. C. Gibson, S. Trpkovski, F. M. Hossain, S. T. Huntington, K. Ganesan, L. C. Hollenberg, and S. Prawer, "Nano-manipulation of diamond-based single photon sources," Optics Express **17**, 11287–11293 (2009).

[35] T. Schroder, A. W. Schell, G. Kewes, T. Aichele, and O. Benson, "Fiber-integrated diamond-based single photon source," Nano Letters **11**, 198–202 (2011).

[36] S. Schietinger, T. Schroder, and O. Benson, "One-by-one coupling of single defect centers in nanodiamonds to high-q modes of an optical microresonator," Nano Letters **8**, 3911–3915 (2008). PMID: 18811213.

[37] P. E. Barclay, C. Santori, K.-M. Fu, R. G. Beausoleil, and O. Painter, "Coherent interference effects in a nano-assembled diamond nv center cavity-qed system," Optics Express **17**, 8081–8097 (2009).

[38] J. Wolters, A. W. Schell, G. Kewes, N. Nsse, M. Schoengen, H. Dscher, T. Hannappel, B. Lchel, M. Barth, and O. Benson, "Enhancement of the zero phonon line emission from a single nitrogen vacancy center in a nanodiamond via coupling to a photonic crystal cavity." Applied Physics Letters **97**, 141108 (2010).

[39] Y.-S. Park, A. K. Cook, and H. Wang, "Cavity QED with diamond nanocrystals and silica microspheres," Nano Letters **6**, 2075–2079 (2006).

[40] D. Englund, B. Shields, K. Rivoire, F. Hatami, J. Vučković, H. Park, and M. D. Lukin, "Deterministic coupling of a single nitrogen vacancy center to a photonic crystal cavity," Nano Letters **10**, 3922–3926 (2010).

[41] J. Rabeau, S. Huntington, A. Greentree, and S. Prawer, "Diamond chemical-vapor deposition on optical fibers for fluorescence waveguiding," Applied Physics Letters **86**, 134104–1–3 (2005).

[42] T. Schröder, M. Fujiwara, T. Noda, H.-Q. Zhao, O. Benson, and S. Takeuchi, "A nanodiamond-tapered fiber system with high single-mode coupling efficiency," Optics Express **20**, 10490–10497 (2012).

[43] H. Ebendorff-Heidepriem and T. M. Monro, "Extrusion of complex preforms for microstructured optical fibers," Optics Express **15**, 15086–15092 (2007).

[44] T. M. Monro and H. Ebendorff-Heidepriem, "Progress in microstructured optical fibers," Annual Review of Materials Research **36**, 467–495 (2006).

[45] J. C. Knight, "Photonic crystal fibres," Nature **424**, 847 (2003).

[46] J. Lægsgaard and A. Bjarklev, "Microstructured optical fibers—fundamentals and applications," Journal of the American Ceramic Society **89**, 2–12 (2006).

[47] T. M. Monro, S. Warren-Smith, E. P. Schartner, A. François, S. Heng, H. Ebendorff-Heidepriem, and S. Afshar V., "Sensing with suspended-core optical fibers," Optical Fiber Technology **16**, 343 – 356 (2010). Special Fiber Structures and their Applications.

[48] A. S. Webb, F. Poletti, D. J. Richardson, and J. K. Sahu, "Suspended-core holey fiber for evanescent-field sensing," Optical Engineering **46**, 010503–010503–3 (2007).

[49] Y. Zhu, R. T. Bise, J. Kanka, P. Peterka, and H. Du, "Fabrication and characterization of solid-core photonic crystal fiber with steering-wheel air-cladding for strong evanescent field overlap," Optics Communications **281**, 55 – 60 (2008).

[50] H. Ebendorff-Heidepriem, P. Petropoulos, S. Asimakis, V. Finazzi, R. Moore, K. Frampton, F. Koizumi, D. Richardson, and T. Monro, "Bismuth glass holey fibers with high nonlinearity," Optics Express **12**, 5082–5087 (2004).

[51] J. Leong, P. Petropoulos, J. Price, H. Ebendorff-Heidepriem, S. Asimakis, R. Moore, K. Frampton, V. Finazzi, X. Feng, T. Monro, and D. Richardson, "High-nonlinearity dispersion-shifted lead-silicate holey fibers for efficient 1-μm pumped supercontinuum generation," Journal of Lightwave Technology **24**, 183 – 190 (2006).

[52] Y. Xu, J. S. Vučković, R. K. Lee, O. J. Painter, A. Scherer, and A. Yariv, "Finite-difference time-domain calculation of spontaneous emission lifetime in a microcavity," Journal of the Optical Society of America B **16**, 465–474 (1999).

[53] D. Englund, D. Fattal, E. Waks, G. Solomon, B. Zhang, T. Nakaoka, Y. Arakawa, Y. Yamamoto, and J. Vučković, "Controlling the spontaneous emission rate of single quantum dots in a two-dimensional photonic crystal," Physical Review Letters **95**, 013904 (2005).

[54] J. Dowling, "Spontaneous emission in cavities: How much more classical can you get?" Foundations of Physics **23**, 895–905 (1993).

[55] W. Lukosz and R. E. Kunz, "Light emission by magnetic and electric dipoles close to a plane interface. I. total radiated power," Journal of the Optical Society of America **67**, 1607–1615 (1977).

[56] W. Lukosz, "Light emission by magnetic and electric dipoles close to a plane dielectric interface. III. radiation patterns of dipoles with arbitrary orientation," Journal of the Optical Society of America **69**, 1495–1503 (1979).

[57] E. M. Purcell, "Spontaneous emission probabilities at radio frequencies," in "Physical Review," , vol. 69 (1946), vol. 69, p. 681.

[58] W. Żakowicz and M. Janowicz, "Spontaneous emission in the presence of a dielectric cylinder," Physical Review A **62**, 013820 (2000).

[59] T. Søndergaard and B. Tromborg, "General theory for spontaneous emission in active dielectric microstructures: Example of a fiber amplifier," Physical Review A **64**, 033812 (2001).

[60] S. Afshar V., S. C. Warren-Smith, and T. M. Monro, "Enhancement of fluorescence-based sensing using microstructured optical fibres," Optics Express **15**, 17891–17901 (2007).

[61] J.-P. Hermier, M. Dahan, X. Brokmann, and L. Coolen, "Emission properties of single CdSe/ZnS quantum dots close to a dielectric interface," Chemical Physics **318**, 91–8 (2005).

[62] P. Anger, P. Bharadwaj, and L. Novotny, "Enhancement and quenching of single-molecule fluorescence," Physical Review Letters **96**, 113002/1–4 (2006).

[63] A. Snyder and J. Love, *Optical waveguide theory* (Springer, 1983).

[64] J. D. Jackson, *Classical electrodynamics* (New York : Wiley, c1999), 3rd ed.

[65] P. Bermel, J. D. Joannopoulos, Y. Fink, P. A. Lane, and C. Tapalian, "Properties of radiating pointlike sources in cylindrical omnidirectionally reflecting waveguides," Physical Review B **69**, 035316 (2004).

[66] D. P. Fussell, R. C. McPhedran, and C. Martijn de Sterke, "Decay rate and level shift in a circular dielectric waveguide," Physical Review A **71**, 013815 (2005).

[67] *Product information PI1036* (Corning Incorporated, 2002).

[68] K. R. Hiremath, M. Hammer, R. Stoffer, L. Prkna, and J. Čtyroký, "Analytic approach to dielectric optical bent slab waveguides," Optical and Quantum Electronics **37**, 37–61 (2005).

[69] K. Hiremath, R. Stoffer, and M. Hammer, "Modeling of circular integrated optical microresonators by 2-d frequency domain coupled mode theory," Optics Communications **257**, 277 – 297 (2006).

[70] L. Prkna, J. Čtyroký, and M. Hubálek, "Ring microresonator as a photonic structure with complex eigenfrequency," Optical and Quantum Electronics **36**, 259–269 (2004).

[71] T. Yamamoto and M. Koshiba, "Analysis of propagation characteristics of whispering gallery modes in a dielectric disk or a curved rectangular dielectric waveguide," Journal of Lightwave Technology **11**, 400 – 404 (1993).

[72] S. Hagness, D. Rafizadeh, S. Ho, and A. Taflove, "Fdtd microcavity simulations: design and experimental realization of waveguide-coupled single-mode ring and whispering-gallery-mode disk resonators," Lightwave Technology, Journal of **15**, 2154 –2165 (1997).

[73] V. Zamora, A. Díez, M. V. Andrés, and B. Gimeno, "Cylindrical optical microcavities: Basic properties and sensor applications," Photonics and Nanostructures - Fundamentals and Applications **9**, 149 – 158 (2011).

[74] E. Krioukov, D. W. Klunder, A. Driessen, J. Greve, and C. Otto, "Sensor based on an integrated optical microcavity," Optics Letters **27**, 512–514 (2002).

[75] A. Taflove and S. Hagness, *Computational Electrodynamics: The Finite-Difference Time-Domain Method*, Artech House Antennas and Propagation Library (Artech House, 2005), 3rd ed.

[76] J.-P. Berenger, "A perfectly matched layer for the absorption of electromagnetic waves," Journal of Computational Physics **114**, 185 – 200 (1994).

[77] A. F. Oskooi, D. Roundy, M. Ibanescu, P. Bermel, J. D. Joannopoulos, and S. G. Johnson, "MEEP: A flexible free-software package for electromagnetic simulations by the FDTD method," Computer Physics Communications **181**, 687–702 (2010).

[78] "Meep website," http://ab-initio.mit.edu/meep/ (2012).

[79] N. S. Xu, J. Chen, and S. Z. Deng, "Effect of heat treatment on the properties of nano-diamond under oxygen and argon ambient," Diamond and Related Materials **11**, 249 – 256 (2002).

[80] J.-C. Pu, S.-F. Wang, and J. C. Sung, "High-temperature oxidation behavior of nanocrystalline diamond films," Journal of Alloys and Compounds **489**, 638 – 644 (2010).

[81] B. R. Smith, D. Gruber, and T. Plakhotnik, "The effects of surface oxidation on luminescence of nano diamonds," Diamond and Related Materials **19**, 314 – 318 (2010).

[82] J.-C. Pu, S.-F. Wang, and J. C. Sung, "High-temperature oxidation behaviors of CVD diamond films," Applied Surface Science **256**, 668 – 673 (2009).

[83] P. John, N. Polwart, C. E. Troupe, and J. I. B. Wilson, "The oxidation of (100) textured diamond," Diamond and Related Materials **11**, 861 – 866 (2002).

[84] I. H. Malitson, "Interspecimen comparison of the refractive index of fused silica," Journal of the Optical Society of America **55**, 1205–1208 (1965).

[85] S. Manning, H. Ebendorff-Heidepriem, and T. M. Monro, "Ternary tellurite glasses for the fabrication of nonlinear optical fibres," Opt. Mater. Express **2**, 140–152 (2012).

[86] V. V. Ravi Kanth Kumar, A. George, J. Knight, and P. Russell, "Tellurite photonic crystal fiber," Optics Express **11**, 2641–2645 (2003).

[87] R. H. Brown and R. Q. Twiss, "Correlation between photons in two coherent beams of light," Nature **177**, 27–29 (1956).

[88] J. R. Ferraro, K. Nakamoto, and C. W. Brown, *Introductory Raman Spectroscopy* (Academic Press, San Diego, 2002), 2nd ed.

[89] J. W. Ager, D. K. Veirs, and G. M. Rosenblatt, "Spatially resolved raman studies of diamond films grown by chemical vapor deposition," Physical Review B **43**, 6491–6499 (1991).

[90] N. Wada, P. Gaczi, and S. Solin, "diamond-like 3-fold coordinated amorphous carbon," Journal of Non-Crystalline Solids **3536, Part 1**, 543 – 548 (1980).

[91] C. F. Bohren and D. R. Huffman, *Absorption and scattering of light by small particles* (New York : Wiley, 1983).

[92] E. P. Schartner, H. Ebendorff-Heidepriem, S. C. Warren-Smith, R. T. White, and T. M. Monro, "Driving down the detection limit in microstructured fiber-based chemical dip sensors," Sensors **11**, 2961–2971 (2011).

[93] K.-M. C. Fu, C. Santori, P. E. Barclay, and R. G. Beausoleil, "Conversion of neutral nitrogen-vacancy centers to negatively charged nitrogen-vacancy centers through selective oxidation," Applied Physics Letters **96**, 121907–1–3 (2010).

[94] S. C. Warren-Smith, S. A. V., and T. M. Monro, "Theoretical study of liquid-immersed exposed-core microstructured optical fibers for sensing," Optics Express **16**, 9034–9045 (2008).

[95] S. C. Warren-Smith, H. Ebendorff-Heidepriem, T. C. Foo, R. Moore, C. Davis, and T. M. Monro, "Exposed-core microstructured optical fibers for real-time fluorescence sensing," Optics Express **17**, 18533–18542 (2009).

[96] K. Okamoto, *Fundamentals of Optical Waveguides*, OPTICS AND PHOTONICS SERIES (Elsevier Science, 2005), 2nd ed.